Title

Understanding Degradation in Polymer Electrolyte Fuel Cells for Light and Heavy-duty Vehicle Applications

Author

Khedekar, Kaustubh

Publication Date

2022

UNIVERSITY OF CALIFORNIA
IRVINE

Understanding Degradation in Polymer Electrolyte Fuel Cells for Light and Heavy-duty Vehicle Applications

DISSERTATION

submitted in partial satisfaction of the requirements
for the degree of

DOCTOR OF PHILOSOPHY

in Materials Science and Engineering
by

Kaustubh Bharat Khedekar

Dissertation committee:
Associate Professor Iryna Zenyuk, Chair
Professor Plamen Atanassov
Professor Jacob Brouwer

2022

Dedication

To my wife Rujvi and parents Bharat and Vijaya Khedekar

“Wonder is the feeling of a philosopher, and philosophy begins in wonder.”

- Socrates

Table of Contents

List of Figures

List of Tables

Acknowledgements

Firstly, I would like to thank my advisor, Prof. Iryna Zenyuk for her invaluable mentorship and support in my research. Your extraordinary work ethic and zeal for science will always be inspiring and an example to me. It kept me motivated even when experiments did not turn out as expected. I admire the way you share your exceptional knowledge and experience with all the students while promoting critical and sincere analysis of the data. Your generous nature to go above and beyond for the well-being of everyone around you is commendable. As your student, I promise to always carry forward these values. I am truly grateful for the time and effort that you invested to help me pursue my academic goals.

Next, I would like to thank my dissertation committee members Prof. Plamen Atanassov and Prof. Jacob (Jack) Brouwer for their valuable feedback and guidance to improve the results of this dissertation. I genuinely love any discussion with Plamen as it is full of fundamental science with the history behind it. Jack's passion for clean energy is unparalleled and his 'Fundamentals of Fuel Cell Technology' class was an exceptional learning experience for me. I would also like to thank the Bosch Research and Technology Center North America fuel cell team at Sunnyvale, CA. Particularly, I would like to thank Dr. Lei Cheng, Dr. Sarah Stewart and Dr. Christina Johnston for their significant contributions to this dissertation. The X-ray diffraction experiments performed by Dr. Lei Cheng with the help of beamline scientist Dr. Nobumichi Tamura are an important part of this dissertation. The text of this dissertation is in part a reprint of the material used with permission from Wiley and Royal Society of Chemistry. I thank them for the permission to include copyrighted figures as part of my dissertation.

I am grateful to several current and former lab mates at University of California, Irvine. I would like to specially mention and thank Dr. Prantik Saha for his outstanding contributions to this dissertation. Thank you to the co-authors Dr. Pongsarun Satjaritanun, Ying Huang, Hanson Wang and others without whom this work would have not been complete. Thanks to Dr. Andrea Perego for making me a meticulous researcher and introducing me to the basics of fuel cell testing. I am thankful to Dr. Yongzhen Qi and Dr. Devashish Kulkarni for their friendship and encouragement.

Finally, I would like to thank my wife, Rujvi. You have motivated me since the beginning and in times when experiments failed, and the workload was overwhelming. I am eternally grateful for your unwavering support and incredible sacrifices. None of this would have been possible without you. This dissertation is as much yours, as it is mine.

VITA

Kaustubh Bharat Khedekar

2017 B.E., Polymer Engineering, Maharashtra Institute of Technology, University of Pune

2019 M.S., Materials Science and Engineering, University of California, Irvine

2022 Ph.D., Materials Science and Engineering, University of California, Irvine

FIELD OF STUDY

Materials Science and Engineering

PUBLICATIONS

1. **Khedekar, K.**, Saha, P., Wang, H., Huang, Y., Stewart, S., Atanassov, P., Tamura, N., Cheng, L., Johnston, C. M., Zenyuk, I., “Understanding Carbon Corrosion in Polymer Electrolyte Fuel Cells,” Journal of Materials Chemistry A, 10, 12551 (2022).

2. **Khedekar, K.**, Satjaritanun, P., Stewart, S., Atanassov, P., Tamura, N., Cheng, L., Johnston, C. M., Zenyuk, I., “Effect of Commercial Gas Diffusion Layers on Catalyst Durability in Varied Cathode Gas Environment,” Small, 202201750 (2022).

3. **Khedekar, K.**, Rezaei Talarposhti, M., Perego, A., Metzger, M., Kuppan, S., Stewart, S., Atanassov, P., Tamura, N., Craig, N., Cheng, L., Johnston, C. M., Zenyuk, I., “Probing Heterogeneous Degradation of Catalyst in PEM Fuel Cells Under Realistic Automotive Conditions with Multi-modal Techniques,” Advanced Energy Materials, 2101794 (2021).

4. Cheng, L., **Khedekar, K.**, Rezaei Talarposhti, M., Perego, A., Metzger, M., Kuppan, S., Stewart, S., Atanassov, P., Tamura, N., Craig, N., Zenyuk, I., Johnston, C. M.,“ Mapping of Heterogeneous Catalyst Degradation in Polymer Electrolyte Fuel Cells,” Advanced Energy Materials, 2000623 (2020).

ABSTRACT OF DISSERTATION

Understanding Degradation in Polymer Electrolyte Fuel Cells for Light and Heavy-duty Vehicle Applications

by

Kaustubh Bharat Khedekar

Doctor of Philosophy in Materials Science and Engineering

University of California, Irvine 2022

Associate Professor Iryna Zenyuk, Chair

Governments and industries are pursuing the use of green hydrogen to achieve zero emissions, especially for difficult to decarbonize sectors such as transportation, aviation, shipping and chemical manufacturing. Polymer electrolyte fuel cells (PEFCs) are an excellent candidate for light and heavy-duty vehicles (LDVs and HDVs) particularly for their ability to scale range at a much smaller additional weight penalty. However, initial system cost remains a barrier for large scale adoption mainly due to use of Platinum (Pt) electrocatalyst. Reducing initial cost by utilizing highly dispersed Pt nanoparticles (2-3 nm) adversely affects the system lifetime. The smaller nanoparticle size does result in improved Pt dispersion, which enhances performance and reduces Pt loading and cost. But smaller nanoparticles also tend to degrade faster due to higher surface energy, which negatively impacts durability. During vehicle drive cycle, Pt nanoparticle surface undergoes repeated oxidation-reduction which leads to dissolution of Pt ions causing loss in electrochemical surface area. The dissolved Pt ions can redeposit on nearby larger nanoparticles. This effect is known as electrochemical Ostwald ripening. The Pt ions can also diffuse towards the anode and get reduced at the membrane-cathode interface by

the crossover hydrogen to form a Pt band. In addition, the Pt ions can completely leave the system via effluent water. The critical balance between cost, performance and durability makes understanding PEFC degradation a priority. Thus, implementing advanced electrochemical and analytical techniques, this dissertation addresses the challenge to decarbonize transportation sector by improving the durability of hydrogen powered net-zero emission PEFC systems.

The results of this dissertation can be distinguished into four chapters. In chapter 1, novel use of μ-X-ray diffraction (μ-XRD) was accomplished to analyze Pt nanoparticle size growth after accelerated stress tests were performed on MEAs using flow fields with different land-channel geometries. Two dimensional μ-XRD maps of the flow field inlet and outlet regions showed heterogeneity with higher electrocatalyst degradation near the inlet caused by increased local relative humidity. For flow field with land-channel dimensions 1 mm, higher electrochemical Ostwald ripening was observed under the lands when compared to channels due to differences between heat and water management. This land-channel heterogeneity disappeared for flow fields with land-channel dimension below 0.5 mm. However, the inlet-outlet heterogeneity stayed. In chapter 2, using μ-X-ray computed tomography (μ-XCT), morphological differences between commercially available gas diffusion layers (GDLs) like SGL 22BB, Freudenberg H23C6 and AvCarb MB30 designed to be used in high RH and high current density conditions were elucidated. Accelerated stress tests (ASTs) performed using the GDLs highlighted distinct effect of morphology and microporous layer cracks (via water management) on Pt dissolution. CFD simulations of water transport in GDLs (using Lattice Boltzmann method) were also used to explain the observed phenomenon. In chapter 3, using focused-ion

beam scanning electron microscopy, non-dispersive infrared spectroscopy, μ-XRD and μ-X-ray fluorescence (μ-XRF) in tandem with oxygen mass transport resistance experiments a precise chronology of cathode catalyst layer degradation (two phases) during carbon corrosion was revealed. In the initial phase, amorphous carbon in contact with Pt nanoparticles oxidized fast. Rapid carbon loss and catalyst layer thinning occurred, but pore structure did not change significantly. Pt nanoparticles detached from the support and ECSA decreased drastically. In the second phase, carbon corrosion slowed down, but severe pore structure collapse was observed explaining the apparent lag observed between carbon loss and the cathode catalyst layer pore structure collapse. In the last chapter, an experimental protocol was developed to enable μ-XRF mapping of membrane electrode assemblies subjected to HDV lifetime. Heavy in-plane movement of Pt in the cathode catalyst layer was revealed for the first time suggesting that electrochemical Ostwald ripening may not be a local effect. Successive synchrotron μ-XRD and μ-XRF discovered a previously unknown correlation between nanoparticle size growth and loading which develops only after HDV lifetime. The results provide short-term system mitigation strategies and long-term direction for durable catalyst materials development to enable zero emission PEFC vehicles.

1. Introduction

The time to discuss net zero emission goals has run out, and the time to put them into action is well underway. To date, 137 countries have committed to net zero carbon emissions by 2050 through announcement of various policies and strategic action plans focused on integration of renewable energy resources, mainly wind and solar [1]. Despite significant improvements in recent years, the use of renewable energy resources, specifically for difficult to decarbonize sectors, such as transmission, transportation and manufacturing has been challenging. For instance, California had more than 27.4 GW of electricity generated by solar as of the end of 2019, generating nearly 20 percent of the state's electricity [2]. With renewable electricity from solar and wind, widely available on the California electric grid, currently the state observes “duck-curve” of net energy demand at any day, where renewable energy is overproduced and curtailed during daytime and a ramp rate of 1.5 GW/hour is needed to meet the demand in the evening, when renewable sources are scarce [3]. Recent power-grid blackouts, fires and heatwaves stressed the grid significantly, particularly in the transmission sector, highlighting the need of alternative solutions that do not rely on electric transmission lines.

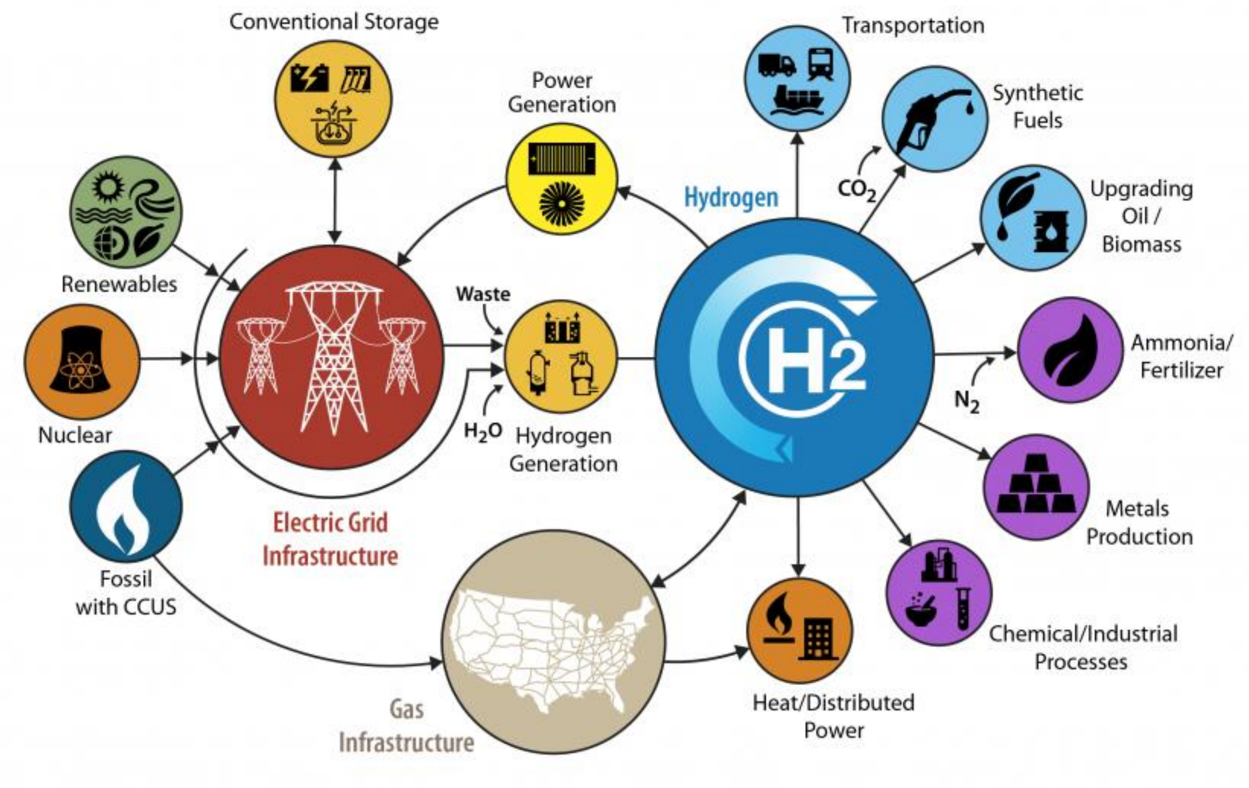

Figure 1.1 *H2@Scale, a United States Department of Energy initiative highlighting use of hydrogen as an energy carrier to decarbonize different sectors [4].*

Hydrogen is a promising energy vector as it can be used as an energy-storage medium for curtailed renewable energy. It can transform the electricity landscape (**Figure 1.1**), as a long-storage energy medium, as it can be injected into natural gas pipelines and transported through them or liquified and carried by trucks to the locations of demand. Thus, hydrogen economy can provide an alternative path to the difficult to decarbonize sectors. To jump start the hydrogen infrastructure and economy, United States Department of Energy (US DOE) recently introduced "Hydrogen Shot" with the '111' goal to reduce the production cost of green hydrogen to $1 per 1 kg of hydrogen in 1 decade [5]. Therefore, as green hydrogen becomes ubiquitous, its utilization in clean zero emission electrochemical conversion devices, such as polymer electrolyte fuel cells

(PEFCs) is highly promising, specifically in the transportation sector as it consumes the largest amount of energy and is at the lowest efficiency. Light-duty vehicles (LDVs) produce a massive 57% of the total U.S. transportation sector greenhouse gas (GHG) emissions [6]. More interestingly, heavy-duty vehicles (HDVs) make up only 7% of the total vehicles on-road but still produce nearly 26% of the total US transportation sector GHG emissions [6,7]. Combined, they account for three-quarters of the total US transportation sector GHG emissions. Most LDVs and HDVs are currently powered by gasoline and diesel engines that also emit nitrogen oxides and high level of particulates. Thus, electrification of the transportation sector is much needed to reduce its reliance on fossil fuels and to reduce GHG emissions.

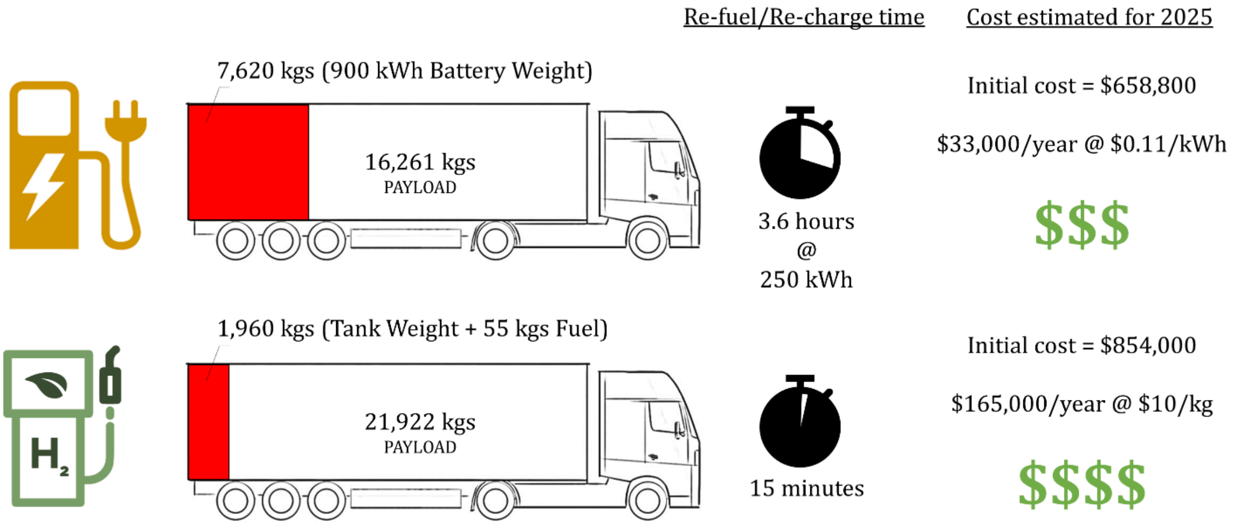

Figure 1.2 *Advantages of polymer electrolyte fuel cell powered heavy-duty vehicle for a one day, 2 shifts and 350 miles of regional haul. Analysis presented by Kenworth at the International Colloquium on Environmentally Preferred Advanced Generation (ICEPAG) 2020 meeting.*

Polymer electrolyte fuel cells (PEFCs) are an excellent candidate to power emission free vehicles, particularly HDVs due to their ability to scale driving range at a much smaller additional weight penalty (**Figure 1.2**) as hydrogen has a high energy density of 150

MJ/kg (liquid or compressed at 700 bar). PEFC vehicles can therefore have a large driving range with fast refueling time. In recent years, Toyota, Hyundai and Honda have successfully launched PEFC powered emission free LDVs. Multiple manufactures have also either planned or launched PEFC HDVs. However, initial system cost still remains a significant challenge for large scale adoption mainly due to the use of platinum-group metal (PGM) electrocatalysts to promote the sluggish kinetics of the oxygen reduction reaction (ORR) [8]. For a projected manufacturing volume of 100,000 HDV systems/year, the calculated PEFC stack cost is $41.93/kWe of which 53% is contributed by electrocatalyst and applications [9]. Current approach to reduce initial cost and improve performance by utilizing highly dispersed PGM nanoparticles (2-3 nm) on carbon support adversely affects stack lifetime [10]. Small well-dispersed nanoparticles result in improved PGM utilization by effectively increasing the electrochemically active surface area (ECSA). This boosts power density while reducing PGM loading and cost/kWe. However, repeated oxidation-reduction of Platinum (Pt) nanoparticles during vehicle lifetime causes Pt dissolution in the cathode catalyst layer [8,11]. This dissolution leads to loss in the ECSA via deposition of Pt in the membrane and increase in Pt nanoparticle size through electrochemical Ostwald ripening and/or coalescence [8].In addition, nanoparticles of Pt alloyed with transition metals such as cobalt (Co) and nickel (Ni) to reduce cost while enhancing ORR activity face significant leaching of transition metals within the voltage-pH range of PEFC operation [12]. Such transition metal leaching not only negates achieved improvement in ORR activity but also affects proton conduction and oxygen transport properties of ionomer causing loss in high current density performance [13]. The complex balance between cost, performance and durability of PEFCs coupled with the

2050 projection of 54% increase in HDV miles travelled [14] makes understanding electrocatalyst degradation to develop durable ORR electrocatalysts a top priority.

2. Background

2.1. Polymer electrolyte fuel cells

Polymer electrolyte fuel cells (PEFCs) also known as proton exchange or polymer electrolyte membrane fuel cells (PEMFCs) are electrochemical energy conversion devices that use hydrogen as a fuel and convert it into electricity and heat. A single PEFC consists of anode and cathode catalyst layers separated by a polymer electrolyte membrane (**Figure 2.1**). Hydrogen is fed on the anode and air on the cathode, both react in an electrochemical reaction on Pt nanoparticles supported on carbon in a catalyst layer. Hydrogen is oxidized at the anode into protons (H^+) and electrons during the hydrogen oxidation reaction (HOR, reaction 2.1). Protons travel through the membrane towards the cathode, while the electrons are routed via an external circuit where they perform electrical work. At the cathode, oxygen from air is reduced and recombines with protons and electrons during the oxygen reduction reaction (ORR, reaction 2.2) to form water.

$$\text{HOR}: \quad H_2 \rightarrow 2H^+ + 2e^- \qquad 2.1$$

$$\text{ORR}: \quad \tfrac{1}{2}O_2 + 2H^+ + 2e^- \rightarrow H_2O \qquad 2.2$$

$$\Sigma: \quad H_2 + \frac{1}{2}O_2 \rightarrow H_2O \qquad 2.3$$

Figure 2.1 also shows transmission electron microscopy (TEM) image of a typical catalyst used in PEFCs. Catalyst layers are composed of Pt nanoparticles, carbon black support and ionomer binder. Pt catalyzes the electrochemical reaction, carbon black disperses Pt nanoparticles to provide high ECSA and electrical conductivity, porosity of catalyst layers helps facilitate transport of oxygen and electrochemically produced water, whereas ionomer binder conducts H^+ ions.

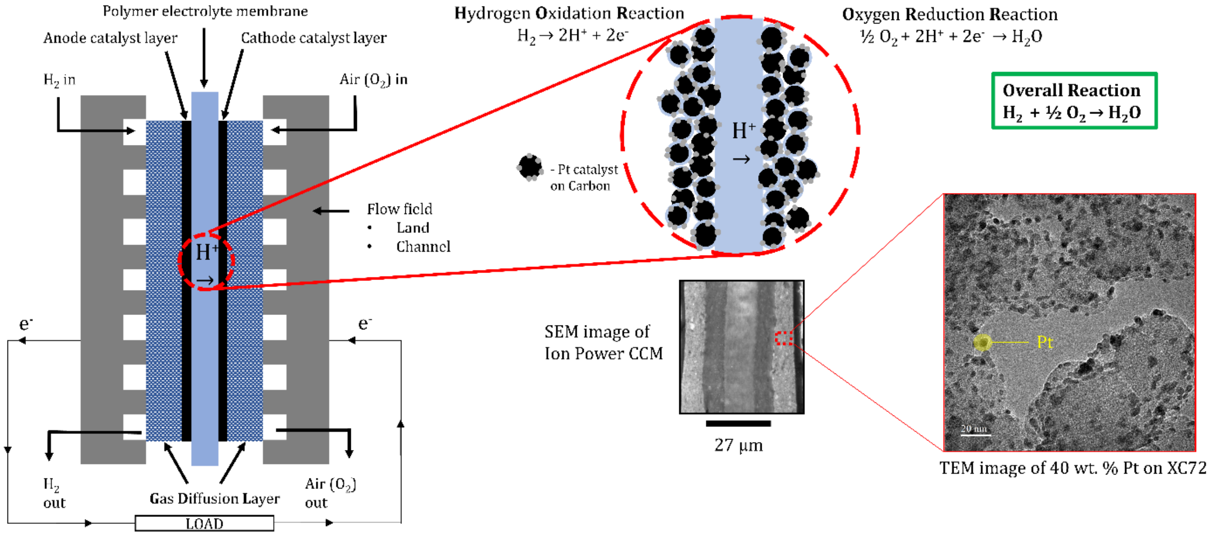

Figure 2.1 (L to R) Schematic representation of cross section of a single PEFC. SEM image of actual catalyst coated membrane cross section. The membrane is Nafion® XL with reinforcement. TEM image of Pt nanoparticles on carbon (XC72).

2.2. Parts of a polymer electrolyte fuel cell

A single PEFC consists of several layers of different materials each designed for a specific function. A summary of all the fuel cell parts can be seen in the schematic shown in **Figure 2.2**. Each described component has a significant influence on the performance and durability of a fuel cell. The PEFC components can be broadly classified into two parts: membrane electrode assembly (MEA) and hardware components. Since several single

PEFCs are stacked together in series to increase voltage and facilitate high power for the required application, low thickness of each component is a desirable feature.

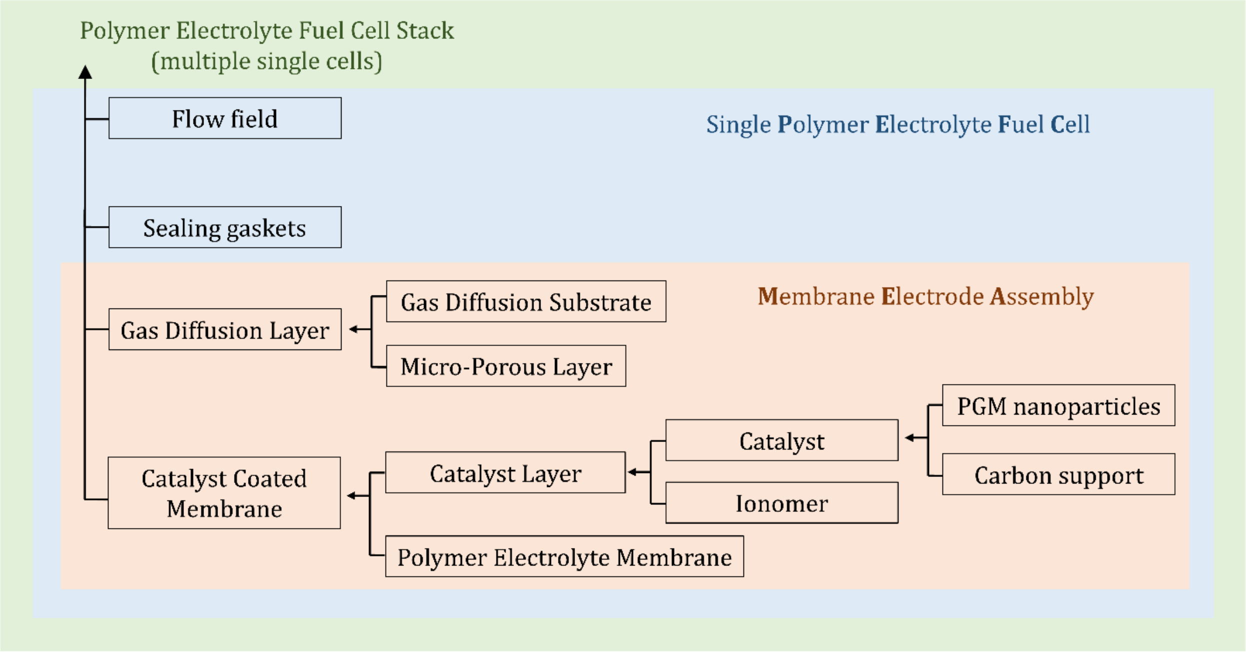

Figure 2.2 *Flow chart describing the various polymer electrolyte fuel cell components.*

2.2.1. Membrane electrode assembly

The MEA is where transport processes and electrochemical reactions happen. A MEA consists of 5 layers. They are: two gas diffusion layers (each for anode and cathode), cathode catalyst layer, anode catalyst layer and the polymer electrolyte membrane. There are multiple ways to fabricate a MEA, however they can be classified into two broad ways – the catalyst coated membrane (CCM) fabrication method and the gas diffusion electrode (GDE) fabrication method. In CCM method, the anode and cathode catalyst layers can be either directly coated on the polymer electrolyte membrane (PEM) or can be first coated on a substrate such as polytetrafluoroethylene (PTFE) and then hot-pressed on to the PEM. The CCM is then assembled with the gas diffusion layers. In GDE method, the catalyst layers are fabricated directly on the gas diffusion layers and are then either hot-pressed on the PEM or directly assembled. The MEAs prepared for experiments in this dissertation used commercially available CCMs (section 3.1.). Individual layers of a MEA are briefly discussed next.

2.2.1.1. Polymer electrolyte membrane

A typical PEM is fabricated casting an ionomer made of perfluorinated polymer containing ionic groups and is the key for PEFC technology. As PEMs are exposed to extremely harsh operating conditions like reducing and oxidizing environments over a wide range of temperatures and relative humidity, they require very high chemical and mechanical stability while maintaining high ionic conductivity and low gas permeation. Therefore, a PTFE long chain is utilized in combination with ionic side chains like perfluorosulphonic acid (PFSA) or perfluorocaboxylic acid [15]. The PTFE backbone provides high chemical and mechanical stability with low gas permeation while the PFSA side chains provide the high ionic conductivity. Equivalent weight (EW) of the ionomer used is an important parameter and can range from 700 to 1400 $g_{polymer}/mol_{SO_3^-}$, where a PEM with low EW will swell due to higher water uptake causing polymer dissolution and increased gas permeation while, the one with high EW may suffer from low ionic conductivity [15]. Nowadays, most of the commercially used PEMs contain expanded PTFE (ePTFE) as reinforcement to enhance the mechanical stability with radical scavengers added to reduce chemical degradation from attack of free radicals Thicknesses of PEMs used for commercial applications can range from 8 μm to 25 μm. Nafion® (DuPont) is by far the most widely used ionomer for membranes with Flemion® (Asahi Glass) and Aciplex® (Asahi Chemical) which differ mostly in the ionic side chain of the final ionomer.

2.2.1.2. Catalyst layers

Catalyst layers in PEFCs are random porous structures comprised of highly dispersed catalyst (Pt) nanoparticles supported by carbon mixed with ionomer. State of the art PEFC catalyst contains 2-3 nm diameter nanoparticles uniformly dispersed on a carbon with large surface area. The larger surface area of carbon allows deposition of higher weight percent (wt. %) of catalyst while maintaining the small nanoparticle size. Typically, large surface area carbons (~ 900 m^2/g) have mesoporous structure and can easily support upto 50 wt. % of catalyst allowing for higher catalyst loading with much lower catalyst layer thicknesses [16]. For instance, a catalyst layer with loading of 300 $\mu g^{Pt}.cm^{-2}$ will result in ~ 13 μm thickness for a 40 wt. % Pt on carbon catalyst, while a 1 wt. % Pt on carbon catalyst for the same loading will have ~ 90-100 μm thickness. Lower catalyst layer thickness is desirable as it reduces the tortuous pathways for oxygen diffusion, H^+ ions transport and helps in removal of electrochemically produced water consequently decreasing the ohmic and mass transport overpotentials at high current densities. To fabricate a catalyst layer, the catalyst powder is first dispersed in solvents along with an ionomer solution such as D2020 (20 wt. % Nafion® in solvents). This is called as a catalyst ink. An optimum ionomer to carbon (I/C) ratio is used to prepare the catalyst ink with defined solvent ratios. An ionomer serves as a binder and facilitates proton conduction to the reaction sites in the catalyst layers. Too low of ionomer content can result in low catalyst layer conductivity while too high of ionomer content can increase oxygen diffusion resistance at the catalyst-ionomer interface and reduce the porosity of the catalyst layer by blocking secondary agglomerate pores due to swelling from water uptake.

Fabrication of catalyst layers can be done directly on the PEM by slot die casting, ultrasonic spray coating and by decal transfer method. Alternatively, the same methods can be used to prepare GDEs. Each fabrication procedure requires different ink recipe and dispersion methodology to achieve optimum PEFC performance. Morphological features like cracks can develop during this fabrication step either due to swelling of the PEM or the morphology of the gas diffusion layer. The catalyst layer morphology thus plays a crucial role in water management and significantly affects PEFC performance and durability.

2.2.1.3. Gas diffusion layers

The GDL is a three-dimensional bi-layer composed of a highly porous gas diffusion substrate (GDS) and a micro porous layer (MPL) coating made of carbon and hydrophobic additives. The typical thickness of a commercially available GDL is in the range of 100 -500 μm [17]. The GDS is a carbonaceous skeleton made up of carbon fibers arranged in different patterns and has an average porosity of 70 - 90% with an average pore diameter ranging from 5- 40 μm [17]. The MPL coating is made from a slurry of carbon black and a hydrophobic polymer such as PTFE. Compared to GDS, MPL has much lower porosity of 25-50% and a finer average pore diameter ranging from 50- 200 nm [18].

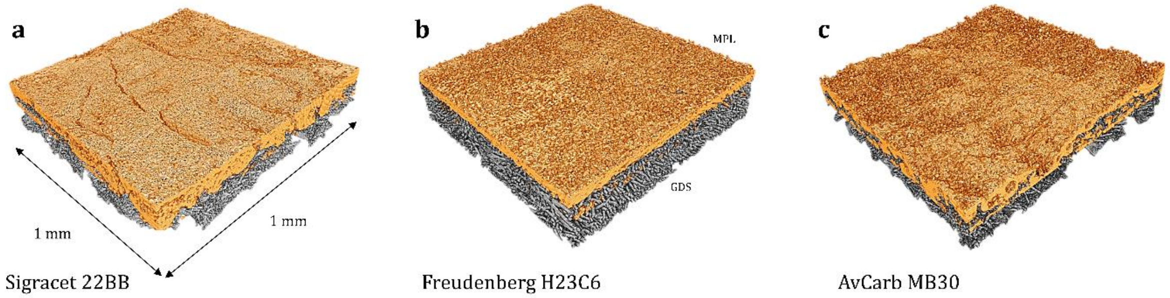

Figure 2.3 *1 cm x 1 cm 3D reconstructed area from micro x-ray computed tomography highlighting key features of different GDLs.*

The GDLs are sandwiched between catalyst layers and the flow field and have following functions - 1.) Facilitate distribution of reactant gases from the flow field channels to the catalyst layers. High porosity and low tortuosity of the GDS are important parameters which can drastically change due to liquid water saturation in it. 2.) Remove electrochemically produced liquid water from the cathode catalyst layer to avoid flooding and reduce mass transport overpotentials. Hydrophobicity of the MPL, presence or absence of MPL cracks and wettability of GDS play a key role. 3.) Conduct electrons from the catalyst layers to the flow fields. Presence of binders and hydrophobic polymers such as PTFE which are electrically insulating in nature can significantly impact GDL electrical conductivity. Also, the compression of GDL greatly affects contact resistances between catalyst layer-GDL-flow field [19]. 4.) Conduct heat produced due to electrochemical reactions in the catalyst layers to ensure operation at desired temperature and RH. And lastly, 5.) Provide mechanical integrity to the membrane electrode assembly (MEA) [19]. Commercially manufactured GDLs utilize different strategies to fine tune properties to cater efficiently to all the above-mentioned functionalities. Suitable precursors are selected, polymerized and extruded into fibers [20]. The fibers are then thermally oxidized and carbonized. The carbonized fibers are turned into a compacted and compressed form of paper (GDS) [20]. This can be done using multiple techniques such as chopping the fibers to desired length and creating a slurry with binders or mechanically curling the fibers by quenching and then compacting and compressing. This step influences the pore size distribution, porosity, density and thickness of the GDS. Sacrificial materials can be used in the binders to counter their effect on porosity. The formed paper is then cured for the binder and the fibers are graphitized. The degree of graphitization will depend on the temperature and the type of precursors selected. The paper is then treated with hydrophobic polymer to tune its wettability [17,20]. Finally, a MPL coating is tape casted on the GDS [20]. The MPL coating can either be embedded in the GDS or can be freestanding and can have a smooth, undulating or cracked surface (**Figure 2.3**). The GDL therefore has an important influence on evaporation and condensation of incoming water vapor in the catalyst layers and on removal of electrochemically produced water either in liquid or vapor form from the cathode catalyst layer. Thus, commercially available GDLs manufactured for application in similar operating conditions but designed using different gas diffusion and water removal strategies can have significant impact on catalyst degradation over the course of PEFC vehicle lifetime.

2.2.2. Hardware

Although the MEA produces voltage and current density, hardware components are necessary to facilitate optimal and efficient operation of MEAs. The main hardware components of a PEFC are flow field and sealing gaskets which are briefly discussed next.

2.2.2.1. Flow field

A typical laboratory scale flow field is made up of a conductive material usually graphite (in case of PEFCs) to facilitate flow of electrons with minimal contact resistances. It has flow channels engraved (**Figure 2.4**) with different patterns such as multiple serpentine or parallel channels designed for uniform distribution of humidified reactant gases and removal of water. The part in between two consecutive channels is known as a land. Each flow field design has different benefits in gas diffusion, water removal and contact resistance. Larger lands tend to achieve lower contact resistances and better thermal management but might affect water removal. Larger channels will effectively distribute gas and remove water but might lead to high contact resistances and non-uniform GDL compression. In addition, the pressure drop between the inlet and outlet of a flow field also significantly depends on the type of design and the land-channel ratio.

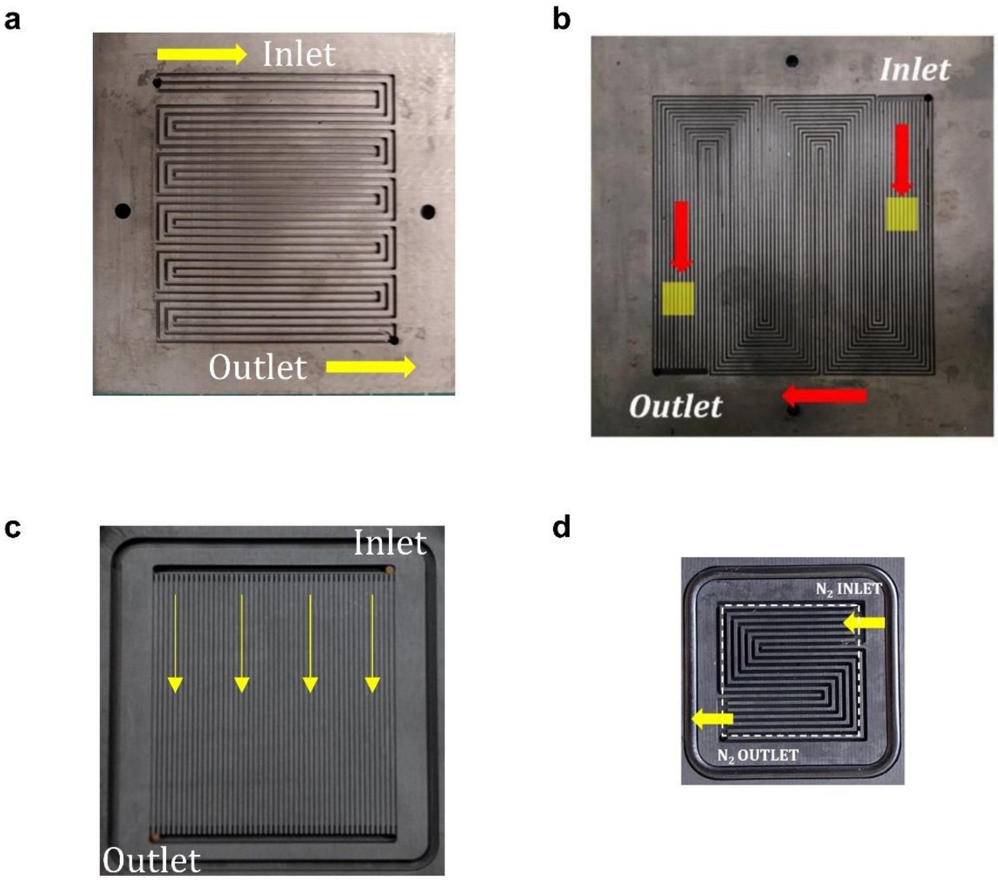

Figure 2.4 *Types of flow fields. a, 25 cm^2 x3 channel serpentine b, 50 cm^2 x14 channel serpentine c, 25 cm^2 parallel channel and d, 5 cm^2 x7 channel serpentine. The number of bends in each flow field are also different.*

Since a single PEFC produces less than 1 V under relevant operating conditions, it is necessary to stack multiple PEFCs in series to achieve usable voltage and power. This is usually done by sandwiching each MEA in a stack between two bipolar plates (flow field with channels on both sides). Bipolar plates maybe made of metal, carbon or a conductive composite and can also have channels for coolant circulation.

2.2.2.2. Sealing gaskets

Sealing gaskets are placed at the edge of the flow field to prevent any leaks from the PEFC. For single fuel cells prepared in labs, fiber reinforced PTFE (FR-PTFE) along with pristine PTFE of various thicknesses are used in combination as gasket materials. They provide sealing when compressed in between two flow fields and are also used to control the compression of the GDL. For instance, if 15% compression is required for a GDL of thickness 230 μm, it can be achieved by using a combined gasket thickness of ~ 200 μm. At stack level, in addition to sealing and GDL compression, gaskets are also used to eliminate area of the inactive membrane reducing cost. Some lab-scale hardware's utilize O-ring for sealing and thus do not require use of gaskets.

2.3. Degradation in polymer electrolyte fuels

PEFC technology has advanced to reach the commercialization stage with more automotive manufacturers announcing new PEFC-based light and heavy-duty vehicles. However, the durability and cost of such systems remains a challenge. Using the DOE cost breakdown for the 80-kWnet stack for LDVs, the cost of precious metal electrocatalyst remains almost unchanged as production rate increases to 500,000 PEFC stacks per year [21]. The cost of the electrocatalyst amounts to 31% of stack cost, for 500,000 LDV systems per year production rate [21]. Pt or Pt-alloys are used as electrocatalyst for the ORR on the cathode side and the HOR on the anode side of PEFCs. Pt or Pt-alloy electrocatalysts are dispersed as nanoparticles onto a carbon-black support. DOE has set a target of reducing Pt loading to 0.125 mg.cm^{-2} to achieve the goal of \$12.6 kW$_{net}^{-1}$ for a stack with power density target of 1.8 W.cm^{-2} for LDVs [22]. MEAs with lower catalyst loading are less durable [23], thus, the cost issue cannot be resolved without focusing on the catalyst durability issue of the PEFC stack. Moreover, HDVs require stacks with 25,000 -30,000 hours lifetime [10], which to date requires ≥ 0.4 mg cm^{-2} Pt catalyst loading. Significant progress in understanding and mitigating cathode catalyst degradation is therefore required to enable the ultimate 2050 HDV lifetime target of 30,000 hours with 0.25 mg cm^{-2} catalyst loading set by the DOE.

More generally, catalyst degradation occurring during PEFC operation impacts the performance by decreasing the power density of the stack and by increasing fuel consumption per generated kWh. PEFC catalyst durability has been previously studied extensively. Pt electrocatalysts are more prone to degradation on the cathode side of the PEFCs, rather than the anode due to higher potentials and more oxidizing conditions. Previously, Wang et al. reported electrochemically active surface area (ECSA) loss of 54.5 % for cathode [11]. They reported higher degradation rates (more ECSA loss) on the cathode side which is due to several factors including: 1.) wider range of potential, 2.) higher difference in pH values and 3.) higher water content. Various studies have also shown that load changing and startup-shutdown, contribute the most to the overall performance loss through catalyst degradation and carbon support corrosion [24]. Dynamic load change is the largest contributor to degradation for various reasons: i) it induces humidity and thermal cycling, ii) it may cause gas starvation and iii) potential cycling due to dynamic load degrades the Pt electrocatalyst.

2.3.1. Simulating light and heavy-duty lifetimes by accelerated stress tests

To assess PEFC durability, accelerated stress tests (ASTs) are used because the experimental time can be reduced compared to using a real vehicle drive-cycle that typically (according to ultimate DOE durability targets) needs to last 8,000 and 30,000 hours for LDV and HDV applications, respectively. ASTs generally include potential cycling between two potentials to simulate load change and accelerate degradation of the catalyst layer. Each potential cycle corresponds to a vehicle acceleration and deceleration event. Degradation includes morphological changes in the catalyst layer that cause performance loss, such as crack formation, thickness loss, ECSA loss and diffusive, ionic and electric pathway connectivity loss leading to transport losses. Degradation of PEFCs has been both physically modeled and experimentally investigated. The influence of voltage cycle profiles on degradation of MEAs has been comprehensively reported by Stariha et al. [24] where the study used square wave and triangular wave potential cycling and evaluated degradations of both the catalyst and the support in different potential ranges. ASTs with square wave voltage cycling showed the highest rate of catalyst degradation. This is since degradation rates, including ECSA loss, increase with the increase of dwell time at the upper potential limit (UPL). Thus, the DOE adopted a square wave voltage cycle with UPL of 0.95 V and lower potential limit (LPL) of 0.6 V with a dwell time of 3 seconds each (**Figure 2.5**). This square wave voltage cycle, originally reported by Nissan [25], is repeated 30,000 times in H_2/N_2 (anode/cathode) environment under atmospheric pressure to simulate the LDV lifetime of 8,000 hours and evaluate catalyst degradation. This AST was therefore utilized in the dissertation for LDV lifetime. To understand effect of reactive (air) vs non-reactive (N_2) environments on catalyst degradation mechanisms, same AST was utilized but with open circuit potential as the UPL.

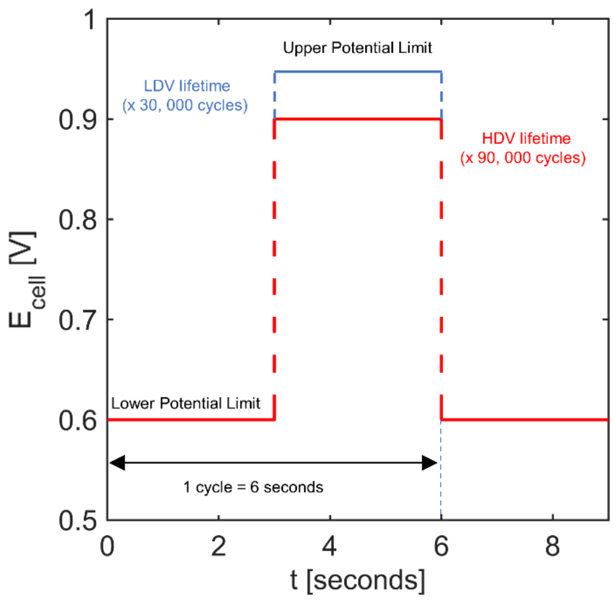

Figure 2.5 *Square cell voltage cycle consisting of 0.6 V LPL and 0.9 V (for HDV) and 0.95 V (for LDV) UPL with a hold time of 3 seconds each.*

Using a representative HDV drive cycle for Class 8 truck reported by the California Air Resource Board, the National Renewable Energy Laboratory simulated the cell voltages for a hybrid 250 kWe fuel cell system/35 kWh battery traction power system with a minimum idle power of 20 kWe to limit the upper potential limit (UPL) at 0.9 V [26]. Electrocatalyst degradation is severely impacted by high UPLs, thus UPL for HDV lifetime needs to be clipped at 0.9 V to ensure that US Department of Energy (DOE) interim and ultimate system lifetime targets of 25,000 and 30,000 hours are reached. A further low value of UPL cannot be used as it decreases overall system efficiency while causing thermal management issues. Based on the simulated cell voltages and previous DOE recommended LDV AST equating to 8,000 hours of system lifetime, a square cell voltage cycle as depicted in **Figure 2.5** with lower potential limit (LPL) of 0.6 V and UPL of 0.9 V with a hold time of 3 seconds each was adopted in the dissertation. To equate the AST to ≥ 25,000 hours of HDV lifetime the 6 second square cell voltage cycle was repeated for 90,000 times in a non-reactive cathode gas (N_2) environment giving a total AST time of 150 hours. The number of cycles were selected to be 90,000 for HDV lifetime as ECSA decreases exponentially and reaches a plateau by the selected number of cycles.

2.3.2. Fundamentals of Platinum degradation

The standard Nernst equilibrium potential of direct dissolution reaction of Pt ions when corrected for the increased surface energy of nanoparticles can decrease to ~ 0.5 V (1 nm and 10^{-6} M of Pt^{2+}) compared to ~ 1 V of bulk Pt [27]. This is commonly known as the Kelvin or Gibbs-Thompson effect. This effect can also be observed for dissolution of Pt ions during reduction reaction of Pt oxide. The equilibrium potential for dissolution of Pt ions from nanoparticles is further lowered by decreasing concentration of Pt ions [27]. Thus, purely based on thermodynamic analysis, significant degradation of Pt nanoparticles occurs via Pt dissolution within PEFC operational voltage (0.6 V to 1 V) and pH (~ 1 to 4) range. This also means that degradation is affected not only by electrocatalyst properties such as nanoparticle size, distribution, crystalline orientation, dispersion and carbon support type but also by the local cathode catalyst layer environment. The local environment can be affected by operating conditions like cell temperature, relative humidity (RH), reactant flow rates and by PEFC components like MPL of GDL and flow field [28,29]. Cell temperature and RH are serious Pt degradation stressors which can be influenced in the local environment by cathode catalyst layer morphology. These include but are not limited to features like porosity, in-plane/through-plane Pt loading distribution and catalyst layer cracks. Liquid water flux in the cathode catalyst layer, affected by the interplay between operating conditions, PEFC components and morphology also plays crucial role to control local RH and Pt ion concentration consequently influencing electrocatalyst degradation [28,30].

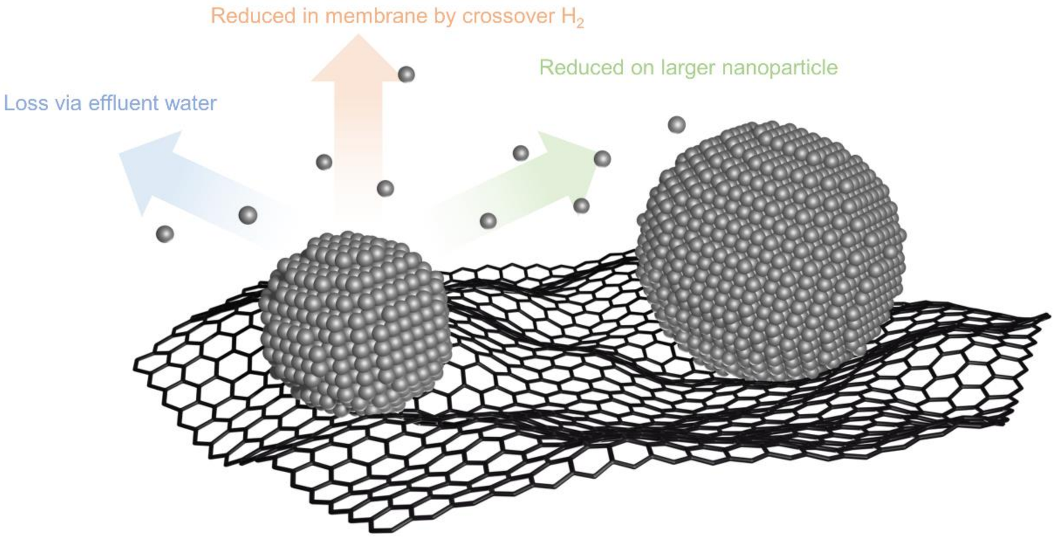

Figure 2.6 *Three ECSA loss pathways caused by dissolution of* Pt^{X+} *ions from Pt nanoparticles during PEFC vehicle operation.*

Dissolution of Pt ions results in three pathways of ECSA loss as shown in **Figure 2.6** where, 1.) the Pt ions can reduce on nearby larger nanoparticles with lower surface energy [11], 2.) the Pt ions can diffuse towards the anode and get reduced in the membrane by crossover hydrogen to form a Pt band [31]. The physical location of such Pt band is governed by the partial pressures of hydrogen and oxygen during the AST [32]. For a non-reactive cathode gas (N_2) environment, the Pt band is located near the membrane-cathode interface. And lastly, 3.) the Pt ions can completely leave the system with the effluent water. This ECSA loss pathway is less explored although inductively coupled plasma mass spectroscopy (ICP-MS) reports of effluent water have detected concentration of Pt ions [30]. The dominant ECSA loss pathway of course depends on the thermodynamics of Pt dissolution, but it also depends heavily on the convoluted interplay between kinetics of Pt oxidation, dissolution and reduction [33]. Thus, UPL, LPL and dwell time at each potential limit during the AST can also affect Pt dissolution. Electrochemical analysis of MEA tests coupled with *in situ* ICP-MS studies suggest that the cathodic step of AST cell voltage cycle (i.e. stepping from UPL to LPL) causes maximum dissolution of Pt ions [33]. The dissolution is attributed to reduction of Pt oxide (~ 0.8 V) formed at the UPL. The formation rate and coverage of Pt oxide is greatly affected by the UPL and the hold time [34], respectively. Therefore, a higher value of UPL with longer hold time will result in increased Pt oxide formation and consequently higher dissolution during the cathodic step. Dissolution during the cathodic step also makes Pt degradation a function of number of AST cycles [35]. A constant hold at UPL for extended periods of time will only passivate the nanoparticle surface reducing the dissolution rate [8]. The rate of reduction of Pt ions is reported to be relatively high ≤ ~ 0.6 V [36]. Thus, a higher value of LPL affects the amount of Pt oxide formed at UPL during the next cell voltage cycle as less clean Pt surface is available for oxide formation. This is also why Pt degradation is less influenced by hold time of a sufficiently low LPL. Several studies are still ongoing to fully understand the effects of above discussed properties and parameters on electrocatalyst degradation.

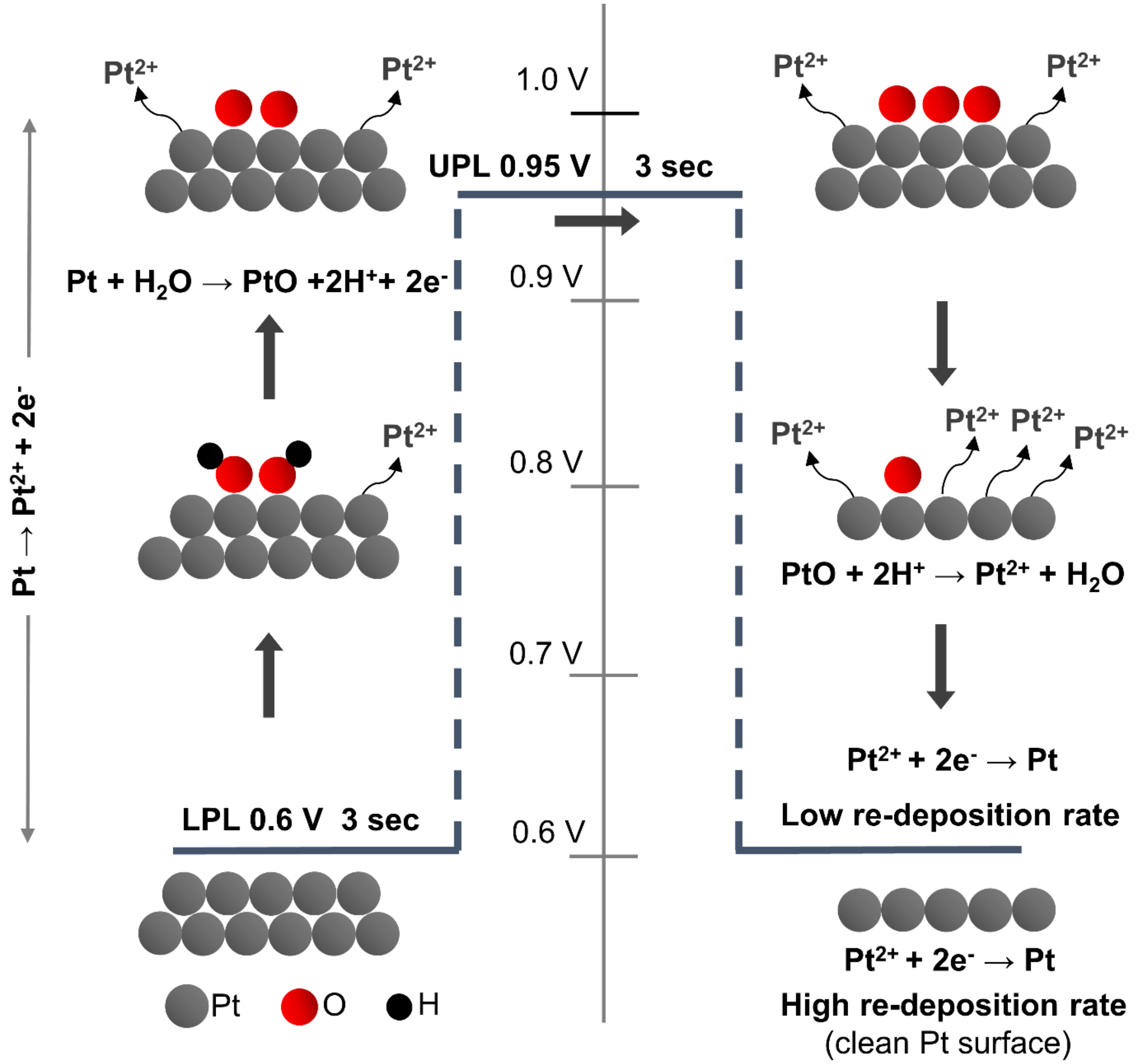

***Figure 2.7** A schematic of the square cell voltage cycle used in this dissertation for LDV lifetime with corresponding Pt degradation reaction mechanisms considered.*

Figure 2.7 shows the schematic of an AST potential cycle with the possible Pt degradation reaction mechanisms considered in this dissertation. During the anodic scan (from low to high potential), pristine Pt surface is present (at beginning of test) at the LPL. During the potential step from the LPL to the UPL Pt dissolution occurs at the defect sites at a low rate. As the potential crosses 0.8 V, OH groups form on the Pt surface ultimately leading to the formation of PtO, as the potential reaches the UPL. During the potential hold at the UPL, PtO coverage increases and a place-exchange mechanism may occur (where Pt and O exchange the position) along with Pt dissolution at a low rate. As the potential is swept down to the LPL in the cathodic scan, PtO is reduced (~0.8 V), as it reacts with protons to form dissolved Pt and water. If the LPL is in a low re-deposition potential range (above ~0.6 V), then unavailability of pristine Pt surface for the Pt ions to redeposit can primarily lead to Pt band formation in the membrane with relatively low Pt particle size growth. This will also reduce the available surface for oxide formation during the next cycle. If the LPL is in high re-deposition potential range (at or below ~0.6 V), then availability of pristine Pt surface for the Pt ions to redeposit can make Ostwald ripening as the primary ECSA loss pathway with higher Pt particle size growth. This also indicates that the amount of PtO formed during the UPL hold of AST cycles directly depends on the LPL (i.e., the availability of pristine Pt surface). At lower UPLs, PtO coverage is lower, resulting in a smaller number of Pt ions formed, consequently causing less degradation over the AST duration.

2.3.3. Fundamentals of carbon corrosion

If startup/shutdown (SUSD) is performed in an uncontrolled way, i.e., when the cell is in open-circuit condition and H_2 is injected in/ejected out the anode compartment without N_2 flushing, a mixed gas front is formed between H_2 and O_2 (from air). This mixed gas front triggers a chain of electrochemical reactions inside the cell that eventually leads to carbon corrosion. The complete mechanism has been explained by Reiser et al. [37] using a reverse-current mechanism. A schematic of the corresponding electrochemical reactions (redrawn based on schematic in [37]) due to reverse current mechanism with resulting potential distribution is shown in **Figure 2.8 a**.

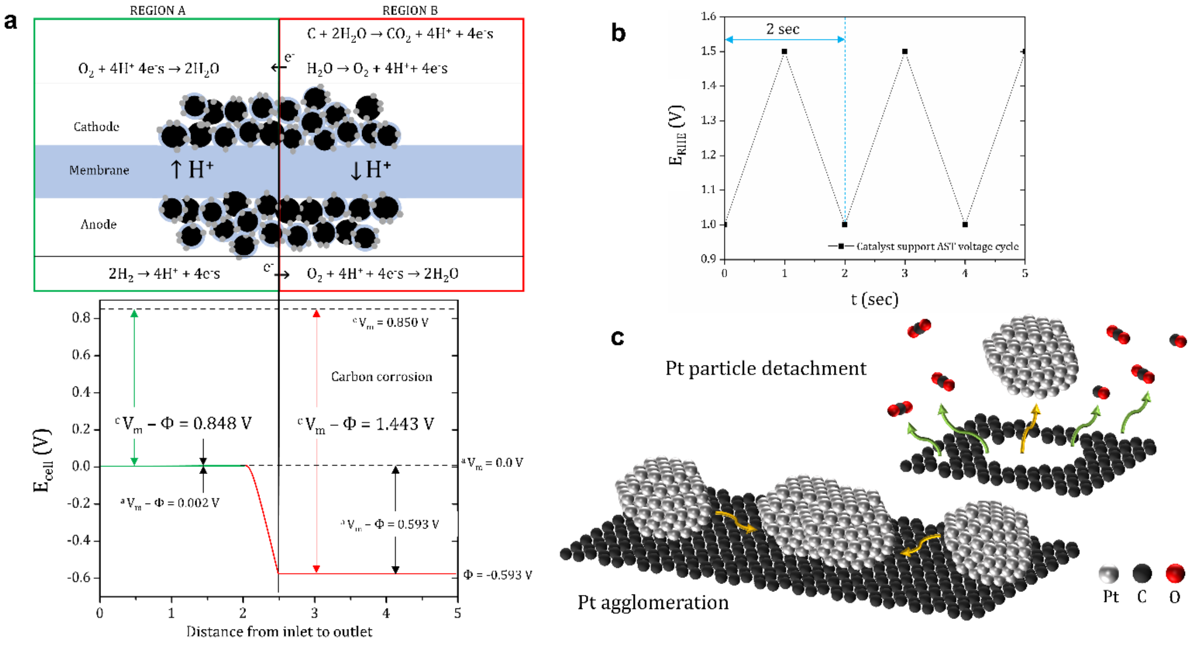

Figure 2.8 Fundamentals of carbon corrosion. a, Electrochemical reactions occurring inside the cell due to a mixed H_2/O_2 front at the anode with corresponding potentials in different regions of the cell. b, The DOE carbon corrosion AST voltage profile to simulate the reverse current mechanism. c, Expected catalyst degradation mechanisms- Pt detachment from carbon support and Pt agglomeration.

The DOE carbon corrosion AST voltage cycle to mimic the operation, and the major degradation reaction mechanisms of carbon corrosion is shown in **Figure 2.8 b** and **c**. The AST was formulated to mimic the potential at cathode region B during the reverse-current mechanism. Brightman and Hinds [38] found that the local potential in cathode region B, where carbon corrosion occurs, is approximately 1.4 V. So, the AST is done by cycling the cell voltage uniformly with time in a triangular waveform with 1 V as the lower limit and 1.5 V as the upper limit. The scan rate is 500 mV/s. As water, not gaseous O_2, oxidizes carbon, the AST is done with H_2 at anode and N_2 at cathode in 100% RH. **Figure 2.8 c** shows the two expected catalyst degradation modes during carbon corrosion - Pt detachment from the carbon support and Pt agglomeration. It is important to note that the carbon corrosion AST is much harsher than the actual SUSD. This is because, carbon only corrodes from region B of the cathode during SUSD while carbon corrodes from the entire cathode catalyst layer during DOE carbon corrosion AST.

3. Experimental

3.1. Materials

Chapter 1. Pt/C based catalyst (TEC10E50E) coated membranes were purchased from Ion Power Inc., New Castle, Delaware, with an active area of 25 cm^2 and loading of 0.3 mg$_{Pt}$cm^{-2} and ionomer to carbon (I/C) ratio of 1 on both anode and cathode. The catalyst coated membranes contained Nafion® XL reinforced membrane of thickness 27.5 µm. A non-woven carbon paper, Sigracet 29 BC, with 5 wt % PTFE treatment and hydrophobic MPL was used as GDL. The total thickness of the GDL is reported by the manufacturer as 235 µm.

Chapter 2. The CCMs were purchased from Ion Power Inc., New Castle, Delaware. 6 cm^2 active area MEAs were prepared by masking 25 cm^2 Ion Power CCMs with Pt/C (TEC10E50E) catalyst. The Pt loading was 300 µg.cm^{-2} on both anode and cathode. The ionomer to carbon (I/C) ratio was 1. The CCMs had ~27.5 µm thick Nafion XL membrane. Sigracet 22BB, Freudenberg H23C6 and AvCarb MB30 were purchased from Fuel Cell Store, College Station, Texas, USA and were used as the three cathode GDLs. Sigracet 22BB was the anode GDL and was kept constant for all the ASTs.

Chapter 3. Ion Power CCMs (New Castle, DE) with 25 cm^2 active area were masked to 5 cm^2 active area. The catalyst layers were made with TEC10E50E catalyst powder from Tanaka Precious Metals, Japan (46.1% Pt/HSAC carbon) with Pt loadings of 0.3 mg.cm^{-2} (both anode and cathode)) with I/C ratio of 1. 27.5 µm thick Nafion XL membrane was used in all the CCMs. Sigracet 22BB gas diffusion layer was used on both anode and cathode to prepare MEAs. Multiple MEAs from the same batch were used to study different morphological changes along with electrochemical diagnostics.

Chapter 4. Commercial CCMs from Gore® Fuel Cell Technologies (Newark, DE) were used to prepare two MEAs with 5 cm^2 active area. Freudenberg H23C6 was used as both anode and cathode GDL for the first standard MEA. Cracks were introduced in the MPL of only cathode Freudenberg H23C6 GDL to prepare the second modified MEA.

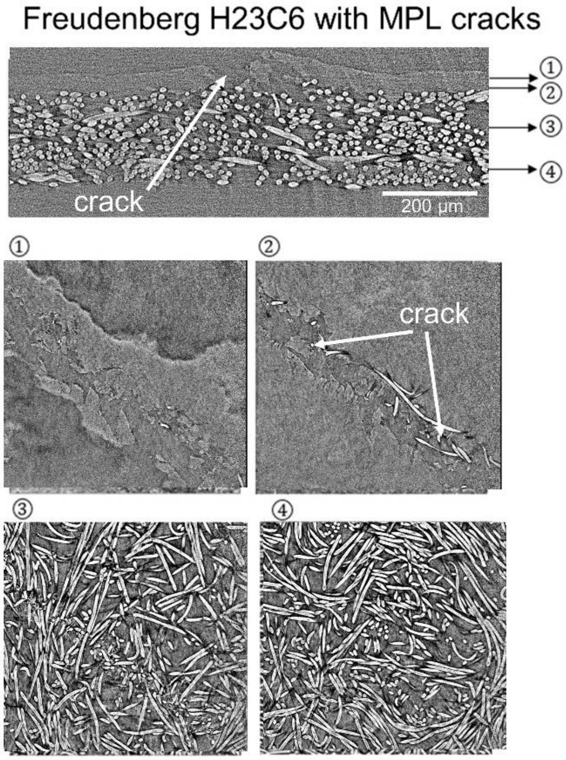

Figure 3.1 *Freudenberg H23C6 GDL with ~ 40-50 µm wide cracks fabricated in the MPL.*

Cracks of ~ 40-50 µm width were milled into the 35 µm thick free-standing MPL of Freudenberg H23C6 GDL using the ~ 15 µm wide tip of tungsten micro needle. The fabrication was done by hand under an optical microscope (x 20) with a pitch of 1 mm. µ-

X-ray computed tomography was performed to confirm the morphology (**Figure 3.1**). The MPL cracks provided a direct transport pathway between the gas diffusion substrate and the cathode catalyst layer for reactants and products.

3.2. Testing equipment

3.2.1. Fuel cell fixture

Chapter 1. Fuel cell fixture hardware from Scribner Associates with POCO graphite 3X serpentine flow field (0.92 mm/0.79 mm width lands/channels) was used in co-flow configuration. Hard-stop PTFE-coated fiberglass gaskets (150 µm thickness) and PTFE gaskets (27.5 µm thickness) were used to achieve GDL compression of 22 %. 13.5 Nm torque was used during the cell assembly.

Chapter 2, 3 and 4. Fuel cell quick connect fixture (qCf) in combination with a cell fixture (cF) from balticFuelCells GmbH, Hagenower Str.73.D-19061 Schwerin, Germany was used. The flow-field contained 7X channel serpentine flow field of 6 cm^2 area, adapted from Simon et al. [39]. The cell compression in this setup is pneumatically controlled. A pneumatic compression pressure of ~0.9 bar was used to achieve the manufacturer recommended 1-1.1 MPa pressure on the GDLs as shown by **Figure 3.2**. This compression pressure resulted in a low contact resistance. The GDL compression was 20-22% as recommended by the different GDL manufacturers.

For limiting current measurements in chapter 3, parallel channel flow field was used as shown in **Figure 2.4 c**.

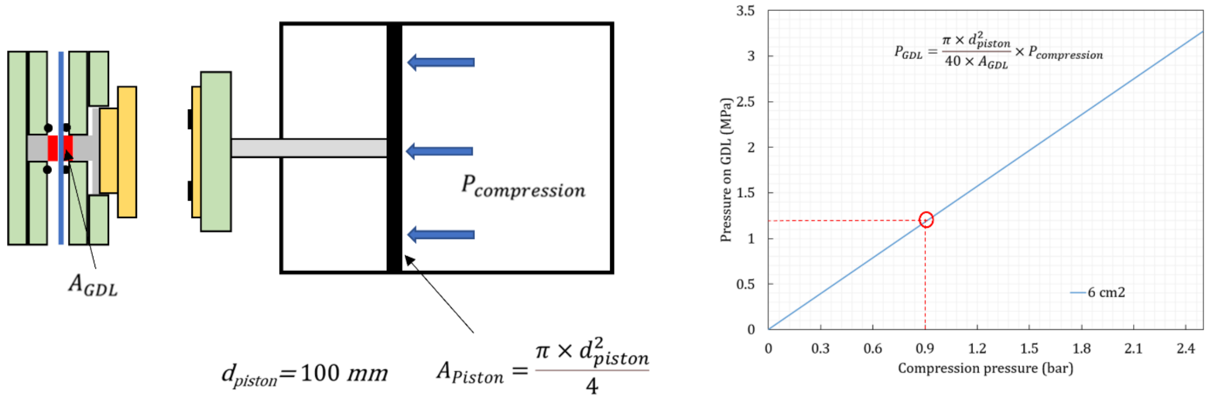

Figure 3.2 *(L to R) Schematic of Baltic hardware with pneumatic compression and pressure on GDL as a function of the pneumatic compression.*

3.2.2. Test station

Load based electrochemical characterization and ASTs in all chapters were performed using the 850e Fuel Cell Test Stand (Scribner Associates, Connecticut, USA) with maximum current load of 50 A. VSP-BioLogic (potential resolution of 5 µV and maximum current of 4 A) or Gamry (maximum current 5 A) potentiostat were used for non-reactive (N_2) cathode environment electrochemical characterization.

3.3. Accelerated stress testing protocols

Chapter 1. Four square wave ASTs were conducted. The conditions for ASTs were either H_2/N_2 or H_2/air on anode/cathode both in 40 % and 100 % RH. The ASTs were conducted with potential cycling from 0.6 V to 0.95 V in N_2 on cathode, or 0.6 V to 0.95 V or OCP, if OCP < 0.95 V for air gas on cathode with a dwell time of 3 seconds at each potential for 30,000 cycles, resulting in a total (AST only) time of 50 hours. The AST was performed at atmospheric pressure and in H_2/air (anode/cathode) and H_2/N_2 environments at 100 %

(wet) and 40 % (dry) relative humidity (RH) with gas flow rates of 210 sccm/830 sccm (anode/cathode) for H_2/Air and 200 sccm/200 sccm for H_2/N_2 (**Table 3.1**).

Table 3.1 *Relative humidity, gas environment on cathode and gas flow rates of different MEAs used in chapter 1 ASTs.*

MEA	**AST RH (%)**	**Cathode gas used during AST**	**Gas flow rate, anode/cathode (sccm)**
N_2 Dry	40	N_2	200/200
N_2 Wet	100	N_2	200/200
Air Dry	40	Air	210/830
Air Wet	100	Air	210/830

For the ASTs performed in air the OCP decreased with the cycle number and for this reason the UPL was reduced (**Figure 3.3**). The OCP was partially recovered during a voltage recovery protocol before electrochemical characterization. Flow Rates were calculated for stoichiometric ratio of 1.2/2 (anode/cathode) assuming maximum current density of 1A cm^{-2} at 0.6 V. During the AST, each MEA was characterized at stages of 0, 1000, 5000, 15000 and 30,000 cycles.

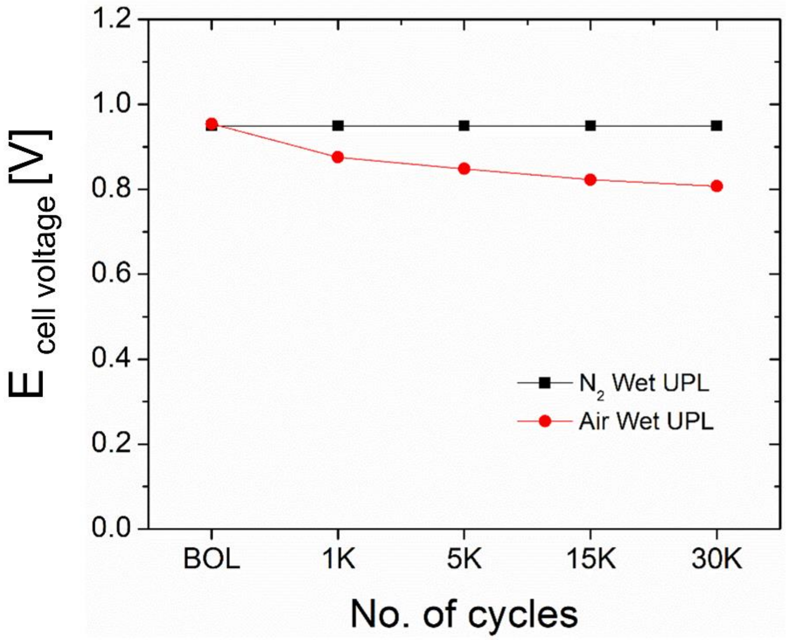

Figure 3.3 *UPL measured as a function of number of AST cycles for N_2 and Air environment ASTs. Reported UPL values have been averaged for the last 50 AST cycles of each stage.*

Chapter 2. The ASTs were conducted at 80°C cell temperature in 100% RH under atmospheric pressure. Three ASTs with different cathode GDLs (22BB, H23C6 and MB30) were conducted in hydrogen/nitrogen (anode/cathode) environment while the rest two ASTs (22BB and H23C6) were conducted in hydrogen/air environment. ASTs were repeated to ensure reproducible performance and confirm observations. **Figure 3.4 a** shows the voltage cycling profile for the nitrogen environment ASTs comprising 0.6 V LPL and 0.95 V of UPL with a dwell time of 3 seconds at each potential. **Figure 3.4 b** shows the voltage cycling profile for the air environment ASTs with OCV as the UPL. Gas flow rates of 0.2 slpm/0.2 slpm were used for both environment ASTs for cathode and anode gases, respectively. During the ASTs, each MEA was characterized after 0, 1000, 5000, 15000 and 30000 AST cycles.

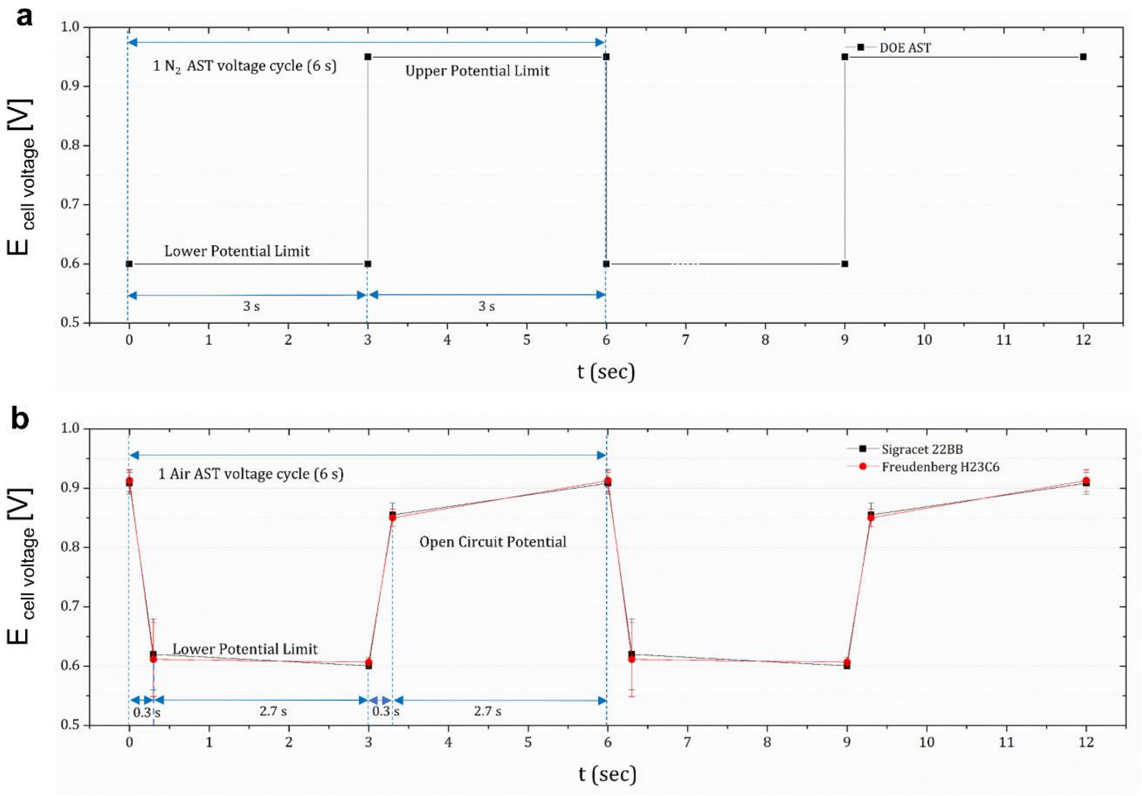

Figure 3.4 *a, Voltage cycle profile of nitrogen environment AST and b, voltage cycle profile of air environment AST.*

Chapter 3. The carbon corrosion AST was performed by cycling the potential from 1 V to 1.5 V with a scan rate of 500 mV.s^{-1} (cycle time of 2 seconds) for 2000 AST cycles. The RH was set at 100% with H_2 on anode and N_2 on cathode with flow rates of 0.2 slpm each under atmospheric pressure. During the AST, MEA I was characterized after only conditioning. MEA II was characterized after 0, 100 and 500 AST cycles while MEA III was characterized after and 0, 100, 500 and 2000 AST cycles. MEA IV (parallel channel flow field) was subjected to the same AST and was characterized after 0, 500 and 2000 AST cycles.

Chapter 4. The ASTs were performed at 80°C cell temperature in 100% RH under atmospheric pressure. As previously discussed, the cell voltage cycle for HDV AST comprises of 0.6 V LPL and 0.9 V of UPL with a dwell time of 3 seconds at each potential. Gas flow rates of 0.2 slpm and 0.2 slpm (H_2/N_2) were used for anode and cathode, respectively. During the AST, each MEA was characterized after 0, 10000, 30000, 60000 and 90000 AST cycles.

3.4. In-situ electrochemical characterization

Chapter 1. Cyclic voltammetry (CV) measurements were conducted with potential sweep from 0.095 V to 0.80 V at a scan rate of 20 $mV.s^{-1}$. Linear sweep voltammetry (LSV) was used to measure H_2 cross-over and were conducted from 0.05 V to 0.80 V at a scan rate of 1 mVs^{-1}. Electrochemical impedance spectroscopy (EIS) was done from 10 kHz to 0.01 Hz at 0 V vs. OCV with 5 points per decade. All the above-mentioned tests were performed in H_2/N_2 environment with 200 sccm/300 sccm flow rates at anode/cathode, with 100% relative humidity (RH) at atmospheric pressure. Polarization curves were generated by holding the cell at constant currents for 3 minutes and measuring the corresponding voltage values with six points in the activation region. Voltage values were averaged over these 3 minutes for both forward and backward scans. The test was performed at 150 kPa(a) backpressure with a stoichiometry of 1.5/1.8 in H_2/Air environment (anode/cathode) in 100% RH according to the fuel cell technical team (FCTT) polarization protocol. The polarization curves were preceded with a voltage recovery protocol, followed by holding the cell current density at 0.60 A cm^{-2}, at 80 ˚C, 100 % RH and with stoichiometry of 1.2/2.0 to ensure the polarization data is collected at the same starting conditions for all of the MEAs. The beginning of life (BOL) data was achieved by performing a cell break-in procedure on a fresh MEA which consisted of potential holds of 30 seconds at 0.80 V, 0.60 V and 0.30 V respectively until constant current was achieved. Mass activity measurements were only done at the BOL and at the end of life (EOL) by holding the cell potential at 0.90 V for 15 minutes, measuring the corresponding current in H_2/O_2 environment at high flow gas flow rates of 1000 sccm/2000 sccm and 150 kPa(a) backpressure. **Table 3.2** below summarizes the chronology and experimental details.

Table 3.2 *Testing procedure and sequence of electrochemical characterization experiments at each stage of the AST in chapter 1.*

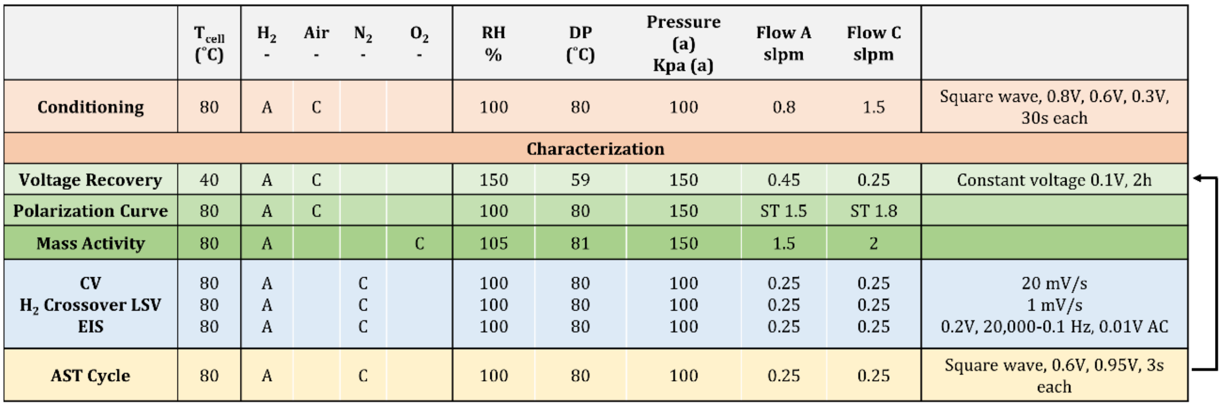

	T_{cell} (˚C)	H_2 -	Air -	N_2 -	O_2 -	RH %	DP (˚C)	Pressure (a) Kpa (a)	Flow A slpm	Flow C slpm	
Conditioning	80	A	C			100	80	100	0.8	1.5	Square wave, 0.8V, 0.6V, 0.3V, 30s each
Characterization											
Voltage Recovery	40	A	C			150	59	150	0.45	0.25	Constant voltage 0.1V, 2h
Polarization Curve	80	A	C			100	80	150	ST 1.5	ST 1.8	
Mass Activity	80	A			C	105	81	150	1.5	2	
CV **H_2 Crossover LSV** **EIS**	80 80 80	A A A		C C C		100 100 100	80 80 80	100 100 100	0.25 0.25 0.25	0.25 0.25 0.25	20 mV/s 1 mV/s 0.2V, 20,000-0.1 Hz, 0.01V AC
AST Cycle	80	A		C		100	80	100	0.25	0.25	Square wave, 0.6V, 0.95V, 3s each

Chapter 2, 3 and 4. CV, LSV and EIS were all collected in hydrogen/nitrogen environment at 80ºC in 100% RH under atmospheric conditions with gas flow rates of 1 slpm/1 slpm on the anode/cathode, respectively. CVs were collected with a potential sweep from 0.1 V to 1.2 V at a scan rate of 100 mV.s^{-1} while LSVs were collected from 0.05 V to 0.8 V at scan rate of 1 mV.s^{-1} to measure hydrogen crossover. EIS was measured at 0.2 V from 20 kHz to 0.1 Hz with 6 points per decade. Voltage break-in was performed at 80C in 100% RH under atmospheric pressure by cycling the voltage between 0.8 V, 0.6 V and 0.3 V (30 seconds each) for 200 cycles in a hydrogen /air environment. Voltage recovery consisted of voltage hold at 0.2 V for 1 hour at 40ºC in 150% RH under 150 kPa in a hydrogen/air environment. Polarization curves in hydrogen/air and hydrogen/oxygen environments were collected in differential conditions at 80ºC in 100% RH under 150 kPa absolute pressure with gas flow rates of 1 slpm/2.5 slpm at anode/cathode, respectively. For air, 4-minute holds from high current density (2 A.cm^{-2}) to low current density (0 A.cm^{-2}) were performed while for oxygen the holds consisted of 3 minutes from 0.75 V to OCV with increments of 25 mV. Average of the last minute was used to generate polarization curve (air) and Tafel plot (oxygen). Limiting current measurements were done for chapter 2 and 3 only, by holding potential from 0.3 V to 0.06 V using 0.5%, 1% and 1.5% concentrations of oxygen (balance nitrogen) at 80^{o}C in 75% RH under 120 kPa, 160 kPa and 200 kPa of absolute pressures with flow rates of 1 slpm/5 slpm at anode/cathode, respectively. The absolute pressures used for limiting current measurements in chapter 3 were 100 kPa, 150 kPa, 200 kPa and 250 kPa. The measured limiting current was then used to calculate the total oxygen mass transport resistance, pressure independent mass transport resistance and mass transport resistance at the Pt-ionomer interface based on procedures reported by Baker et al. [40] and Greszler et al. [41]. For chronology and detailed summary of each electrochemical characterization protocol in chapter 2 along with the ASTs see **Figure 3.5** and **Table 3.3**, respectively. For electrochemical characterization in chapter 3 and 4, see **Table 3.4** and **Table 3.5**, respectively.

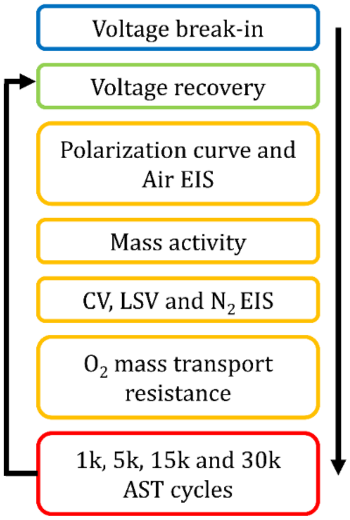

Figure 3.5 *Electrochemical characterization sequence in chapter 2.*

Table 3.3 *Details of electrochemical characterization protocols in chapter 2.*

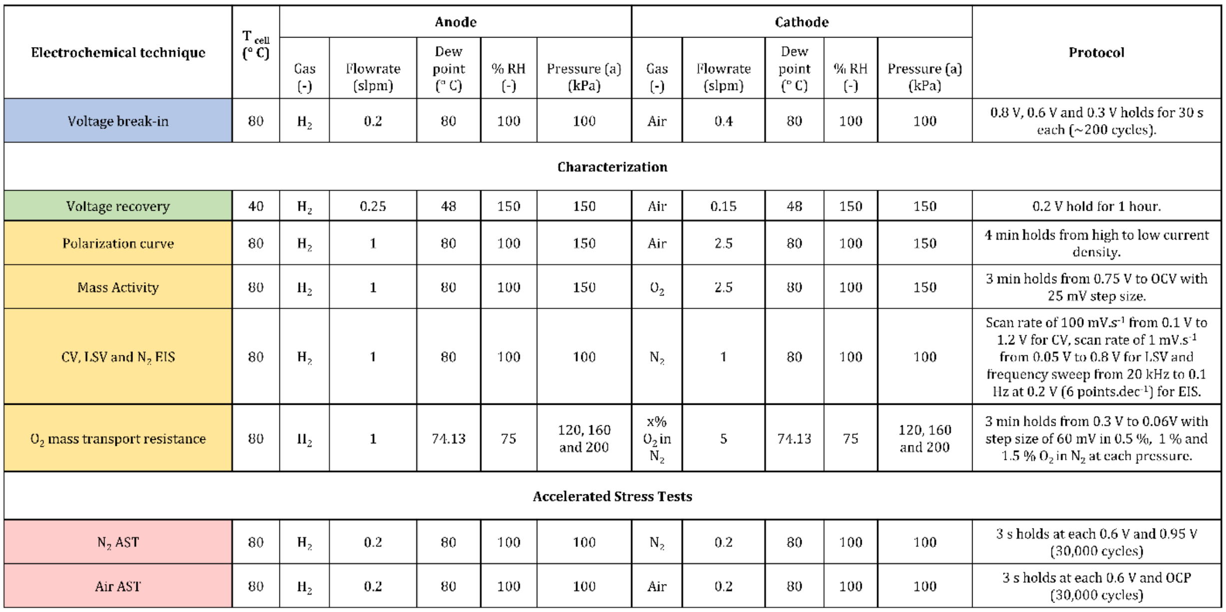

Electrochemical technique	T_{cell} (° C)	Anode					Cathode					Protocol
		Gas (-)	Flowrate (slpm)	Dew point (° C)	% RH (-)	Pressure (a) (kPa)	Gas (-)	Flowrate (slpm)	Dew point (° C)	% RH (-)	Pressure (a) (kPa)	
Voltage break-in	80	H_2	0.2	80	100	100	Air	0.4	80	100	100	0.8 V, 0.6 V and 0.3 V holds for 30 s each (~200 cycles).
Characterization												
Voltage recovery	40	H_2	0.25	48	150	150	Air	0.15	48	150	150	0.2 V hold for 1 hour.
Polarization curve	80	H_2	1	80	100	150	Air	2.5	80	100	150	4 min holds from high to low current density.
Mass Activity	80	H_2	1	80	100	150	O_2	2.5	80	100	150	3 min holds from 0.75 V to OCV with 25 mV step size.
CV, LSV and N_2 EIS	80	H_2	1	80	100	100	N_2	1	80	100	100	Scan rate of 100 $mV.s^{-1}$ from 0.1 V to 1.2 V for CV, scan rate of 1 $mV.s^{-1}$ from 0.05 V to 0.8 V for LSV and frequency sweep from 20 kHz to 0.1 Hz at 0.2 V (6 $points.dec^{-1}$) for EIS.
O_2 mass transport resistance	80	H_2	1	74.13	75	120, 160 and 200	x% O_2 in N_2	5	74.13	75	120, 160 and 200	3 min holds from 0.3 V to 0.06V with step size of 60 mV in 0.5 %, 1 % and 1.5 % O_2 in N_2 at each pressure.
Accelerated Stress Tests												
N_2 AST	80	H_2	0.2	80	100	100	N_2	0.2	80	100	100	3 s holds at each 0.6 V and 0.95 V (30,000 cycles)
Air AST	80	H_2	0.2	80	100	100	Air	0.2	80	100	100	3 s holds at each 0.6 V and OCP (30,000 cycles)

Table 3.4 *Details of electrochemical characterization and AST protocols in chapter 3.*

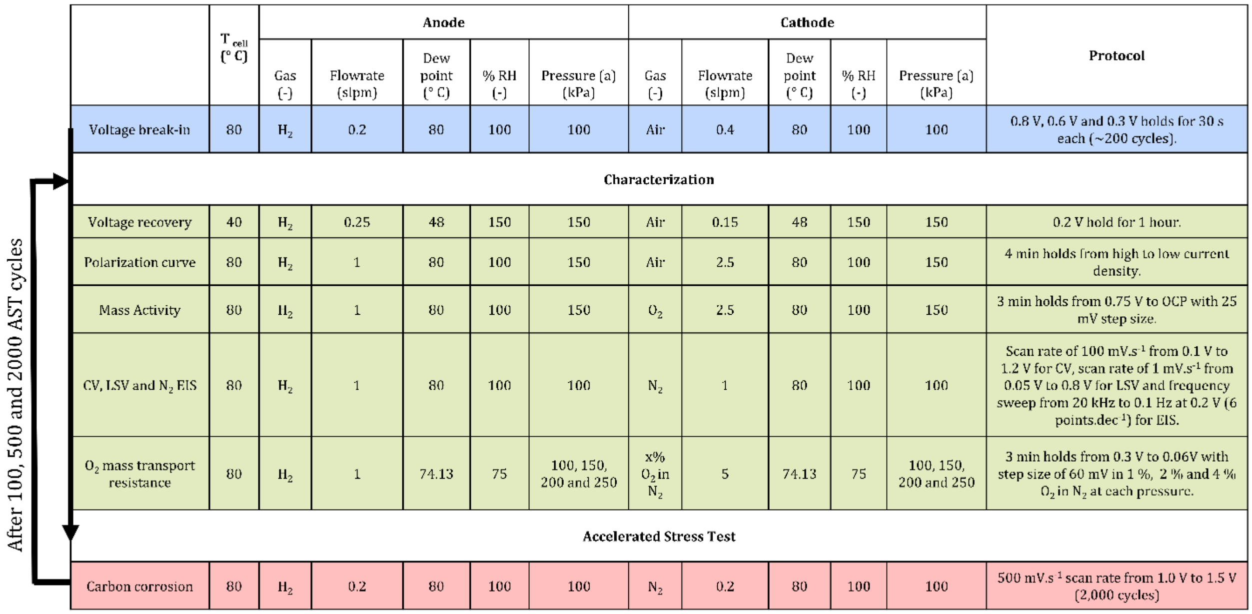

	T_{cell} (° C)	**Anode**					**Cathode**					**Protocol**
		Gas (-)	Flowrate (slpm)	Dew point (° C)	% RH (-)	Pressure (a) (kPa)	Gas (-)	Flowrate (slpm)	Dew point (° C)	% RH (-)	Pressure (a) (kPa)	
Voltage break-in	80	H_2	0.2	80	100	100	Air	0.4	80	100	100	0.8 V, 0.6 V and 0.3 V holds for 30 s each (~200 cycles).
Characterization												
Voltage recovery	40	H_2	0.25	48	150	150	Air	0.15	48	150	150	0.2 V hold for 1 hour.
Polarization curve	80	H_2	1	80	100	150	Air	2.5	80	100	150	4 min holds from high to low current density.
Mass Activity	80	H_2	1	80	100	150	O_2	2.5	80	100	150	3 min holds from 0.75 V to OCP with 25 mV step size.
CV, LSV and N_2 EIS	80	H_2	1	80	100	100	N_2	1	80	100	100	Scan rate of 100 $mV.s^{-1}$ from 0.1 V to 1.2 V for CV, scan rate of 1 $mV.s^{-1}$ from 0.05 V to 0.8 V for LSV and frequency sweep from 20 kHz to 0.1 Hz at 0.2 V (6 $points.dec^{-1}$) for EIS.
O_2 mass transport resistance	80	H_2	1	74.13	75	100, 150, 200 and 250	x% O_2 in N_2	5	74.13	75	100, 150, 200 and 250	3 min holds from 0.3 V to 0.06V with step size of 60 mV in 1 %, 2 % and 4 % O_2 in N_2 at each pressure.
Accelerated Stress Test												
Carbon corrosion	80	H_2	0.2	80	100	100	N_2	0.2	80	100	100	500 $mV.s^{-1}$ scan rate from 1.0 V to 1.5 V (2,000 cycles)

Table 3.5 *Details of electrochemical characterization and AST protocols in chapter 4.*

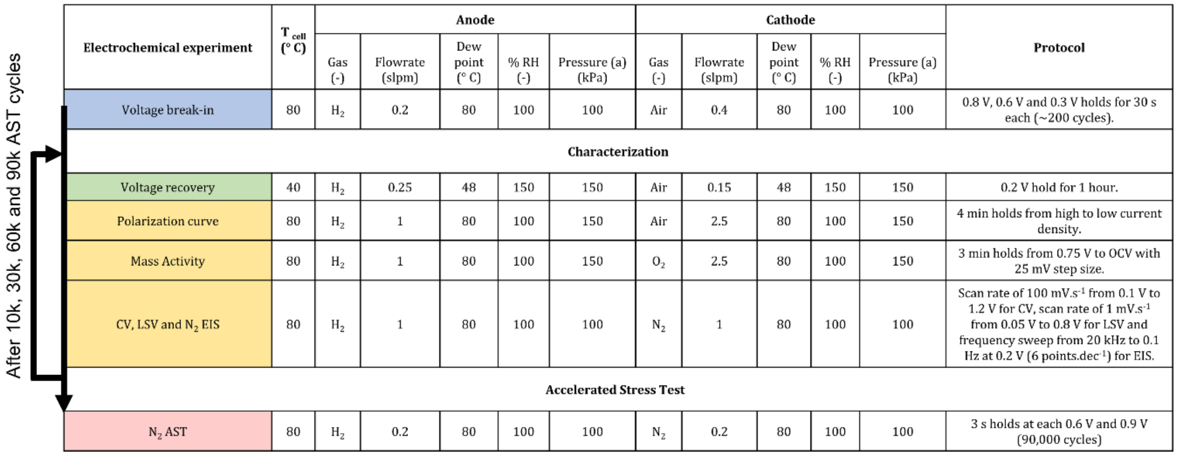

Electrochemical experiment	T_{cell} (° C)	**Anode**					**Cathode**					**Protocol**
		Gas (-)	Flowrate (slpm)	Dew point (° C)	% RH (-)	Pressure (a) (kPa)	Gas (-)	Flowrate (slpm)	Dew point (° C)	% RH (-)	Pressure (a) (kPa)	
Voltage break-in	80	H_2	0.2	80	100	100	Air	0.4	80	100	100	0.8 V, 0.6 V and 0.3 V holds for 30 s each (~200 cycles).
Characterization												
Voltage recovery	40	H_2	0.25	48	150	150	Air	0.15	48	150	150	0.2 V hold for 1 hour.
Polarization curve	80	H_2	1	80	100	150	Air	2.5	80	100	150	4 min holds from high to low current density.
Mass Activity	80	H_2	1	80	100	150	O_2	2.5	80	100	150	3 min holds from 0.75 V to OCV with 25 mV step size.
CV, LSV and N_2 EIS	80	H_2	1	80	100	100	N_2	1	80	100	100	Scan rate of 100 $mV.s^{-1}$ from 0.1 V to 1.2 V for CV, scan rate of 1 $mV.s^{-1}$ from 0.05 V to 0.8 V for LSV and frequency sweep from 20 kHz to 0.1 Hz at 0.2 V (6 $points.dec^{-1}$) for EIS.
Accelerated Stress Test												
N_2 AST	80	H_2	0.2	80	100	100	N_2	0.2	80	100	100	3 s holds at each 0.6 V and 0.9 V (90,000 cycles)

3.5. Analysis of electrochemical data

3.5.1. Electrochemically Active Surface Area calculation

The ECSA was calculated using the standard hydrogen underpotential deposition (H_{UPD}) region, where the area under the H_{UPD} region of the CV (**Figure 3.6**), was integrated to acquire the ECSA using equation below:

$$ECSA = \frac{i \times V}{L \times \upsilon \times 210} \qquad 3.1$$

where, the nominator represents the area of the H_{UPD} region in the CV, *L* is the loading of the electrocatalyst, 210µC.cm^{-2} is the unit charge and *υ* is the scan rate under which the CVs were performed.

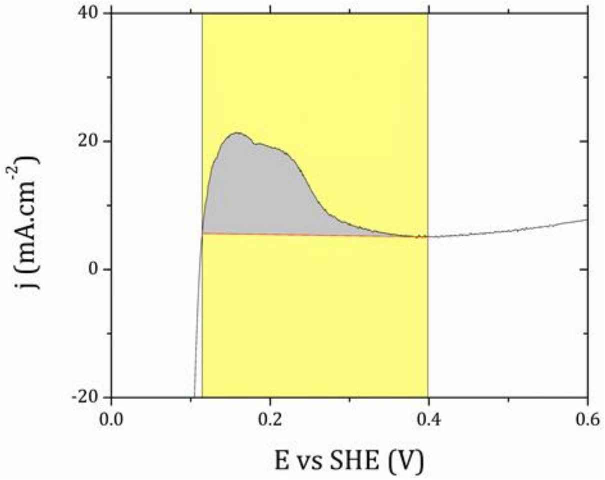

Figure 3.6 *Integrated area (gray) highlighting hydrogen desorption peak area from the CV used to calculate the ECSA using equation 3.1.*

3.5.2. Hydrogen crossover current density

H_2 crossover current density is measured by LSV. This current is added as a correction in the H_2/O_2 polarization curve to get a proper estimate of Tafel slope and exchange current density. It is also used to ensure that the fuel cell has been assembled correctly.

For instance, **Figure 3.7** and the **Table 3.6** show the LSV plots, and the current densities used for crossover correction respectively in chapter 3 results. Typical values can range from 1 to 5 mA.cm^{-2} depending upon the membrane thickness and type (reinforced or non-reinforced).

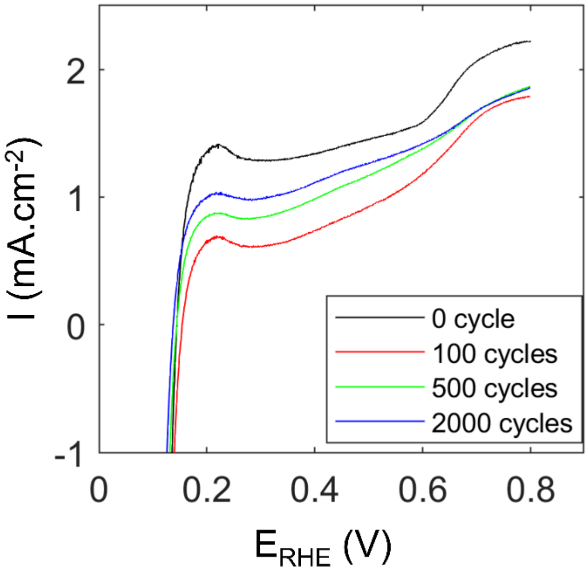

Figure 3.7 Linear sweep voltammetry data at BOL, after 100, 500 and 2000 AST cycles in chapter 3.

Table 3.6 Values of crossover current density used for correction to generate Tafel plots in chapter 3.

AST stage	**$I_{crossover}$ (mA.cm^{-2})**	**$\Delta I_{crossover}$ (mA.cm^{-2})**
BOL	2.15	0.05
100 AST cycles	1.53	0.22
500 AST cycles	1.65	0.25
2000 AST cycles	1.6	

3.5.3. Fitting electrochemical impedance spectroscopy with transmission line model

To fit the electrical impedance spectroscopy data for a porous electrode, a transmission line model is required rather than a Randle's circuit. A transmission line can be thought to be a collection of a large number of Randle's circuits consisting of infinitesimally small electrical circuit components like ion transport resistance, double layer capacitance, charge transfer resistance etc. A typical transmission line circuit looks like the one shown in **Figure 3.8**.

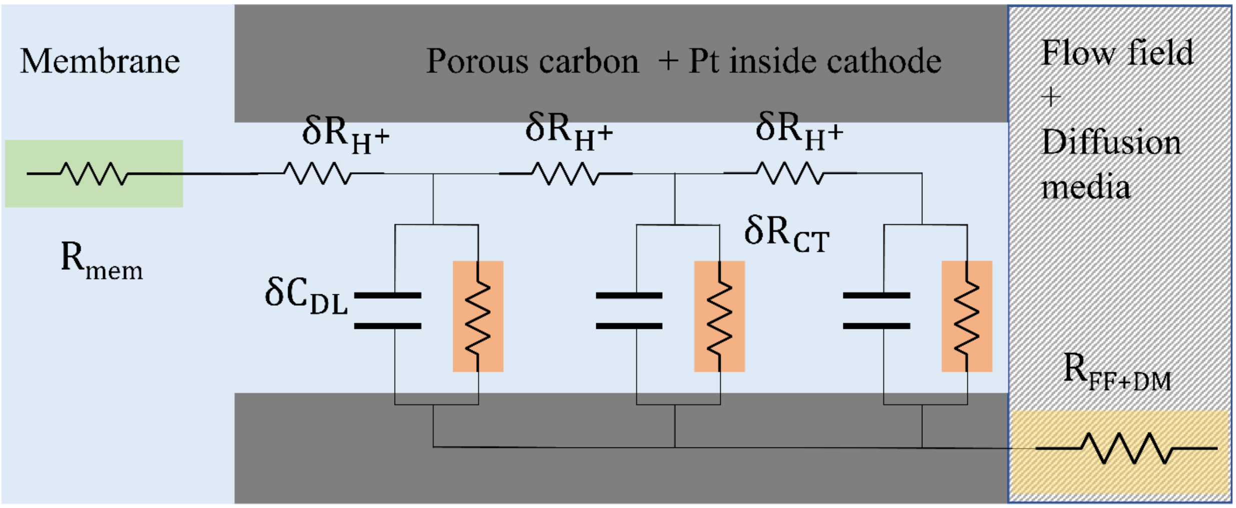

Figure 3.8 *Schematic of a transmission line setup for a PEFC electrode.*

Figure 3.8 shows three regions of interest for fitting EIS data of a porous cathode catalyst layer in PEFC - the membrane, cathode catalyst layer, diffusion media (DM) and the flow field (FF). R_{mem} is denoted as the bulk H^+ transport resistance through the membrane and R_{FF+DM} is the electronic resistance. The cathode catalyst layer also has some electronic resistance, but it is usually negligible compared to the H^+ transport resistance inside the cathode catalyst layer. Inside cathode catalyst layer, $R_{Sheet} = N \times \delta R_{H^+}$ and $C_{Sheet} = N \times$

δC_{DL} with $N \to \infty$ where N is the number of circuit elements. R_{Sheet} and C_{Sheet} are the overall proton transport resistance and capacitance in the cathode catalyst layer. These are macroscopic quantities that can be related to experiments. The EIS was performed with H_2/N_2 at anode/cathode. In this configuration, $\delta R_{CT} \to \infty$. Hence, charging of the electrode is mostly capacitive. In practice, charge transfer resistances due to Faradaic reactions like ionomer adsorption, H oxidation (crossover H_2) can show some impact at low frequency limit. However, in the high frequency limit, the above-mentioned assumptions work pretty well. The net impedance formula is [42,43]:

$$Z = j\omega L + R_{Ohmic} + \sqrt{\frac{R_{Sheet}}{j\omega C_{Sheet}}}\coth\left(\sqrt{j\omega R_{Sheet} C_{Sheet}}\right) \qquad 3.2$$

In equation (3.2) above, $j = \sqrt{-1}$, $\omega = 2\pi\nu$ is the angular speed, and L = inductance coming from the electrical wires. $R_{Ohmic} = R_{mem} + R_{FF+DM}$. EIS data are fit to this formula using Levenberg-Marquardt technique by implementing a modulus-weighted complex nonlinear least-squares fitting method for data fitting and error estimates. Opensource Impedance Fitter (OSIF) [44], a python-based script was used. With the values of R_{Sheet} and R_{Ohmic}, one can do the iR correction as below:

$$\eta_{Ohmic} = i \times R_{eff} = i \times \left\{R_{Ohmic} + \frac{R_{Sheet}}{3}\right\} \qquad 3.3$$

3.5.4. Tafel slope and concentration overpotentials from H_2/O_2 polarization curve

To calculate the concentration overpotential, first, the reversible potentials for H_2/O_2 and H_2/air case need to be calculated. Nernst equation for ORR can be written as:

$$E_{rev} = 1.23 - 0.0009(T - 298) + \frac{2.303RT}{4F}\log\left[\left(\frac{P_{H_2}}{P_{H_2,ref}}\right)^2\left(\frac{P_{O_2}}{P_{O_2,ref}}\right)\right] \qquad 3.4$$

where $P_{H2,ref}$ and $P_{O2,ref}$ are 1 atm each. These are the reference partial pressures at which the P independent quantities were calculated. (T-298) term is the temperature correction that comes from the temperature dependence of Gibbs free energy for ORR. For PEFC experiments, T = 353 K. The gas feeds (H_2 and O_2) are both 100% humidified. So, pressure of saturated water vapor has to be subtracted from the set backpressure to get the pressure of dry gas.

At T= 353 K, the pressure of saturated vapor pressure is = P_{sat} (80° C) = 47.343 kPa.

So, pressure of dry H_2 = P_{H2} = 151.988 – 47.343 kPa = 104.645 kPa.

For H_2/O_2 polarization curve, pressure of dry O_2 = P_{O2} = 151.988 – 47.343 kPa = 104.645 kPa.

Substituting all these values to equation (3.4), we get E_{rev} for H_2/O_2 polarization curves to be (vs RHE):

$$E_{rev}(H_2|O_2) = 1.23 - 0.0495 + 0.0175 \times \log\left(\left[\frac{104.645}{101.325}\right]^3\right) = 1.181\ V$$

3.5.4.1. Calculation of Tafel slope

First, the Butler-Volmer relation can be written in a way prescribed by Gasteiger *et al.* [45]. The advantage of that way of writing the equation is that it is easy to relate with experimental parameters. It is also quite convenient for degradation studies, as one can isolate the quantities that can vary with degradation.

$$\mathrm{i} = \mathrm{i}_0\left(\mathrm{P}_{\mathrm{O}_2}, \mathrm{T}\right) \times \mathrm{RF}^{(\mathrm{k})} \times 10^{\frac{\eta_{\mathrm{kin}}^{(\mathrm{k})}}{\mathrm{b}}} \qquad 3.5$$

In equation (3.5), i_0 is the exchange current density which depends on the catalyst nature, support structure, temperature and also on the partial pressure of O_2. The dependence on partial pressure of O_2 comes from the reaction order, which is approximately thought to be close to 0.5 [46]. rf stands for the roughness factor which is the ratio between Pt ECSA and the geometric cell area. This is known for all AST stages. The current 'i' on the left-hand side has the unit of $\mathrm{A.cm_{geo}^{-2}}$ normalized to the cell geometric area. As rf is the ratio of Pt ECSA to the geometric active area ($\mathrm{cm_{Pt}^{2}.cm_{geo}^{-2}}$), the unit of i_0 is $\mathrm{A.cm_{Pt}^{-2}}$, i.e., it is normalized to the physical area of the Pt particles. η_{kin} refers to the kinetic overpotential. The superscript (k) denotes the AST stage. The advantage of writing the Butler-Volmer equation like equation (3.5) is that- the effect of degradation that is relevant in the kinetic region, i.e., loss of ECSA, and hence roughness can be isolated. The equation (3.5) also easily shows that for the same current density i, the kinetic overpotential η_{kin} changes at different AST stages. As usual, 'b' refers to the Tafel slope.

Using H_2/O_2 polarization curve at BOL, one can get BOL $\eta_{kin}(i)$ directly from the cell voltage data. Using the superscript 0 to represent the BOL data, we can write:

$$\eta_{\mathrm{kin}}^{(0)}(\mathrm{i}) = \eta^{(0)} - \eta_{\mathrm{Ohmic}}^{(0)} = \mathrm{E}_{\mathrm{rev}} - \mathrm{E}_{\mathrm{cell}}^{(0)}(\mathrm{i}) - \mathrm{i} \times \left(\mathrm{R}_{\mathrm{Ohmic}}^{(0)} + \frac{1}{3}\mathrm{R}_{\mathrm{Sheet}}^{(0)}\right) \qquad 3.6$$

In equation (3.6), $\eta^{(0)}$ is the experimentally measured overpotential, $\mathrm{E}_{\mathrm{cell}}^{(0)}(\mathrm{i})$ is the measured cell voltage at a particular current density. E_{rev} is 1.181 V. The most important assumption in equation (3.5) is that at BOL, the concentration overpotential, i.e., $\eta_{\mathrm{conc}}^{(0)} \approx 0$. This is certainly an approximation and ignores the contribution from unassigned voltage losses, but it is a common one used to calculate kinetic parameters in PEFCs. To make this approximation more justified, H_2/O_2 polarization curves are performed in differential conditions. With this definition of kinetic overpotential at BOL, one can rewrite the equation (3.6) to get the Tafel slope and exchange current density i_0:

$$\mathrm{E}_{\mathrm{cell}}^{(0)} = \mathrm{E}_{\mathrm{rev}} - \mathrm{i} \times \left(\mathrm{R}_{\mathrm{Ohmic}}^{(0)} + \frac{1}{3}\mathrm{R}_{\mathrm{Sheet}}^{(0)}\right) - \mathrm{b} \times \log \mathrm{i} + \mathrm{b} \log \mathrm{i}_0 + \mathrm{b} \log \mathrm{RF}^{(0)} \qquad 3.7$$

From, equation (3.7), first, ‘b’ is estimated from the iR corrected curve (the first two terms on the right-hand side of the equation) and log(i) plot. Experimentally, it is 71 mV/dec which is almost equal to the value found by Neyerlin et al. [47] for Pt/HSAC catalyst. Then, from the calculated Tafel slope, the exchange current density i_0 is calculated.

3.5.4.2. Calculation of concentration overpotential in H_2/O_2 setup

It is already well-known in the electrochemistry literature that mass transport limitation can cause wrong estimation of kinetic parameters. In the electrochemical corrosion industry specifically, this issue has been historically very important. Many innovative techniques have been developed to systematically remove the mass transport effects in the kinetic region. Often mass transport corrections are necessary to estimate kinetic parameters. In PEFCs, O_2 mass transport limitation is reduced by experimental setups- doing polarization curve in H_2/O_2 instead of H_2/air and high flow rate. This setup usually gives good results at the BOL. However, after carbon corrosion, O_2 MTR increases significantly. So, the same setup (flow rate, backpressure etc.) may not be sufficient to compensate the increasing MTR after carbon corrosion. The increasing concentration overpotential with number of AST cycles can be explicitly calculated, with the logical assumption, that Tafel slope remains constant (BOL value of ~ 70 mV/dec) in the following way:

At any AST stage, equation (3.5) is valid. If one writes down the equation (3.5), with the same current density at BOL and another AST stage 'k', one gets:

$$\mathrm{i} = \mathrm{i}_0\left(\mathrm{P}_{\mathrm{O}_2}, \mathrm{T}\right) \times \mathrm{RF}^{(\mathrm{k})} \times 10^{\frac{\eta_{\mathrm{kin}}^{(\mathrm{k})}}{\mathrm{b}}} = \mathrm{i}_0\left(\mathrm{P}_{\mathrm{O}_2}, \mathrm{T}\right) \times \mathrm{RF}^{(0)} \times 10^{\frac{\eta_{\mathrm{kin}}^{(0)}}{\mathrm{b}}} \qquad 3.8$$

Equation (3.8) is convenient to use as polarization curves (both H_2/O_2 and H_2/air) are performed at known current densities which are kept the same. $\eta_{\mathrm{kin}}^{(0)}$ can be obtained from the H_2/O_2 polarization curve data using equation (3.6). Thus, knowing $\eta_{\mathrm{kin}}^{(0)}$, one can predict $\eta_{\mathrm{kin}}^{(\mathrm{k})}$ from:

$$\eta_{\mathrm{kin}}^{(\mathrm{k})} = \eta_{\mathrm{kin}}^{(0)} + \mathrm{b} \times \log\left\{\frac{\mathrm{RF}^{(0)}}{\mathrm{RF}^{(\mathrm{k})}}\right\} \qquad 3.9$$

In equation (3.9), rf values are known at all AST stages. Tafel slope ‘b’ is set constant at the BOL value of ~ 70 mV.dec^{-1}. The exchange current density does not change as it is a catalyst specific parameter. In addition, ohmic overpotential can be easily estimated as:

$$\eta_{\text{Ohmic}}^{(k)} = i \times \left(R_{\text{Ohmic}}^{(k)} + \frac{1}{3} R_{\text{Sheet}}^{(k)} \right) \qquad 3.10$$

The data for R_{Ohmic} and R_{Sheet} can be known for all stages from EIS measurements. So, the remaining overpotential, i.e., concentration overpotential coming from O_2 mass transport limitation can be found from:

$$\eta_{\text{conc}}^{(k)} = \eta^{(k)} - \eta_{\text{kin}}^{(k)} - \eta_{\text{Ohmic}}^{(k)} = \left\{ E_{\text{cell}}^{(0)}(i) - E_{\text{cell}}^{(k)}(i) \right\} - b \times \log\left\{ \frac{RF^{(0)}}{RF^{(k)}} \right\} \qquad 3.11$$
$$- i \times \left(\left[R_{\text{Ohmic}}^{(k)} - R_{\text{Ohmic}}^{(0)} \right] + \frac{1}{3}\left[R_{\text{Sheet}}^{(k)} - R_{\text{Sheet}}^{(0)} \right] \right)$$

In equation (3.11), we have combined the equations (3.6), (3.9) and (3.10). Note that equation (3.11) is written in such a way that it only contains those parameters that are directly found from the experiments. Applying equation (3.11) to the H_2/O_2 polarization curve with the known parameters allows to calculate concentration overpotential at different current densities.

3.5.5. Concentration overpotentials from H_2/air polarization curve

To calculate the concentration overpotentials, firstly the reversible potential for H_2/air setup is needed. It can be calculated from equation (3.4). The only difference with the previous calculation for H_2/O_2 setup is in the O_2 partial pressure. In air, O_2 consists approximately 1/5th of the number density. Saturated vapor pressure, again, is 47.343 kPa at 80° C. The set backpressure at anode and cathode is 1.5 atm or 151.988 kPa.

So, for H_2/air polarization curve, pressure of dry O_2 = P_{O2} = 1/5 * (151.988 - 47.343) = 20.929 kPa.

Thus, for H_2/air polarization curve (vs RHE) from equation (3.4):

$$\mathrm{E_{rev}(H_2|air)} = 1.23 - 0.0495 + 0.0175 \times \log\left(\left[\frac{104.645}{101.325}\right]^2 \times \left[\frac{20.929}{101.325}\right]\right) = 1.1685\ \mathrm{V}$$

Tafel slope and the exchange current density can be determined from data in oxygen. So, one can estimate the kinetic overpotential $\eta_{\mathrm{kin}}^{(k)}$ at any stage of AST using equation (3.5). $\eta_{\mathrm{Ohmic}}^{(k)}$ can also be calculated from the known values of R_{Ohmic} and R_{Sheet} at different AST stages. Experimentally, one can measure the overpotential $\eta^{(k)}(\mathrm{i})$ at any current density. From these quantities, one can estimate the concentration overpotential at any stage of AST.

$$\eta_{\mathrm{conc}}^{(k)}(\mathrm{i}) = \eta^{(k)}(\mathrm{i}) - \eta_{\mathrm{kin}}^{(k)}(\mathrm{i}) - \eta_{\mathrm{Ohmic}}^{(k)}(\mathrm{i}) = \mathrm{E_{rev}} - \mathrm{E_{cell}^{(k)}}(\mathrm{i}) - \mathrm{b} \times \log\left[\frac{\mathrm{i}}{\mathrm{i_0} \times \mathrm{RF}^{(k)}}\right] - \mathrm{i} \times \left(\mathrm{R_{Ohmic}^{(k)}} + \frac{1}{3}\mathrm{R_{Sheet}^{(k)}}\right) \qquad 3.12$$

Thus, from equation (3.12), concentration overpotential at BOL can be explicitly calculated and need not be approximated as 0. Note that in H_2/O_2 setup, the approximation of $\eta_{\mathrm{conc}}^{(0)}(\mathrm{i}) = 0$ is necessary, otherwise the kinetic parameters cannot be calculated as no exact analytical formula for concentration overpotential that can applied to PEFC exists in literature.

3.6. Ex-situ analytical characterization

3.6.1. Scanning electron microscopy

Scanning electron microscopy (SEM) was performed to identify degradation of Pt nanoparticles and to identify morphological changes of the catalyst layer due to degradation. The following procedure was followed to obtain sample cross-sections from the SEM. First, an area of about 1 cm × 1 cm in the middle of the MEA was cut from the MEA, which was then sandwiched between stainless steel or glass plate to keep flat. The assembly was then mounted in epoxy and sectioned to expose the cross-section. Multiple Buehler EcoMet 30 polishing paper were used to polish the cross-section with finish progressively increasing from 320 grit to 1200 grit. The polished cross-section was imaged in a JOEL-7200F field emission scanning electron microscope, equipped with an Oxford Instruments X-MaxN EDS detector. Catalyst layer thickness measurement was carried out using ImageJ. Multiple measurements were taken at various locations across the entire 1 cm length of the cross-section.

3.6.2. Focused ion beam scanning electron microscopy

To perform focused ion beam scanning electron microscopy (FIB-SEM), the cathode-side GDL was carefully peeled off the MEA to expose the cathode catalyst layer. The sample was then affixed to an SEM pin mount using carbon tape. The FEI Quanta 3D, a dual-beam FIB/SEM instrument, was used for this analysis. The liquid gallium metal ion beam source was operated at an accelerating voltage of 30 kV, while the electron beam parameters were 10 kV and 93 pA. The sample stage was tilted at 52° such that the incident ion beam is perpendicular to the sample surface for slicing. A protective Pt layer, roughly one micron thick, was deposited on the surface of the catalyst layer. Side trenches and rough cuts to expose the surface of interest were milled at 500 pA, with several cleaning cuts performed at 30 pA to shave off destructed portions of the catalyst layer. With the given electron beam energy, the planar resolution of the SEM was 10 nm.

After preparation, approximately 10 μm x 2 μm x 10 μm (length x width x depth) volume was investigated as the region of interest (ROI) via a combination of FEI's Auto Slice and View program and manual SEM imaging. A 20-nm slice of the ROI was milled by the ion beam at 30 pA, followed by imaging with the electron beam under vacuum. Following image acquisition, the SEM micrographs were registered and aligned using Fiji ImageJ and the StackReg plug-in [48]. A portion of the ROI was then cropped and converted to 8-bit. An FFT bandpass filter was applied to eliminate any vertical striation artifacts from the ion beam slicing. To achieve accurate thresholding, the image contrast was increased to elucidate the difference between solid and void volume. Once the pore area is elucidated, the porosity of each slice and the overall image stack can be calculated. Because of the SEM resolution, 10 nm was used as the bin size for pore diameter distribution. The in-plane and through-plane pore-space tortuosity factors of the pores were calculated using the Tau Factor [49] add-on in MATLAB. Three-dimensional reconstruction of the cathode catalyst layer was accomplished using Dragonfly software. A pore space rendering was generated with the OpenPNM [50] workflow, and a pore size distribution for the cathode catalyst layer was obtained. In-house MATLAB scripts and the Curve Fitting application were used to plot probability density functions to fit the pore size distribution histograms.

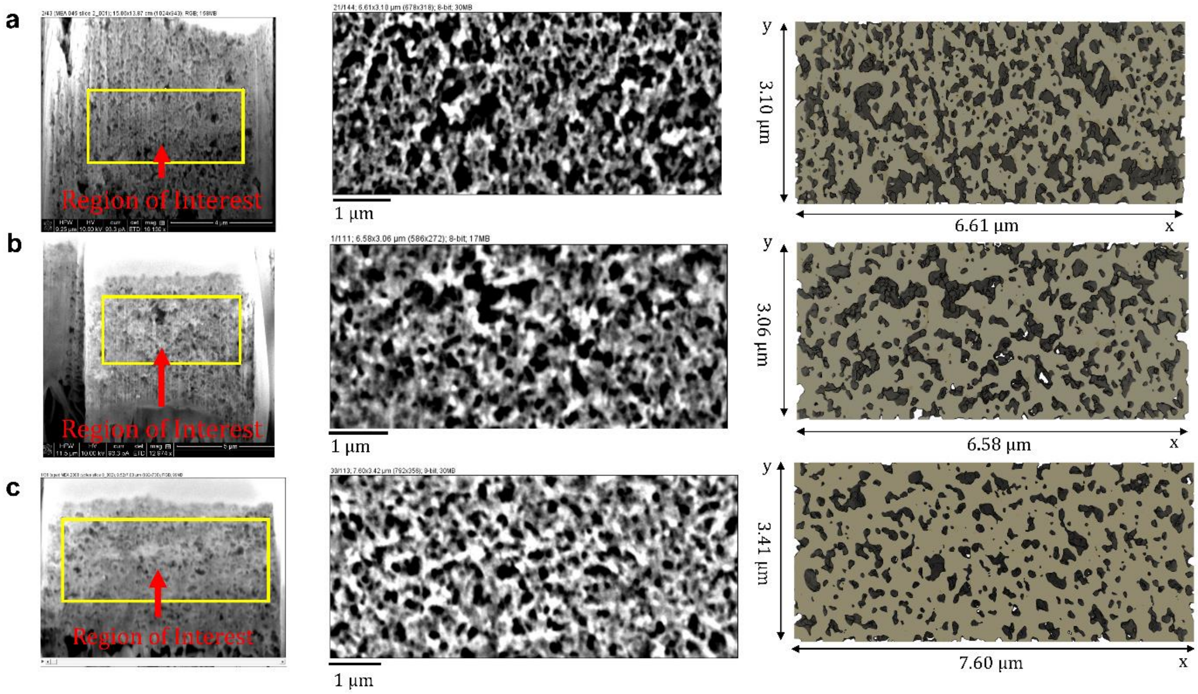

Figure 3.9 *a, BOL b, 500 AST cycles and c, 2000 AST cycles. The first column shows the region of interest used for analysis from the raw FIB-SEM images. The region of interest excludes the areas that are either too close to the membrane or the platinum capping layers. The second column shows the raw grayscale images. The third column shows the segmented images. The color indicates solid phase (platinum, ionomer, and carbon).*

The critical part about FIB-SEM analysis is finding the right contrast so that the pore space is properly visible. An SEM image fundamentally shows contrast between the solid and the void phase. When viewing an image slice, the next image slice may also affect the overall interpretation. For instance, if there is a layer of solid material just behind a pore, the pore may effectively look like a solid of slightly different contrast. In **Figure 3.9** and **Figure 3.10**, solid is denoted by white and the void is denoted by dark colors. At low contrast, pores were not sometimes visible because of the solid layer behind. The contrast was increased to account for this issue. If the contrast is too high, the solid substances with lower density will appear dark, and as a result, will be interpreted as void. So, at very low contrast, the pores are under-counted. At very high contrast, the pores are over-counted. For the final data analysis, an intermediate contrast setting was chosen to correctly estimate the pore volume.

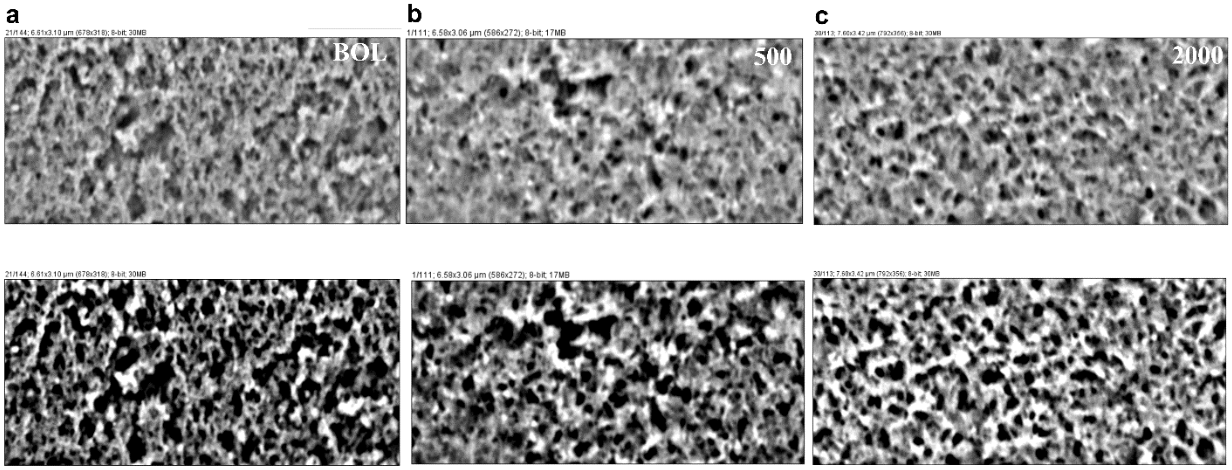

Figure 3.10 *Role of contrast adjustment for a proper analysis of pore-space at a, BOL b, 500 AST cycles and c, 2000 AST cycles (contrast adjusted below).*

After proper segmentation, the images consist of correct pore and solid volumes. Local thickness procedure is performed on the pore-space to inscribe spherical kernels into each pore. Essentially, the largest possible sphere is being fit into the pore, and those voxels that belong to this sphere are ascribed to the diameter of the fit sphere. The pore-size distribution histogram is generated Then a bimodal log-normal distribution is fit to the discrete pore size distribution. Inside fuel cell catalyst layers, a bimodal pore size distribution is observed experimentally. The larger pores, known as the primary pores, are the void spaces between the carbon agglomerates. The smaller pores, called the secondary pores, are the void spaces inside each agglomerate. Uchida et al. were the first to suggest a bimodal pore size distribution inside catalyst layers from the mercury intrusion porosimetry data [51]. Log-normal distribution is usually fitted to the pore volume data of gas diffusion layers in fuel cell [19]. As a result, this can be used in the study for the pore size distributions inside the catalyst layer as well. The following formula is used for fitting:

$$\mathrm{PDF}\ (\mathrm{r}) = \sum_{\mathrm{k}=1,2} \mathrm{f}_{\mathrm{r,k}} \left\{ \frac{1}{\sqrt{2\,\pi}\,\mathrm{r}\,\sigma_{\mathrm{k}}} \exp\left[-\frac{\left(\ln \mathrm{r} - \ln \mathrm{r}_{\mathrm{o,k}}\right)^2}{2\sigma_{\mathrm{k}}^2} \right] \right\} \qquad 3.13$$

In equation (3.13), PDF stands for the probability density function. $f_{r,k}$ denotes the weight of the k'th distribution with the mean $r_{0,k}$ and the standard deviation σ_k. Clearly $f_{r,1} + f_{r,2} = 1$. The distribution mean is ($f_{r,1}*r_{0,1} + f_{r,2}*r_{0,2}$). There are two mean diameter and standard deviation values that can be reported- 1) quantities calculated from the segmented images itself, and 2) quantities calculated from the log-normal fits. The following data obtained for the pore size distribution at different stages of carbon corrosion (chapter 3) shown in **Table 3.7** is an example.

Table 3.7 *Fitting parameters at BOL, after 500 AST cycles and after 2000 AST cycles.*

Parameter	**Value at BOL**	**Value after 500 AST cycles**	**Value after 2000 AST cycles**
Mean diameter (nm)	50.6	72.1	55.7
Mode (nm)	22.1	48.0	40.9

Standard deviation (nm)	33.2	39.1	31.0
R^2 value	0.8	0.7	0.7
σ_1 (nm)	0.6	0.7	0.7
σ_2 (nm)	0.6	0.5	---
$r_{0,1}$ (nm)	55.6	61.1	56.8
$r_{0,2}$ (nm)	31.4	78.1	----
$f_{r,1}$ (nm)	0.8	0.6	1.0

3.6.3. Non-dispersive infra-red spectroscopy

For non-dispersive infra-red (NDIR) spectroscopy the effluent stream from the cathode was split and one end of it was connected to the IAQ-CALC^{TM} model 7545 NDIR sensor (TSI Incorporated, Shoreview, MN) during the AST cycles. This allowed for accurate and reproducible measurement of carbon dioxide and carbon monoxide ppm in the effluent stream as a function of time. The data was collected at every 2 seconds from the start of AST voltage cycling until the ppm values reached the initial baseline to account for all the residual oxidized carbon ppm. This data was utilized to estimate carbon loss in μg.cm^{-2} of active area.

During carbon corrosion AST (1-1.5 V voltage cycling), the anode feed was 100% humidified H_2 and the cathode feed was 100% humidified N_2 at 80 C (353 K). The flow rate was 0.2 slpm for both anode and cathode. Flow pressure was 1 atm absolute. It was assumed that the inlet and outlet flow rate at the cathode were same. However, the number flow rate was different, and can be calculated as follows:

$$\left.\frac{dN}{dt}\right|_{in} = \left.\frac{dN_{N_2}}{dt}\right|_{in} + \left.\frac{dN_{vapor}}{dt}\right|_{in} \qquad 3.14$$

$$\left.\frac{dN}{dt}\right|_{out} = \left.\frac{dN_{N_2}}{dt}\right|_{in} + \left.\frac{dN_{vapor}}{dt}\right|_{out} + \left.\frac{dN_{CO_2}}{dt}\right|_{out} + \left.\frac{dN_{CO}}{dt}\right|_{out} \qquad 3.15$$

In the equations (3.14) and (3.15), it was implicitly assumed that dN_{N2}/dt is same at both inlet and outlet as N_2 does not react. $\left.\frac{dN_{vapor}}{dt}\right|_{out} < \left.\frac{dN_{vapor}}{dt}\right|_{in}$ as water vapor reacts with C to form CO and CO_2. The experimental data shows that CO_2 is produced at much larger amount than CO. This happens because the potential applied, 1-1.5 V is higher than the known CO oxidation potential. So, the produced CO gets oxidized to CO_2. The NDIR sensor measures ppm level of CO_2 and CO. The CO_2 and CO ppm readings can be converted to the C mass lost. First, the mass of CO_2 produced from the measured ppm data is estimated as:

$$m_{CO_2}(cycle) = \int_{\text{AST start time}}^{\text{time } CO_2 \text{ returns base level}} \frac{dV}{dt} n_{tot}\left(ppm_{CO_2} - ppm_{CO_2,baseline}\right) M_{CO_2}\, dt \qquad 3.16$$

$$m_{CO}(cycle) = \int_{\text{AST start time}}^{\text{time CO returns base level}} \frac{dV}{dt} n_{tot}\left(ppm_{CO} - ppm_{CO,baseline}\right) M_{CO}\, dt \qquad 3.17$$

In equations (3.16) and (3.17), dV/dt is the volume flow rate (0.2 slpm). The net molar density of outgoing species n_{tot} is given by $n_{tot} = n_{N_2} + n_{vapor} + n_{CO_2} + n_{CO}$. Among all the quantities, n_{CO} is the most negligible. The baseline ppm level of CO_2 and CO was subtracted because before AST, i.e., before any significant production of CO_2 or CO due to AST, the baseline ppm levels were not 0. Thus, it had to be subtracted from the observed ppm level to estimate the correct ppm of CO_2 and CO that was produced due to the AST. Another important aspect of equations (3.16) and (3.17) are the upper limit of the integration. It was observed that the ppm levels return to the baseline after some time once the AST stops. The fuel cell operation was kept in idle mode until the ppm levels return to the baseline values. The integration was carried out until that time.

The back pressure was kept at 1 atm during the time. Here $P_{back} = P_{gas} + P_{vapor}$. P_{vapor} = saturated vapor pressure at 80° C = 47.343 kPa, which is about half of the back pressure (1 atm = 100 kPa). So, the contribution of water vapor at this high RH cannot be neglected at all. In the expression of total molar density $\mathrm{n_{N_2} + n_{CO_2} + n_{CO} = n_{ideal}}$ where the N_2, CO, and CO_2 can be assumed to be ideal gases, and can be estimated as $\mathrm{n_{ideal} = \frac{P_{ideal}}{RT} = \frac{P_{back} - P_{vapor}}{RT} = \frac{P_{back} - P_{sat}}{RT}}$ = 18.4 mol/m^3. Density of saturated water vapor is 293.8 gm/m^3, and the molar density of saturated vapor at 80 C = 293.8 gm/m^3 / 18.02 gm/mol = 16.3 mol/m^3. So, the molar density of water vapor is almost similar to that of ideal gas. This is also expected as the vapor pressure was almost half of the back pressure. So, the saturated vapor pressure was almost equal to the pressure exerted by the ideal gas inside the NDIR chamber.

With these calculations, equations (3.16) and (3.17) can be simplified to (in units of μg):

$$\mathrm{m_{CO_2}(cycle) = \int_{AST\ start\ time}^{time\ when\ CO_2\ returns\ to\ base\ level} 0.0051\left(ppm_{CO_2} - ppm_{CO_2,baseline}\right) dt} \qquad 3.18$$

$$\mathrm{m_{CO}(cycle)} = \int_{\text{AST start time}}^{\text{time when CO returns to base level}} 0.00324\left(\mathrm{ppm_{CO}} - \mathrm{ppm_{CO,baseline}}\right)\mathrm{dt} \qquad 3.19$$

From the mass of CO_2 and CO, mass of C lost can be calculated as:

$$\mathrm{m_{C_{lost}}(cycle)} = \frac{3}{11}\mathrm{m_{CO_2}(cycle)} + \frac{3}{7}\mathrm{m_{CO}(cycle)} \qquad 3.20$$

The results of equation (3.20) are discussed in chapter 3. Below in **Figure 3.11**, plotted are the ppm levels of CO_2 and CO (without the baseline corrections) as observed during the AST. **Figure 3.11 a** to **c** show the CO_2 ppm levels whereas **Figure 3.11 d** to **f** show CO ppm levels. The MEA II was aged for 500 cycles and MEA III was aged for 2000 cycles. So, the ppm data (for both CO and CO_2) for the first 500 cycles were averaged between these two MEAs. The ppm data for the next 1500 cycles is only from MEA III. As can be seen in the **Figure 3.11**, the CO ppm levels are much lower than the corresponding CO_2 levels. This is consistent as the potentials applied (1-1.5 V) are higher than the CO oxidation potential, as a result of which, most of the CO had been oxidized to CO_2.

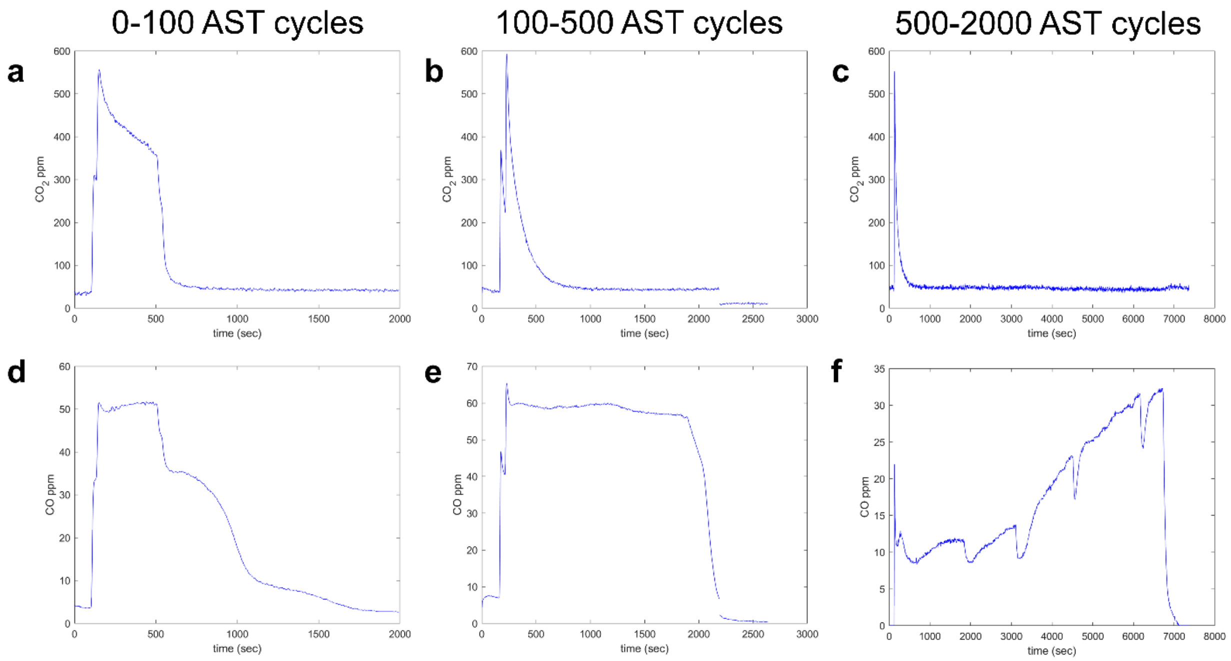

__Figure 3.11__ NDIR sensor data (in ppm) of CO_2 and CO during the AST voltage cycling.

3.6.4. Micro-X-ray diffraction

Synchrotron micro-X-ray diffraction (μ-XRD) mapping was conducted at Beamline 12.3.2 of the Advanced Light Source (ALS) at Lawrence Berkeley National Laboratory (LBNL). A 10 keV monochromatic X-ray beam was focused to ~2×5 μm^2 by Kirkpatrick−Baez mirrors. The degraded MEAs disassembled from testing hardware were mounted on a x−y scan stage and tilted 25° relative to the incident beam. Diffraction images were recorded in reflection mode with a two-dimensional Pilatus-1 M detector mounted at 60° to the incoming X-ray, approximately 150 mm away from the probe spot. Exposure time at each position was 10 s. Calibrations for distance, center channel position, and tilt of the detector were performed based on a powder pattern obtained from a reference Al_2O_3 particles taken at the same geometry. For mapping of the 1 cm ×1 cm area of each MEA samples (chapter 1) a scan of 50 × 20 points was performed with a step size of 200 μm on the x-axis and 500 µm on the y-axis. Finer 200 µm step size in x-axis was adopted to resolve the flow field channel (~0.78 mm) and land (~0.92 mm). The X-ray scan diffraction data was then processed by XMAS [52,53]. Diffraction rings were integrated along the azimuthal direction and the peak width was determined by fitting a 2D Lorentzian function with an angular resolution of~0.02°. Instrumental broadening was estimated using large Al_2O_3 crystals powder in the exact same detector configuration. The estimated Pt particle size is an average from both cathode and anode catalyst for each measured location since the synchrotron X-ray penetrates both cathode and anode. In our measurement, change of Pt particle size before and after AST is dominated by the cathode Pt catalyst particle size increase, as minimal particle size growth occurred on the anode side, when the anode was fixed at 0.0 V vs R.H.E in pure H_2 environment during AST. Please note that the step size in both x and y directions is different for maps in different chapters.

3.6.5. Micro-X-ray fluorescence

The micro-X-ray fluorescence (µ-XRF) measurements were performed using XGT-9000 Horiba XRF microscope. A 10 µm capillary was utilized to map an area of 2048 µm by 2048 µm near inlet and outlet with 1024 pixels in both x and y directions giving a resolution of 2 µm × 2 µm. The larger 20.48 mm × 20.48 mm (~ 4 cm^2) area was also mapped using the 10 µm capillary with 1024 pixels in both x and y directions giving a resolution of 20 µm × 20 µm. The X-ray energy was set to 50 keV. As the X-ray penetrates the full MEA (anode GDL, CCM and cathode GDL), the reflected X-ray signal to the detector includes Pt contribution from both anode and cathode. Thus, the quantified total average Pt loading is the sum of anode and cathode loading. 2D colormaps were generated in MATLAB using fluorescence images generated by the microscope and the quantified total average

Pt loading. The total average Pt loading of 550 μg.cm^{-2} with ± 2% spatial variation was quantified for the CCMs using a calibration curve generated from 10 μm capillary maps of calibration samples with known Pt loading. For Pt loading quantification L alpha peak was used. To ensure no variation is caused due to attenuation and the quantified data reflected true change, the total average Pt loading of each reported area was reconfirmed by using a larger 1.2 mm capillary at multiple spots (**Table 3.8** of chapter 4 results). A variation of only ± 2% was observed due to attenuation. No GDLs were removed from the CCMs after ASTs. The GDLs also made sure that the CCM was completely flat during mapping before and after ASTs. To make certain that observed in-plane movement of Pt loading was not due to distortion of the CCM when placed under vacuum, an equilibrium time of ~ 3 hours was provided before any mapping. Lastly, the inlet and outlet were marked on the cathode GDL for further after AST synchrotron experiments.

Table 3.8 *Quantified average total Pt loading with different capillaries to understand variation due to attenuation.*

	Average total Pt loading (Maps with 10 μm capillary) μg.cm^{-2}	Average total Pt loading (3 spots with 1.2 mm capillary) μg.cm^{-2}	% attenuation
Standard MEA 4 cm^2 – before AST	559	549	1.78
Standard MEA inlet – before AST	559	552	1.25
Standard MEA outlet – before AST	553	547	1.08
Standard MEA 4 cm^2 – after AST	550	541	1.63
Standard MEA inlet – after AST	551	559	1.45
Standard MEA inlet – after AST	548	549	0.18
Modified MEA 4 cm^2 – before AST	558	552	1.07

Modified MEA inlet – before AST	545	549	0.73
Modified MEA outlet – before AST	547	552	0.91
Modified MEA 4 cm^2 – after AST	498	487	2.20
Modified MEA inlet – after AST	477	470	1.46
Modified MEA outlet – after AST	535	543	1.30

The synchrotron X-ray micro fluorescence mapping (chapter 4) was carried out at the exact identical location using identical raster scan step of the diffraction mapping (start and end point, step size and scan area). The Vortex-EM detector is positioned at an angle to the incoming X-ray beam. The monochromatic X-ray energy was increased to 12 keV for X-ray fluorescence measurements.

To facilitate identical location μ-XRF mapping (chapter 4), a thin 25 μm PTFE template was prepared with alignment markers. Using the cathode flow field as reference, holes were cut out in the template near the inlet and outlet (**Figure 3.12**). The diameter of the holes was kept equal to the diagonal of the 2048 μm by 2048 μm area to be mapped. This ensured automatic alignment of the mapped areas when the template was placed (matching the alignment markers simultaneously) on the MEAs for mapping before and after the AST. Similarly, a PTFE template with square cut out of 4cm^2 area was prepared to facilitate identical location mapping of the larger areas.

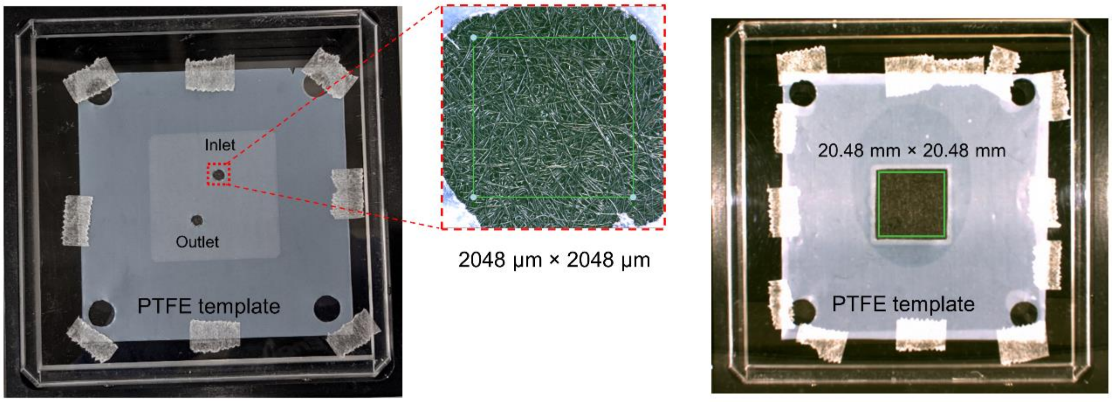

Figure 3.12 *Images show sample preparation with 25 μm PTFE template for 0.04 cm^2(L) and 4 cm^2(R) areas.*

3.6.6. Micro-X-ray computed tomography

Micro-X-ray computed tomography (μ-XCT) of MEAs and GDLs was performed at Beamline 8.3.2 at ALS synchrotron at LBNL, Berkeley, CA. Monochromatic X-rays with 25 keV energy were selected. 50 μm LuAg:Ce scintillator, 10x lenses and sCMOS PCO Edge camera were used to produce an image with 0.65 μm pix^{-1}. 200 ms exposure time was used with 1300 images collected per scan. To create the X-ray CT images, a three-dimensional image stack is reconstructed using two-dimensional radiographs collected from 0 to 180^o rotation. The reconstructions and phase retrieval were performed using the Gridrec algorithm with open-source TomoPy [54] The reconstruction parameters and details are described previously [55,56]. Image processing and 8-bit conversion were carried out with open-source Fiji/ImageJ [48] Dragonfly, Object Research Systems was used for 3D rendering.

3.6.7. Computational Fluid Dynamics simulation with Lattice Boltzmann Method

The Lattice Boltzmann Method (LBM) is a computational fluid dynamics (CFD) technique for solving a wide variety of fluid flow problems in the complex structure of the porous medium. LBM was performed to simulate the liquid water injection inside the detailed structure of GDL samples. The model utilized free surface conditions and a time-dependent simulation was used to capture the behavior of liquid water transport inside the GDL samples. XFlow 2020x (Build 102.03), which is a commercial CFD program that has a built-in LBM solver, was used to perform numerical simulations. The lattice element size was 0.65 µm, giving a total number of 18,312,548 to 22,353,320 elements, depending on the size and resolution of the computed geometry. The computational domain has a size of 400 x 400 μm^2 with the thickness depending on the sample. The time step was set to 0.1 µs. The liquid-water was injected under the sample at the same locations and flow rate at 1e-4 kg/s. The surface tension of liquid-water was set to 0.072 N/m, which corresponds to the surface tension of water in contact with air at 25 ºC. Surface tension is also responsible for the contact angle (θ) where a surface meets a GDL surface. This is determined by the interactions across the fluid-fluid and fluid-solid interface. The GDL contact angle in the simulation was assumed to be constant and uniform at 110 degree.

3.6.8. X-ray Photoelectron Spectroscopy

The X-ray photoelectron spectroscopy (XPS) data were measured by Kratos AXIS Supra X-ray photoelectron spectrometer, with a monochromatic Al Kα operating at 225 W for survey spectra and 300 W for high-resolution spectra. The survey spectra were acquired using 160 eV pass energy, 1 eV step size, 100 ms dwell time, while the high-resolution spectra were acquired using 20 eV pass energy, 0.1 eV step size, 100 ms dwell time. For each spectrum, the data were averaged by three random sample points and each sample point was averaged by specific cycles of scanning. All spectra were analyzed using CasaXPS software and fitted with 70 % Gaussian / 30 % Lorentzian line shape.

4. Results

4.1. *Chapter 1:* Mapping and probing heterogenous catalyst degradation under realistic automotive operating conditions

Practically, in both small-scale single cell MEA evaluation and large-scale PEFC stack operation, CCMs are sandwiched between cathode/anode GDLs. And the entire five-layer assembly is placed between flow fields/bipolar plates, where the land sections press down the GDL under compression to maintain good electrical contact and gases flow mainly in the channels of the flow fields/bipolar plates. Depending on the flow field geometry and fluid dynamics at specific operating conditions, there may exist local variations in mass transport, heat transport, water transport, and current distribution over the area of the catalyst layer, where local water accumulation, strongly influenced by the flow field geometry, plays an important role affecting catalyst durability [8,29,57]. Pt catalyst nanoparticles at specific locations are exposed to different local conditions (e.g., RH, liquid water content, and gas composition [H_2 and O_2 gradients in the case of H_2/air operation]), thus the localized degradation behavior likely deviates [58]. So far, 1D segmented cell design has shown some progress in delivering insights into electrocatalyst degradation from start-up and shut-down cycles, showing non-uniform ECSA loss between inlet and outlet regions [59]. But current understanding of this heterogeneity is still limited due to experimental limitation in resolving local degradation.

Particularly, how the heterogeneity of catalyst degradation correlates to its specific location does is quantitatively unknown. Thus, there is a need for detailed analytics of the Pt catalyst degradation with a fine 2D spatial resolution to elucidate such non-uniform Pt degradation behavior at the electrode level. In this chapter, a new methodology to spatially resolve and quantify Pt catalyst nanoparticle degradation over a large area (several cm^2) of aged MEAs was developed. The novel method was used to understand in detail the causes of heterogeneous Pt catalyst degradation rates by comparing ASTs in H_2/N_2 and H_2/air environments under wet and dry operating conditions.

4.1.1. Electrochemical characterization data

Figure 4.1 a-d shows polarization curves for four MEAs during the AST. Over the course of 30,000 cycles (~ 50 hours) all four MEAs showed potential loss that indicates that degradation is taking place. Comparing the polarization curves for BOL and EOL for four MEAs a clear trend emerges, where higher potential loss at medium and high current densities is observed for MEAs cycled in N_2 compared to those in air. Over the course of 30,000 AST cycles, N_2 Wet MEA had the largest polarization loss, which amounted to 0.2 V at 0.8 A/cm^2. For all four MEAs the polarization curves at the BOL and after 1,000 cycles either showed minimal difference (N_2 Wet), showed improved performance after 1,000 cycles (Air Dry) or did not show any differences (N_2 Dry and Air Wet). 1,000 AST cycles translates to 1.67 hours of testing. The minimal improvement or no change of polarization during this 1.67 hours can be attributed to additional cell conditioning. Previous study has shown that for Pt/C (low surface area) the mass activity improves during first three voltage recovery cycles [60]. For the Air Dry MEA OCP of 0.95 V was observed at the BOL which decreased to, 0.94 V, 0.93 V at 15,000 and 30,000 cycles respectively. The OCV reported here is collected after voltage recovery. But during the AST cycling in air environment, it was observed that the OCV (UPL for Air ASTs) decreased to 0.83 V (**Figure 3.3**), which is lower than 0.95 V UPL used for N_2 ASTs. The OCV decrease during the voltage cycling caused the AST to be performed at lower values of UPL, which reduced the amount of Pt being dissolved. This lower rate of degradation is due to decreased amount of PtO formed at lower UPL [33,35,61]. The potential loss during AST for all four MEAs from 1,000 to 5,000 cycles, from 5,000 to 15,000 cycles and from 15,000 to 30,000 cycles can be approximated as equipotential within the MEA but different between MEAs. Correlation between the polarization loss and the ECSA loss is discussed in the upcoming sections.

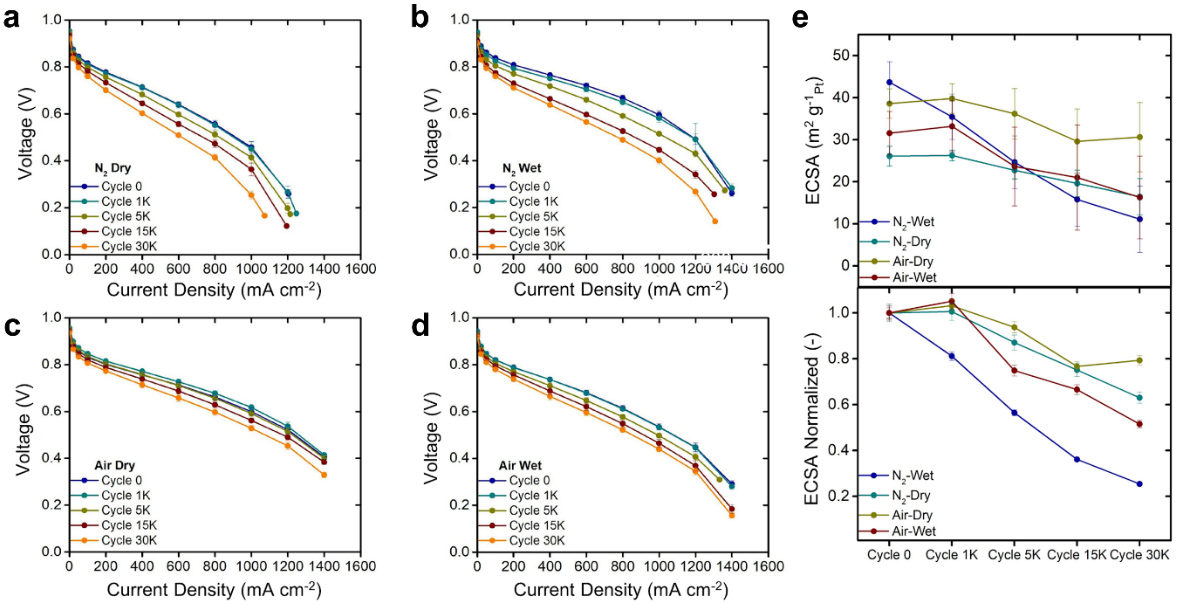

__Figure 4.1__ Polarization curves collected after 0, 1000, 5000, 15000 and 30000 AST cycles for a, N_2 Dry, b, N_2 Wet, c, Air Dry and d, Air Wet. The polarization curves were carried in H_2/Air at 80ºC, 100 % RH, 150kPa(a) backpressure, 1.5/1.8 stoichiometry anode/cathode. e, ECSA as a function of AST cycle number for N_2 Dry, N_2 Wet, Air Dry and Air Wet MEAs (top). Normalized ECSA as a function of AST cycle number (bottom).

Figure 4.2 shows cyclic voltammetry curves for four MEAs from the BOL to 30,000 cycles. The ECSA for each experiment was calculated from the charge integrated under the H_{UPD}

region with equation (3.1). For all MEAs with ageing the following observations were made regarding the CVs: i) the loss of the H_{UPD} region, ii) the loss of adsorbed oxide species on Pt surface and iii) an increase in double layer capacitive current between 0.5 and 0.65 V. The most pronounced reduction in H_{UPD} region was observed for N_2 Wet and N_2 Dry, where, together with the decrease in ECSA, a reorganization in the Pt crystal structure was recognized, as almost complete disappearance of the peak in the region between 0.1 and 0.15 V was observed, generally associated with the Pt (110) direction [62]. Pt(110) has shown to be the most unstable surface in rotating disk experiments, hence it is not surprising that its loss is the most pronounced in this study [62]. **Figure 4.3** shows that hydrogen cross-over and shunt resistances have not changed significantly during the AST protocols and thus are not major contributors of the MEA degradation.

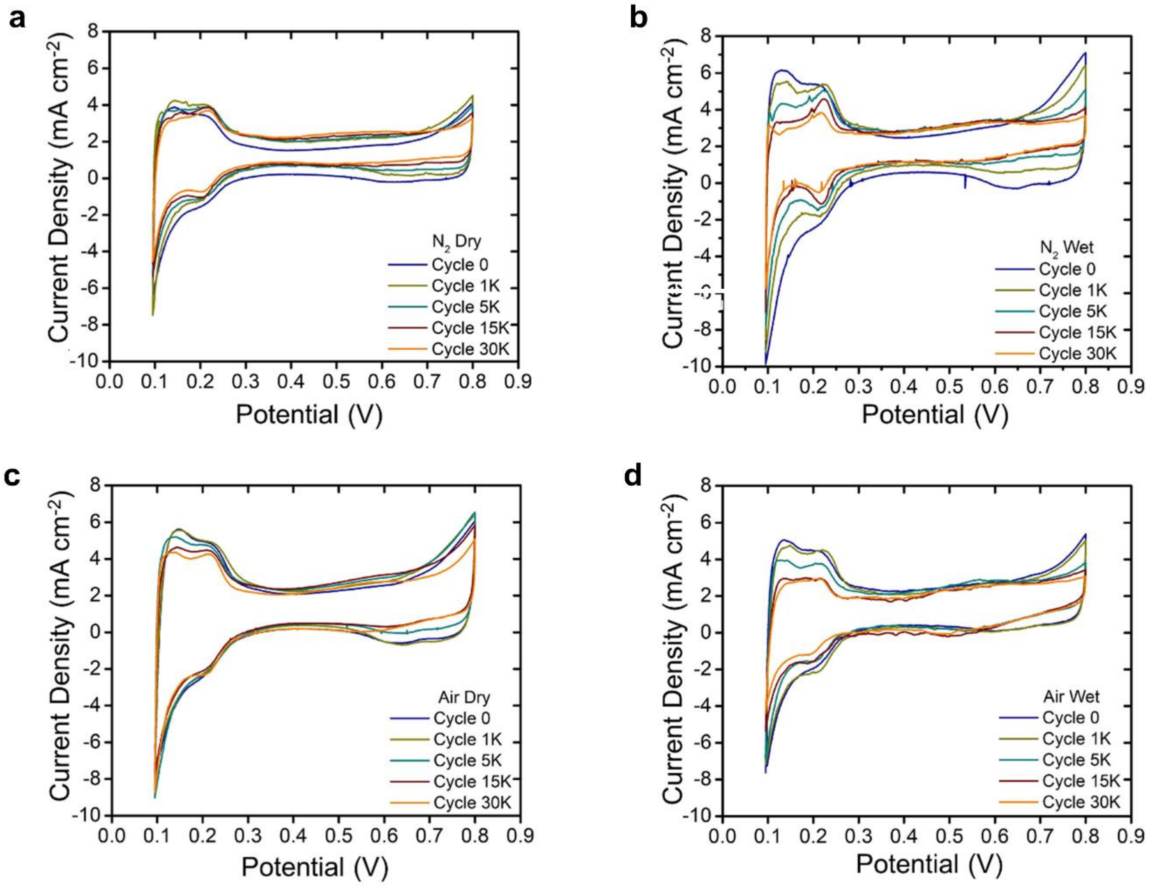

Figure 4.2 *Cyclic voltammograms collected after 0, 1000, 5000, 15000, 30000 AST cycles for a, N_2 Dry, b, N_2 Wet, c, Air Dry and d, Air Wet. The CVs were carried in H_2/N_2 at 80°C, 100 % RH, 200 sccm/300 sccm anode/cathode.*

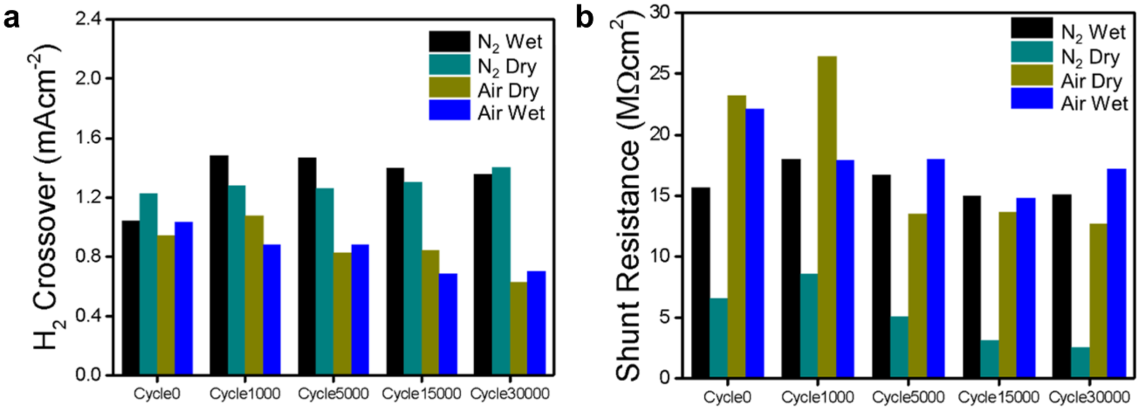

Figure 4.3 *a, Hydrogen crossover and b, shunt resistance calculated from LSVs collected after 0, 1000, 5000, 15000, 30000 AST cycles for N_2 Dry, N_2 Wet, Air Dry and Air Wet. The LSVs were carried in H_2/N_2 at 80°C, 100 % RH, 200 sccm/300 sccm anode/cathode.*

Figure 4.1 e shows the relationship of the calculated and normalized ECSA with the cycle number. Variation in the BOL ECSA is observed to be between 25 and 43 m^2 g^{-1}. N_2 Dry MEA has the lowest BOL ECSA, which will be attributed to MEA-to-MEA variability during fabrication process, which also resulted in thinner catalyst layer (**Table 4.2**). Lower BOL double layer capacitance also confirms this observation (**Figure 4.4**). There is a slight increase in the ECSA values at 1,000 cycles for the three MEAs but N_2 Wet, which can be attributed to additional cell conditioning as previously described. Such initial increase in the ECSA values has also been reported before [63]. A decrease in the ECSA is observed for all MEAs during AST cycling after 1,000 cycles. N_2 Wet MEA shows the highest catalyst degradation, from 43 m^2 g^{-1} at BOL to 10 m^2 g^{-1} after 30,000 cycles. This MEA also showed the highest loss of electrochemical double layer capacitance, which corroborates the ECSA loss. Compared to the other three MEAs, this MEA started out with the highest ECSA and ended up with the lowest. Only 25 % of the ECSA is left at the EOL. This can be attributed to the UPL that remains at 0.95 V constantly. As discussed in the Introduction section, ECSA loss scales with the UPL. Air Dry has the least ECSA loss, and it maintains 80 % of its ECSA at the EOL (from 38 m^2 g^{-1} at BOL to 32 m^2 g^{-1} at EOL). Whereas Air Wet and N_2 Dry show somewhat similar ECSA loss, maintaining 52 % and 62 % of the BOL ECSA and having 18 m^2 g^{-1} at the EOL. During ASTs in air environment, the UPL dropped to values below 0.9 V for both wet and dry conditions during voltage cycling. This lower UPL results in lower ECSA loss. Due to repeated oxidation and reduction of the Pt particles during AST cycling, Ostwald ripening and particle dissolution are the dominant degradation mechanisms that lead to the loss of ECSA through Pt particle size growth and Pt band formation in the- membrane.

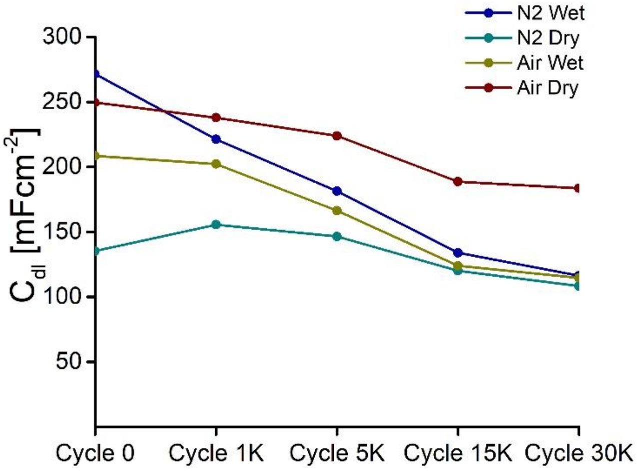

Figure 4.4 *Double layer capacitance for 0, 1000, 5000, 15,000, 30,000 AST cycles calculated from CVs for N_2 Dry, N_2 Wet, Air Dry and Air Wet. The CVs were carried in H_2/N_2 at 80°C, 100 % RH, 200 sccm/300 sccm anode/cathode.*

Table 4.1 *Tafel slopes extracted from ΔV vs. log($ECSA_{ratio}$) at low current density.*

Condition	Tafel slope at 100 mA cm^{-2} (mV decade^{-1}) from BOL to EOL, where the decade refers to log($ECSA_{ratio}$)
Air Dry	134
N_2 Dry	195
Air Wet	74
N_2 Wet	90

With the loss of ECSA, change in activation overpotential of ORR can be calculated by taking the ratio of two Tafel equations at BOL and that during ageing and rearranging to obtain the following:

$$\Delta\eta = \frac{2.303RT}{\alpha F} log(\frac{i_0 \cdot ECSA_{BOL}}{i_0 \cdot ECSA_{Aging}}) \qquad 4.1$$

where $\Delta\eta$ is the change in ORR overpotential from BOL to that during ageing, i_0 is exchange current density that is assumed to be constant [47], R is gas constant, T is temperature, F is Faraday's constant and α is the symmetry coefficient that is taken to be 1 at low current densities. Only ECSA changes during the ageing. When $\Delta\eta$ is plotted against log ($ECSA_{ratio}$), a Tafel slope can be calculated and compared to the expected 70 mV decade^{-1} if all the overpotential losses during ageing are due to ECSA loss. Using equation (4.1), Tafel slopes are calculated at a low current density of 100 mA cm^{-2} and plotted in **Figure 4.5** and summarized in **Table 4.1**, Tafel slopes of 90, 134 and 74 mV decade^{-1} for N_2 Wet, Air Dry and Air Wet MEAs were observed, respectively. Thus, N_2 Wet and Air Wet show close to expected 70 mV decade^{-1} loss of overpotential, which is indicative that the polarization loss for these two cases is mainly due to the ECSA loss. For the Air Dry the high Tafel slope value of 134 mV decade^{-1} was observed, which is indicative that the polarization loss is not only due to ORR kinetics but might be affected by mass-transport or other phenomena. Overall, since the average electrode thickness was not changed during the AST cycling (**Table 4.2**), degradation of the catalyst support due to ageing is negligible.

Table 4.2 *Catalyst layer thickness of the four MEAs acquired with cross-sectional SEM for Control sample and aged samples.*

	Control	**Air Wet**	**N_2 Wet**	**Air Dry**	**N_2 Dry**
SEM-Average Thickness (μm)	8.13 ± 0.59	9.32 ± 0.27	8.76 ± 0.26	8.13 ± 0.48	7.45 ± 0.17

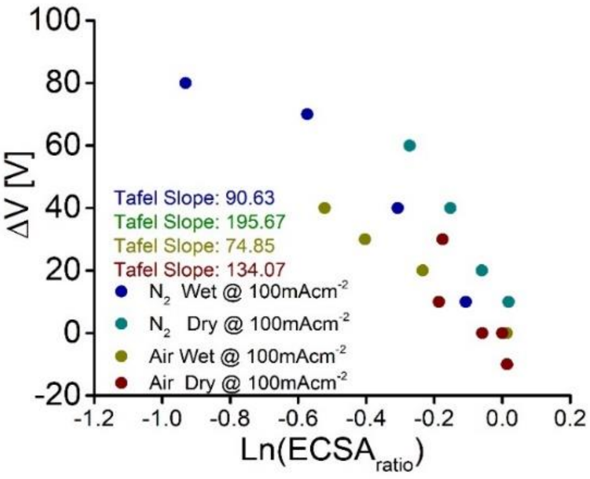

Figure 4.5 *Tafel slope analysis at low current density of 100 mA/cm^2. Tafel slopes were calculated from polarization curves carried in H_2/Air at 80^{o}C, 100 % RH, 150kPa(a) backpressure, 1.5/1.8 stoichiometry anode/cathode.*

4.1.2. Catalyst layer thickness and Pt band formation

Figure 4.6 shows the cross-sectional SEM images and EDS spectra for a Control sample and for the aged MEAs. The membrane is reinforced with ~15 µm layer of PTFE in the middle. The cathode catalyst layers are observed on the right and show uniformity in thickness. Pt-band formation is identified in case of N_2 Wet conditions close to the cathode catalyst layer and PEM interface where Pt ions were reduced by crossover H_2 and deposited inside the PEM (**Figure 4.6 f**). The large loss of ECSA for N_2 Wet conditions can be ascribed to this complete loss of Pt from the cathode catalyst layer. Pt band formation in other MEAs was not sufficiently pronounced to be observed by SEM. The cathode catalyst layer thickness values are shown by **Figure 4.6 g**, where thickness ranged from 8.13 to 9.32 µm for three MEAs but N_2 Dry, which had a lower thickness of 7.45 µm. Furthermore, the two thicknesses from XCT for Baseline and for Air Wet are also reported in **Figure 4.6 g**.

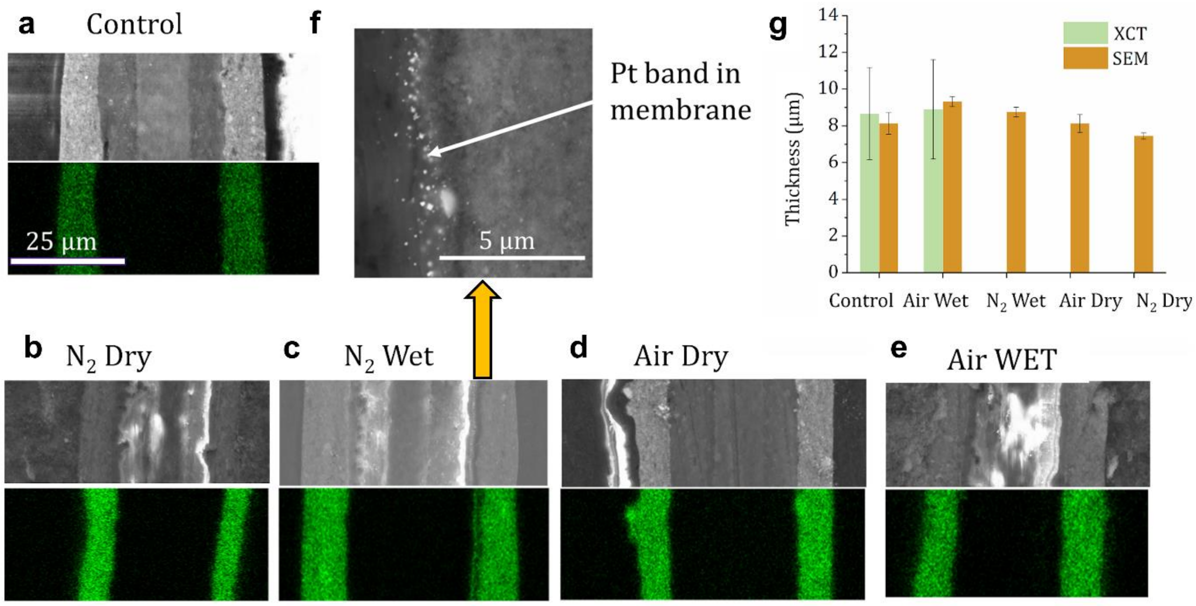

***Figure 4.6** (a-e top) Cross-sectional SEM images of the anode (left), PEM and cathode (right) catalyst layers and their respective EDS images, f, SEM image of the Pt-band formed within PEM for N_2 Wet AST and g, the bar plot of the average thicknesses acquired from SEM and XCT.*

4.1.3. Pt nanoparticle size growth

µ-XRD experiments were performed on the MEAs and 1 cm × 1 cm maps of the catalyst layer at the inlet, outlet and middle regions are shown in **Figure 4.7**. The Control sample has uniform particle-size distribution of average 3.2 nm. These particle sizes are consistent with previously reported value of 2.9 and 3.0 nm with local TEM methods [64,65], and to the 3.3 nm estimated by XRD [66] (for TKK TEC10E50E catalyst. Under dry conditions (**Figure 4.7 b** and **c**) the particle size growth is not significant compared to wet conditions (**Figure 4.7 d** and **e**). For Air Dry, there is no observable particle size change compared to the Control sample. This is also the sample that maintained 80 % of its ECSA at the EOL. N_2 Dry shows some Pt particle size increase under land in the middle and near the gas outlet. Mean Pt particle size observed was 4.7 nm. From the

ECSA plots N_2 Dry maintained 62 % of its ECSA at the EOL. Thus, the loss of 38 % of ECSA can be attributed to Ostwald ripening of particles from 3.2 nm to 4.7 nm via Pt dissolution. Air Wet and N_2 Wet showed the highest Pt particle size growth under land. Particularly, for Air Wet, such growth was notable at the outlet. Maximum Pt particle size observed for N_2 Wet was 14 nm, which is 4.5 times higher than the Control sample. For N_2 Wet, the difference in particle size between land and channel is significant only in the outlet region. The particle size under the channel decreased from inlet to outlet. Non-uniform humidification (inlet is more humidified compared to outlet owing to co-flow configuration and lack of produced heat and water due to absence of the ORR) is believed to be the cause for this heterogeneous particle size growth. Air Wet and N_2 Wet at EOL maintained 50 % and 25 % of the BOL ECSA, respectively. Air Wet had more significant change in Pt particle sizes than N_2 Wet from inlet to outlet, with prominent land to channel differences evident in all three regions. These significant changes in Air Wet are attributed to produced water mostly at the LPL (0.6 V) and subsequent heat generated due to ORR during voltage cycling. Differences in oxygen transport under land and channel lead to differences in ORR current (lower current under the land [67]. Therefore, catalyst layer located under the land is colder compared to the channel, as catalyst layer under the land generates less heat (due to lower ORR current). In addition, land conducts heat more effectively due to direct contact with the GDL fibers [68]. All this contributes to higher water content in the catalyst layer under land, which leads to increased PtO coverage and subsequent Pt dissolution, hence larger particle size under the land. Similarly, higher ORR current and therefore more heat is generated in the inlet region compared to outlet due to co-flow configuration of both anode and cathode gas feeds. As a result, outlet will be at a lower temperature than inlet and more humidified, which causes water accumulation in the outlet region [68,69] (more under lands). This leads to higher growth of Pt nanoparticle size in outlet region compared to inlet for air case. Previous neutron imaging studies have shown such water accumulation in air environment at the outlet [69,70]. Such inlet/outlet catalyst degradation changes in air and N_2 were observed previously [70,71] but not directly with μ-XRD.

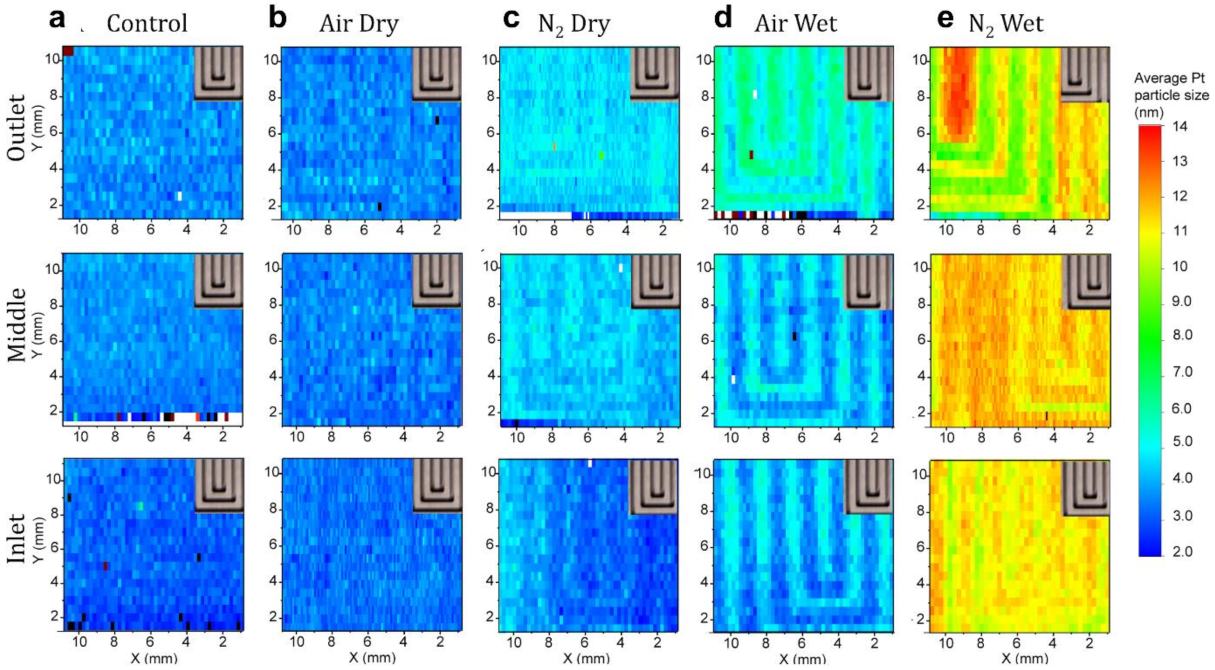

Figure 4.7 1 cm × 1cm μ-XRD maps showing post-mortem Pt nanoparticle size distribution in three locations (outlet, middle and inlet) of the MEAs a, control, post-mortem with b, air in dry condition. c, N_2 in dry condition, d, air in wet condition and e, N_2 in wet condition. Insets show corresponding flow field geometry.

These observations are valid for relatively wide lands of 0.92 mm and one option is to design a flow-field with narrower lands. A 14-channel serpentine flow field with 0.5 mm x 0.5 mm width of land-channel (**Figure 4.8 e**) was used to perform N_2 Wet AST and understand whether similar heterogeneous Pt degradation is observed. This flow-field also has a larger pressure drop from inlet to outlet and water will be pushed from under the lands with gas crossflow, resulting in more uniform water distribution between land and channel. **Figure 4.8 a** to **d** shows the Pt nanoparticle size distribution maps and associated averaged distributions, where average particle size decreased from 9.3 to 6.7 nm from the inlet to outlet. These are much smaller sizes compared to the Pt particle size observed for 0.92 mm lands. From the 2D micro XRD map no clear land-channel geometry was observed and unimodal Pt nanoparticle size distribution was seen. The flow-field design has a significant impact on catalyst layer degradation due to water and heat management and choosing narrow lands can minimize heterogeneous degradation of Pt catalyst.

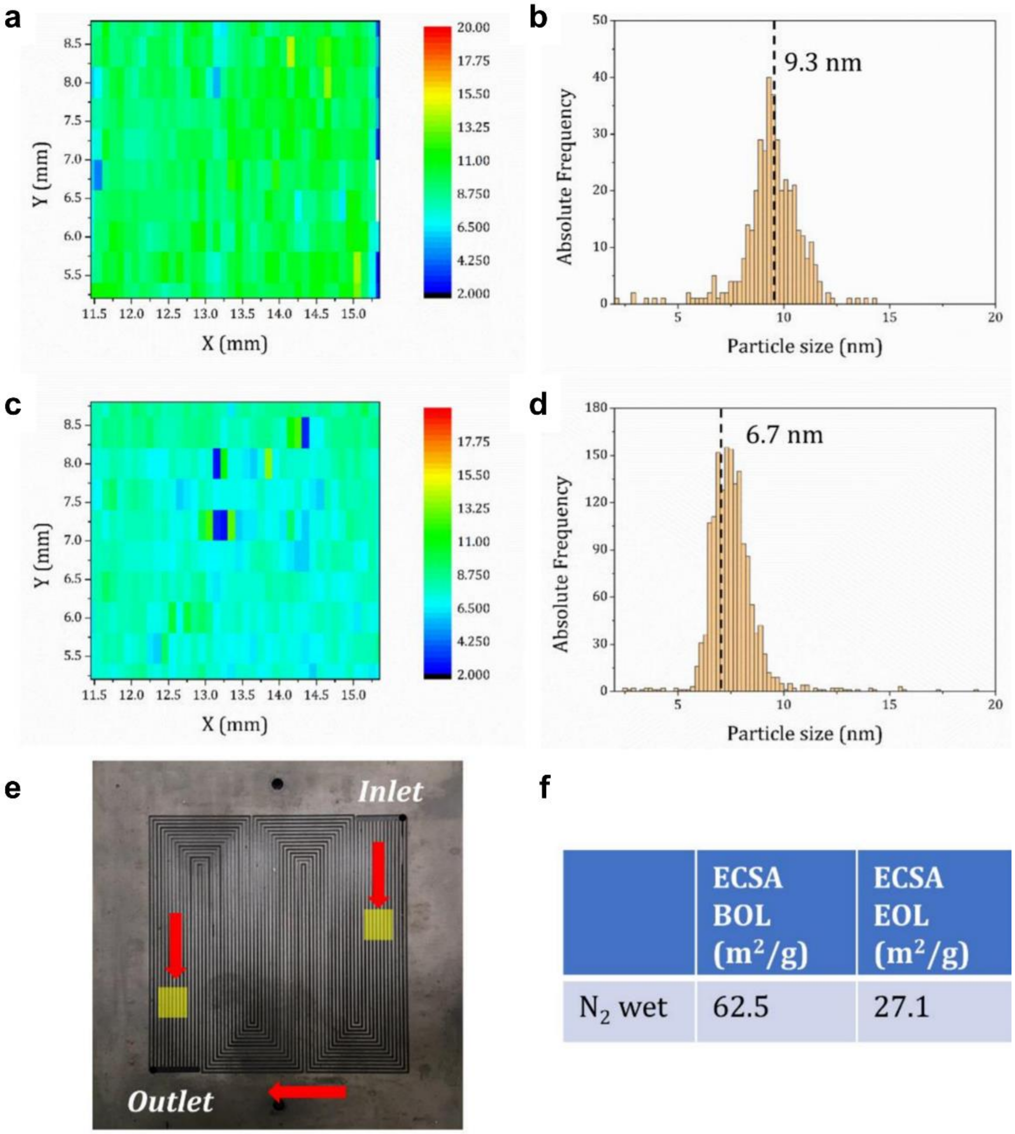

	ECSA BOL (m^2/g)	ECSA EOL (m^2/g)
N_2 wet	62.5	27.1

Figure 4.8 *a, Inlet location μ-XRD map and b, corresponding nanoparticle size distribution histogram. c, Outlet location μ-XRD map and d, corresponding nanoparticle size distribution histogram. e, 50 cm^2 DOE flow field and f, BOL and EOL ECSA.*

The data from **Figure 4.8** is summarized into a particle size distribution plot, shown in **Figure 4.9**, for the gas inlet, middle, and outlet of the MEAs. The Control sample showed log-normal size distribution with mean particle sizes of 3 nm near inlet and increasing to 3.5 nm near the outlet. The inlet and outlet difference in Pt particle size is mainly due to conditioning procedure for the Control sample. For the Air Dry MEA, the mean particle size increased from 3.3 nm at the inlet to 3.6 nm at the outlet. For N_2 Dry the bi-modal Pt distribution is observed near the inlet with 3 nm and 4 nm mean Pt particle sizes, whereas for the outlet the mean increased to 4.6 nm.

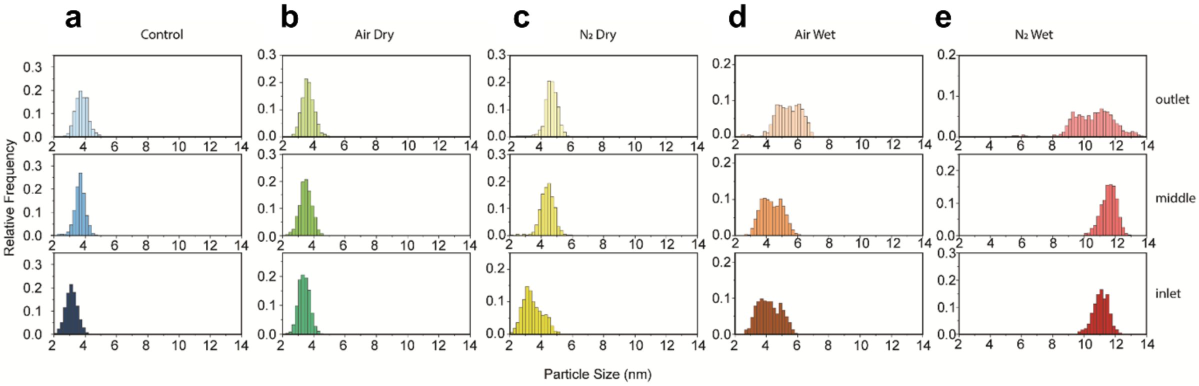

__Figure 4.9__ BOL and EOL catalyst particle size distribution in three locations (outlet, middle and inlet) for four AST MEAs.

From the data for Air Wet, bi-modal Pt size distribution is observed, with mean Pt particle size increasing from 4 nm near inlet to 5.5 nm near outlet. This increase of particle size towards the outlet in Air Wet conditions is due to water accumulation at the outlet [69,70], as water is generated during AST. Lastly, a single log-normal sharp distribution is observed near the inlet and in the middle of the MEA for N_2 Wet, with mean Pt particle size of 12 nm. The unimodal Pt distribution is because Pt distribution is more uniform under land and channel, as observed in **Figure 4.7**. But, near the outlet, bimodal distribution is observed again, due to smaller particle size under channel and larger particle size under land, with mean Pt particle sizes of 9.5 nm and 11.5 nm. Ostwald ripening is more pronounced for inhomogeneous particle size distribution, as smaller particles within nanometer distance to larger particles will dissolve and redeposit onto the larger particles. Here, it is important to emphasize that locally (under land or under channel) a unimodal distribution is observed and only when land and channel distributions are overlayed, they become bimodal.

4.1.4. X-ray photoelectron spectroscopy data

The XPS survey spectra results are shown in **Figure 4.10**, with the corresponding data listed in **Table 4.3**. It is found that the surface C/F atomic concentration ratios range from 1.17-1.08 for Control, 1.68-1.18 for N_2 Dry, 1.34-1.06 for N_2 Wet, 1.15-1.11 for Air Dry and 1.27-1.22 for Air Wet respectively (calculated by maximum C / minimum F and minimum C / maximum F), indicating that N_2 Dry and N_2 Wet have more ununiform ionomer exposure as F is the main content of Nafion®. Meanwhile, the average surface S/Pt atomic concentration ratios are found to be 1.78, 1.45, 1.28, 1.52 and 1.64 for Control, N_2 Dry, N_2 Wet, Air Dry and Air Wet separately (low atomic concentration elements don't have as accurate standard deviation as high ones), implying that both N_2 Dry and N_2 Wet MEA have worse ionomer coverage on Pt because sulfonate terminal groups of Nafion® are the proton conductive component and have high adsorption energy with Pt. These results are consistent with the phenomena in SEM and μ-XRD showing obvious Pt-band and larger particle size distribution of N_2 MEA than Air MEA, all revealing that numerous platinum nanoparticles detached from the ionomers.

Table 4.3 *The XPS survey results of five MEA. At% – atomic concentration. Std – standard deviation*

	O 1s		C 1s		F 1s		S 2p		Pt 4f	
Sample	At%	Std	At%	Std	At%	Std	At%	Std	At%	Std
Control	4.67	0.38	49.80	1.12	44.27	0.68	0.80	0.04	0.45	0.06
N2 Dry	3.65	1.29	55.76	5.16	39.61	3.42	0.58	0.26	0.40	0.20
N2 Wet	4.47	0.79	51.28	3.31	42.86	2.23	0.78	0.13	0.61	0.16

Air Dry	4.82	0.07	49.67	0.34	43.97	0.31	0.93	0.05	0.61	0.04
Air Wet	4.11	0.27	52.41	0.52	42.21	0.45	0.79	0.04	0.48	0.04

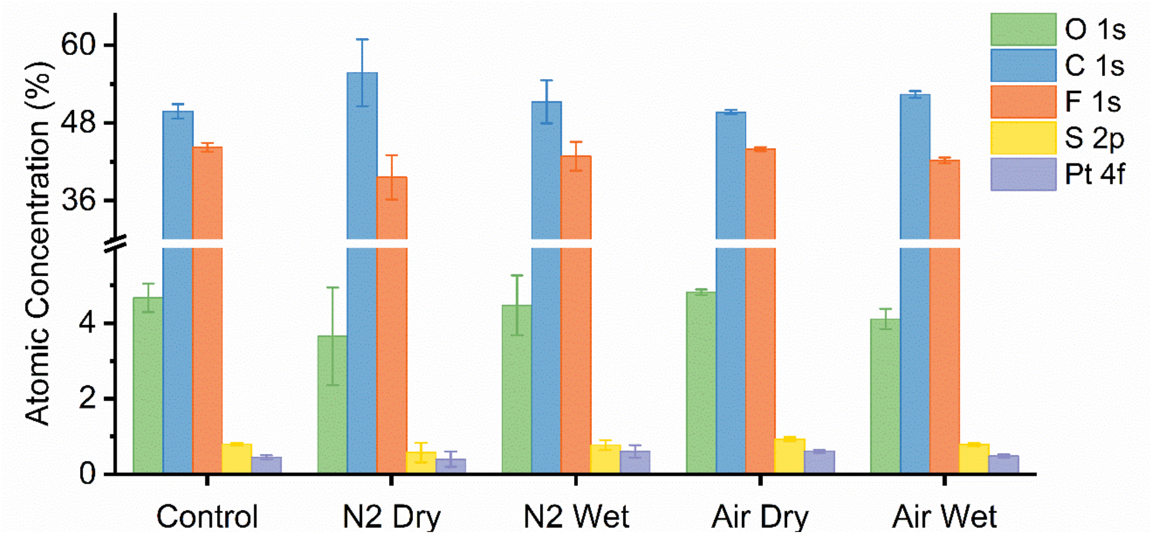

***Figure 4.10** The XPS survey results of five MEAs. The corresponding data are listed in Table 4.3.*

High-resolution C 1s and Pt 4f with curve fitting are shown in **Figure 4.11** and **Figure 4.12** respectively, with the corresponding results listed **Table 4.4**. The overlapping five MEA C 1s and Pt 4f after the normalization of maximum intensities to 1 are also given to compare the shapes, as **Figure 4.12** and **Figure 4.11 a**. It can be found that the relative atomic concentrations of sp^2 carbon (graphitic), which is the main chemical state of the carbon support but doesn't exist in ionomer structure, are ~32% for Control and Air Dry, about 36% for N_2 Wet and Air Wet, and as high as 41% for N_2 Dry. The high sp^2 concentration in N_2 Dry is consistent with the survey result that it has the most non-uniform ionomer exposure as described before.

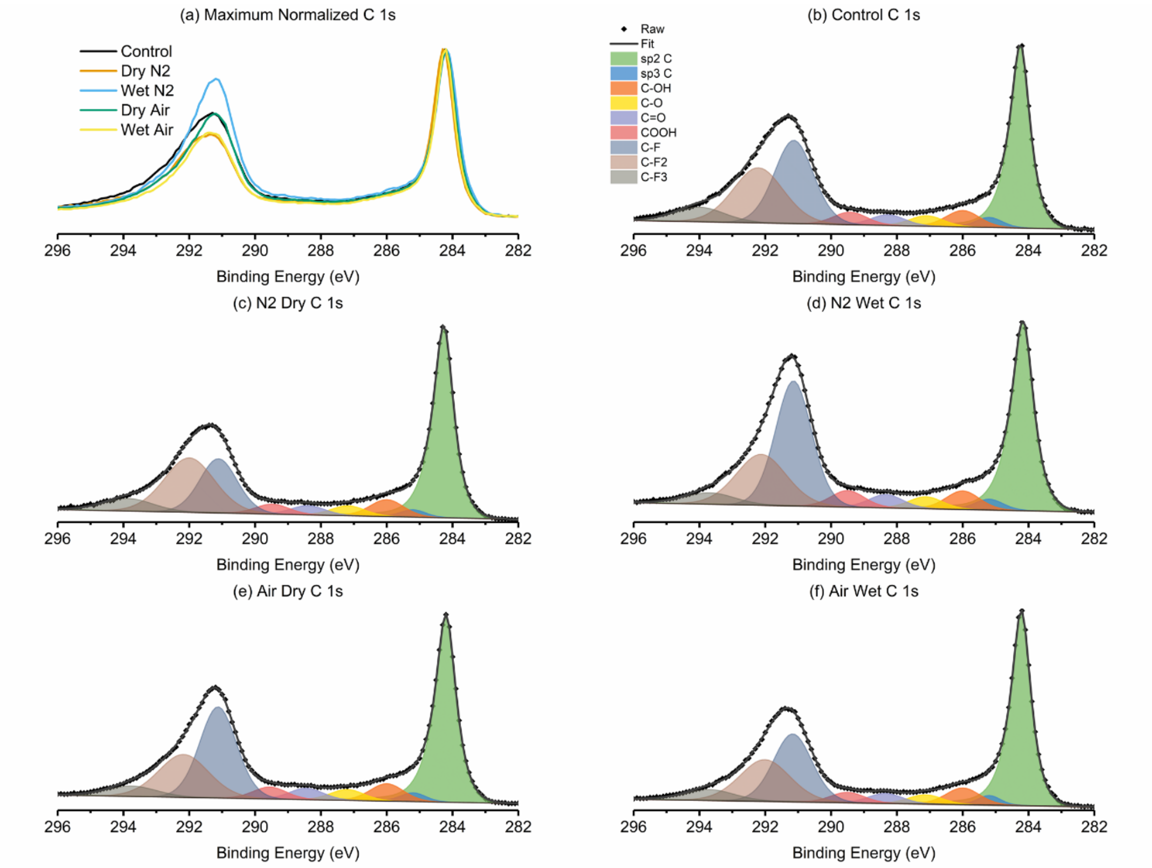

Figure 4.11 *Curve fitted high-resolution C 1s of five MEA: a, Overlapped spectra with the maximum intensities normalized to 1 (a.u.); b, Control; c, N_2 Dry; d, N_2 Wet; e, Air Dry; f, Air Wet.*

Table 4.4 *The curve fitted results for high resolution a, C 1s and b, Pt 4f of five MEA. At% – relative atomic concentration. Std – standard deviation.*

a	Control		N2 Dry		N2 Wet		Air Dry		Air Wet	
States	At%	Std	At%	Std	At%	Std	At%	Std	At%	Std
C 1 sp2	32.68	1.97	41.13	6.22	36.59	4.95	32.60	0.96	36.61	0.44
C 2 sp3	2.29	0.36	2.10	0.28	2.32	0.55	2.33	0.44	1.92	0.16
C 3 C-OH	4.35	0.23	5.25	0.73	4.72	0.68	4.23	0.21	4.85	0.02
C 4 C-O	2.73	0.09	2.90	0.09	2.71	0.12	2.88	0.03	2.78	0.15
C 5 C=O	2.74	0.05	2.79	0.26	2.76	0.19	2.96	0.14	2.82	0.04
C 6 COOH	3.02	0.33	2.60	0.64	3.12	0.48	3.29	0.11	3.09	0.10
C 7 C-F	22.28	3.04	17.07	7.94	22.08	5.82	24.67	1.76	21.91	2.43
C 8 C-F2	22.24	0.55	18.21	1.04	18.93	1.75	19.69	1.21	19.12	1.88
C 9 C-F3	7.66	0.67	7.94	2.39	6.78	1.50	7.34	1.02	6.89	0.41
b	Control		N2 Dry		N2 Wet		Air Dry		Air Wet	

States	At%	Std	At%	Std	At%	Std	At%	Std	At%	Std
Pt0	44.21	0.95	46.58	2.34	55.94	0.63	43.45	0.15	47.75	1.41
Pt2+	36.39	0.74	35.79	2.19	28.09	0.57	35.60	0.44	33.84	0.10
Pt4+	19.41	0.95	17.63	0.38	15.97	0.09	20.94	0.48	18.41	1.31

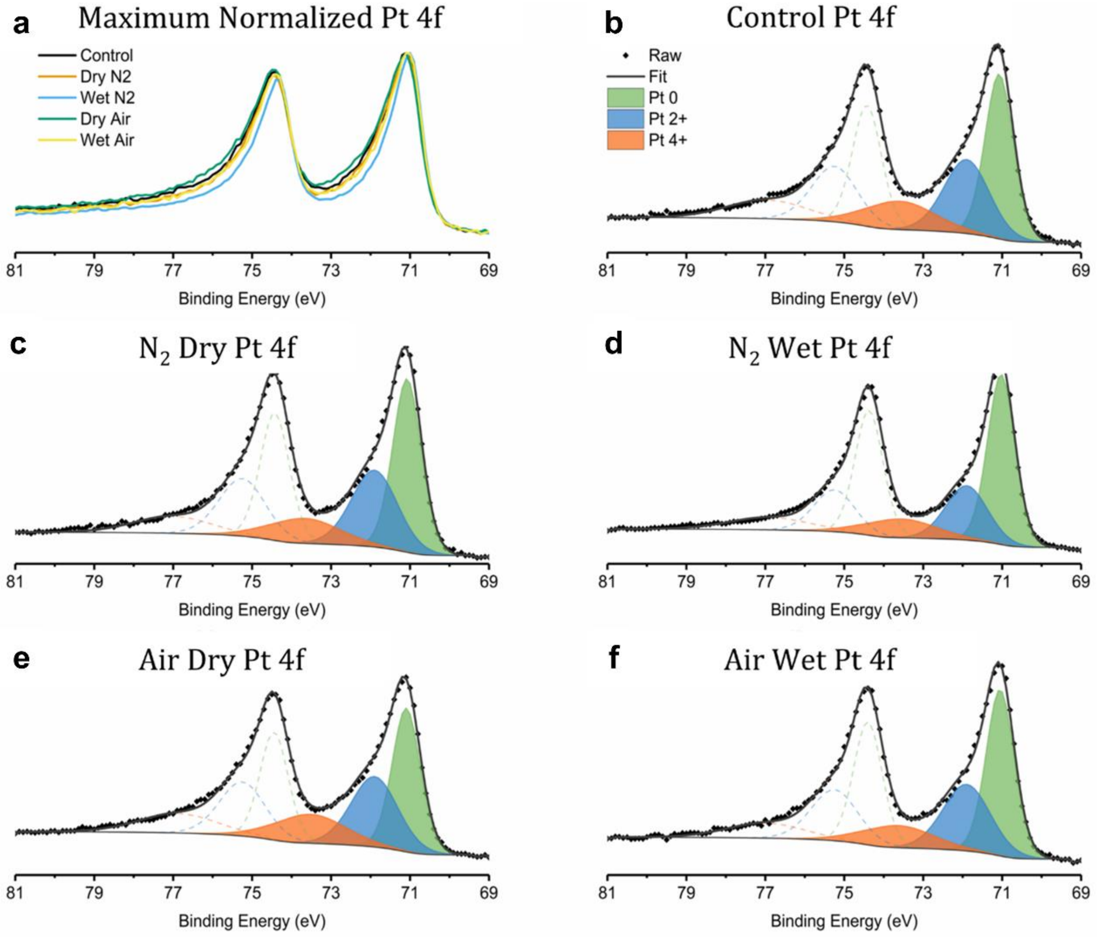

__Figure 4.12__ Curve fitted high-resolution Pt 4f of five MEA: a, Overlapped spectra with the maximum intensities of Pt 4f 7/2 normalized to 1 (a.u.); b, Control; c, N_2 Dry; d, N_2 Wet; e, Air Dry; f, Air Wet.

The high-resolution Pt 4f spectra in **Figure 4.12** reveals the surface composition of the platinum catalyst, comprised of reduced metallic platinum (Pt^0) and oxidized states of platinum: “surface oxidized platinum” (Pt^{2+}), usually associated with the presence of surface platinum oxide (PtO), and “edge oxidized platinum” (Pt^{4+}) usually associated with the PtO_2 represented at nanoscale by “edge oxide”. XPS observations suggest that N_2 Wet MEA sample has the highest relative Pt^0 atomic concentration ~56 % and Air Wet is the 2nd highest, of about 48 %, while the one of Control MEA sample shows only ~44 % (all concentrations are based on relative participation of the given moiety in the surface presence of the total chemical species). Higher content of metallic Pt^0 can be attributed to larger nanoparticle size. In such larger particles a substantial portion of platinum atoms would be located inside the nanoparticle and thus will not contribute to electrocatalytic activity. On the other hand, the relative atomic concentrations of “edge” Pt^{4+} are found to be 19.4 %, 17.4 %, 16.0 %, 20.9 %, and 18.4 % for Control, N_2 Dry, N_2 Wet, Air Dry and Air Wet, respectively. In contrast with Pt^0, larger Pt nanoparticle size leads to smaller surface area and hence lower edge Pt. In general, the high-resolution Pt 4f XPS spectra is consistent with the Pt size distributions observed by microscopy and estimated by XRD. XPS spectra corroborates also with the direct observations of “Pt band” formation and Pt nanoparticles clustering in cross-section SEM and micro-XRD described above, confirming that N_2 Wet sample MEA registers severe platinum dissolution and re-agglomeration.

Specific hypothesis on the Nafion® ionomer redistribution can be made from the analysis of the relative intensities change in component structure of the high-resolution C 1s spectra provided in **Figure 4.11 a** and **Table 4.4**. It should be noted that sp^2 carbon species (often termed “graphitic”) is the main chemical state of the (element) carbon in the carbonaceous support but is entirely absent in the chemical structure of Nafion® ionomer, were all the carbon is in sp^3 state. The relative atomic concentration of sp^2 carbon is ~32 % for Control and Air Dry, it elevates to about 36 % for N_2 Wet and Air Wet, and as high as 41 % for N_2 Dry MEA sample. The high sp^2 concentration in the N_2 Dry sample is consistent with the microscopy survey result indicating that it has the least uniform (most heterogeneous) ionomer distribution, concurrent with the observation of highest "exposed" carbonaceous support for that sample from XPS. Another interesting spectral XPS segment is the carbon-fluorine region ranging from 290-296 eV binding energy (the higher the BE is, the more F atoms are bonded with the C). Considering the Nafion® chemical structure one can conclude that C-F moiety is associated solely with the sulfonate group of the ionomer, C-F_2 is the main building block of the Nafion® polymer backbone and C-F_3 is the ionomer backbone terminal. Thus, the ratios between such moieties present in the spectra of MEA samples could indicate the levels of heterogeneity and interactivity of these components of the Nafion® chain. We can see that the ratio of C-F/C-F_2 are calculated to be 1.17-0.84 for Control, 1.46-0.47 for N_2 Dry, 1.62-0.79 for N_2 Wet, 1.43-1.10 for Air Dry and 1.41-0.93 for Air Wet. Higher ratio values for N_2 Dry and N_2 Wet imply that they have most heterogeneous sulfonate distributions, which is consistent with lower C/F ratios in survey spectra. The reason why N_2 Dry has the highest deviation in both C/F ratio (in the survey XPS spectra) and C-F/C-F_2 ratios (in the high-resolution C 1s spectra) is probably because the sulfonate ionomer group is hydrophilic and has less mobility at lower humidity adding a surface/chemical component to the explanation of the drying phenomena and associated with it structural changes at hierarchy of scales.

4.1.5. Morphology of catalyst layer and catalyst loading changes

Figure 4.13 shows the XCT volume rendered images of the Control MEA (**Figure 4.13 a**) and the MEA with AST cycling in Air Wet conditions (**Figure 4.13 b**). These images reveal the woven structure of the catalyst layer. After ageing some of the catalyst coated membrane is swollen into a crack in a microporous layer (**Figure 4.13 b**). As it is shown in **Table 4.2** the catalyst layer thickness remains approximately unchanged after the AST, the result was also confirmed via the XCT data, where through comparing **Figure 4.13 c** and **Figure 4.13 d** it is seen that the thickness of the catalyst layer remains unchanged after the AST. The inhomogeneity in catalyst layer thickness is mainly due to it having a pattern.

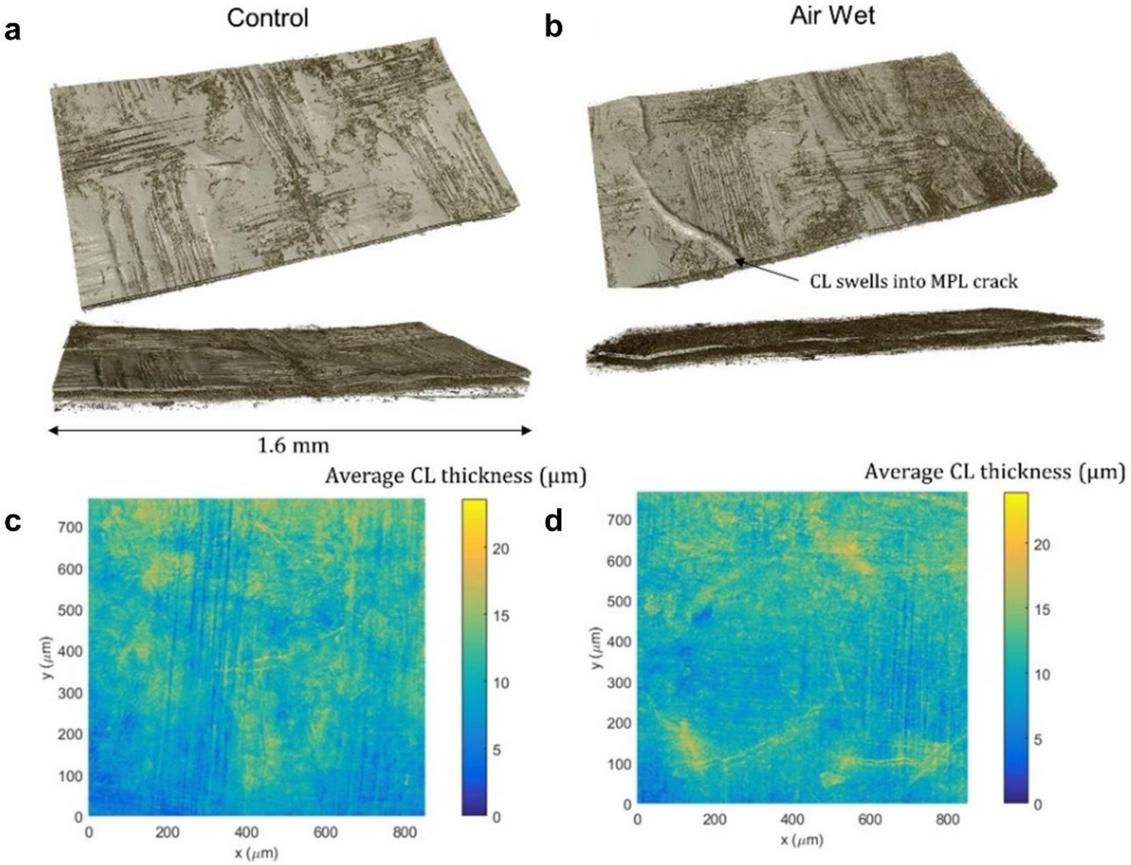

Figure 4.13 *XCT volume-rendering of a, control and b, Air Wet MEA. The average CL thickness is shown as a 2D map for c, control and d, Air Wet MEA.*

To understand whether Pt loading distribution is correlated to Pt nanoparticle size distribution, or whether Pt nanoparticle growth is a local phenomenon, μ-XRF mapping for N_2 Wet and Air Wet MEAs at the EOL was performed. N_2 Wet and Air Wet MEAs were selected because they showed the highest Pt nanoparticle size changes between the land and channel. **Figure 4.14 a** shows the 2 mm x 2 mm location mapped with micro XRF near the outlet. The micro XRF signal comes from both anode and cathode catalyst layers (control sample loading ~ 0.6 mg_{Pt} cm^{-2}). **Figure 4.14 b** shows the Pt loading distribution curves for the three MEAs. The average Pt loading decreased from 0.6 mg_{Pt} cm^{-2} to 0.5 mg_{Pt} cm^{-2} for both N_2 Wet and Air Wet MEAs, indicating a loss of 0.1 mg_{Pt} cm^{-2} of Pt from the cathode catalyst layer. Such loss of Pt loading can occur due to removal of effluent water containing Pt ions from the MEA. This Pt loading loss may be higher near the outlet due to water accumulation. Similar Pt loading loss was observed in previous studies, where Pt ions were detected in effluent water [57].

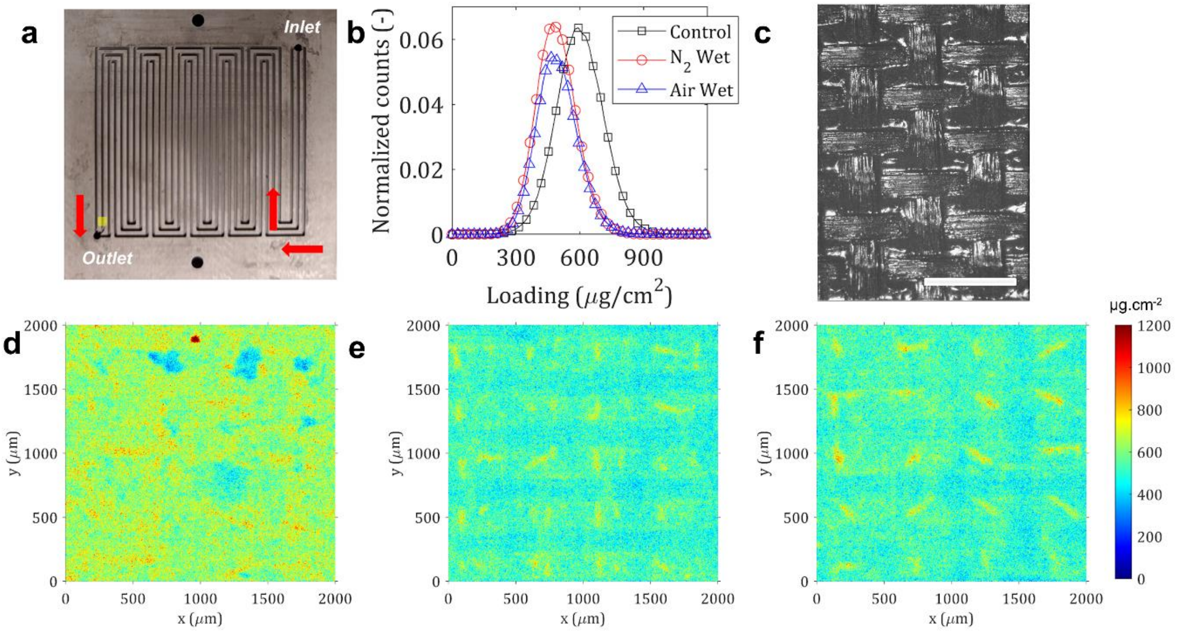

***Figure 4.14** a, Flow-field used in the fuel cell assembly with highlighted area (near outlet) where µ-XRF maps of the MEAs have been taken, b, the loading of Pt for the MEAs plotted via averaging µ-XRF maps, c, the optical image of cathode catalyst layer of pristine MEA d, control sample micro XRF map, e, N_2 Wet AST MEA micro XRF map and, e, Air Wet AST MEA micro XRF map. The size of the scale bar in c is 1 mm.*

No such Pt loading loss was observed for N_2 Dry AST sample as shown by **Figure 4.15**. µ-XRF also maps the patterned structure of the catalyst layer, where the optical image of catalyst layer is shown by **Figure 4.14 c**. Optical image clearly confirms that the structure of the catalyst layer is patterned with a thread pitch of 250 µm. **Figure 4.14 d** shows the control sample MEA µ-XRF map near the outlet. Local bare spots are observed that are primarily due to gaps in the catalyst layer pattern and some manufacturing defects. **Figure 4.14 e** and **Figure 4.14 f** show µ-XRF maps of N_2 Wet and Air Wet MEAs, where no loading redistribution was observed under the land or channel. This observation confirms that the Pt particle size growth under land is a local phenomenon.

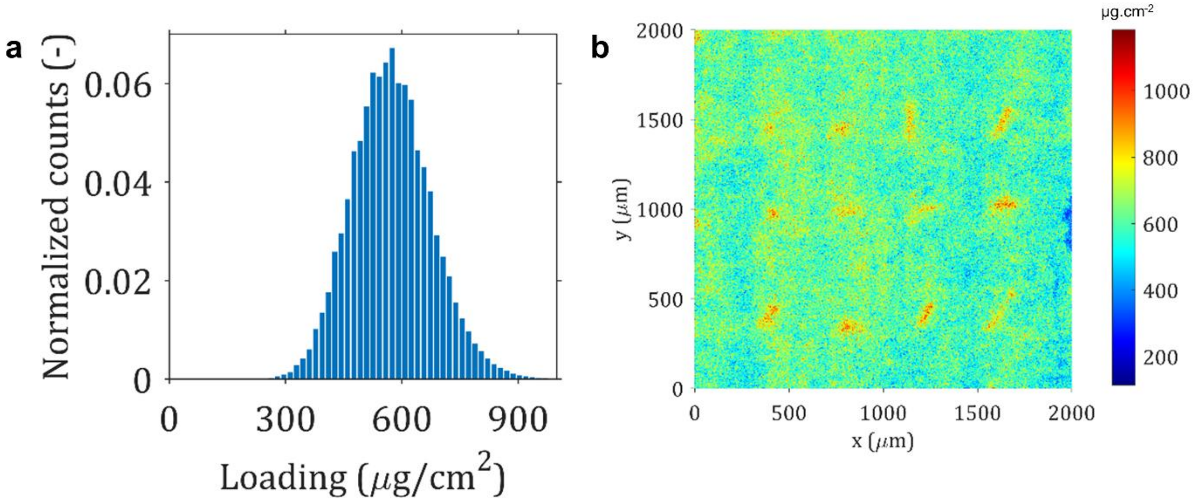

Figure 4.15 a, Nitrogen Dry AST sample average Pt loading and b, μ-XRF map of Nitrogen Dry AST sample.

Figure 4.16 summarizes the land and channel differences due to Pt dissolution during N_2 Wet and Air Wet ASTs. Under the land and in N_2 Wet AST Pt nanoparticle size increases mainly due to high mobility of Pt ions and high redeposition rates. Furthermore, observed Pt-band formation within the membrane is also due to high Pt ions mobility. For N_2 Wet AST under the channel lower Pt dissolution rates are expected because of less water present in the catalyst layer under the channel. For Air Wet AST smaller Pt nanoparticle size is observed under land compared to N_2 Wet AST which can be primarily attributed to the decreasing UPL, due to dropping OCV during voltage cycling. Fewer Pt^{2+} ions are observed due to lower amount of PtO formation at decreasing UPL. Also, under these AST conditions no Pt band formation was observed in the membrane. For Air Wet AST the Pt nanoparticle size under channel is smaller, as there is less water and lower UPL during cycling.

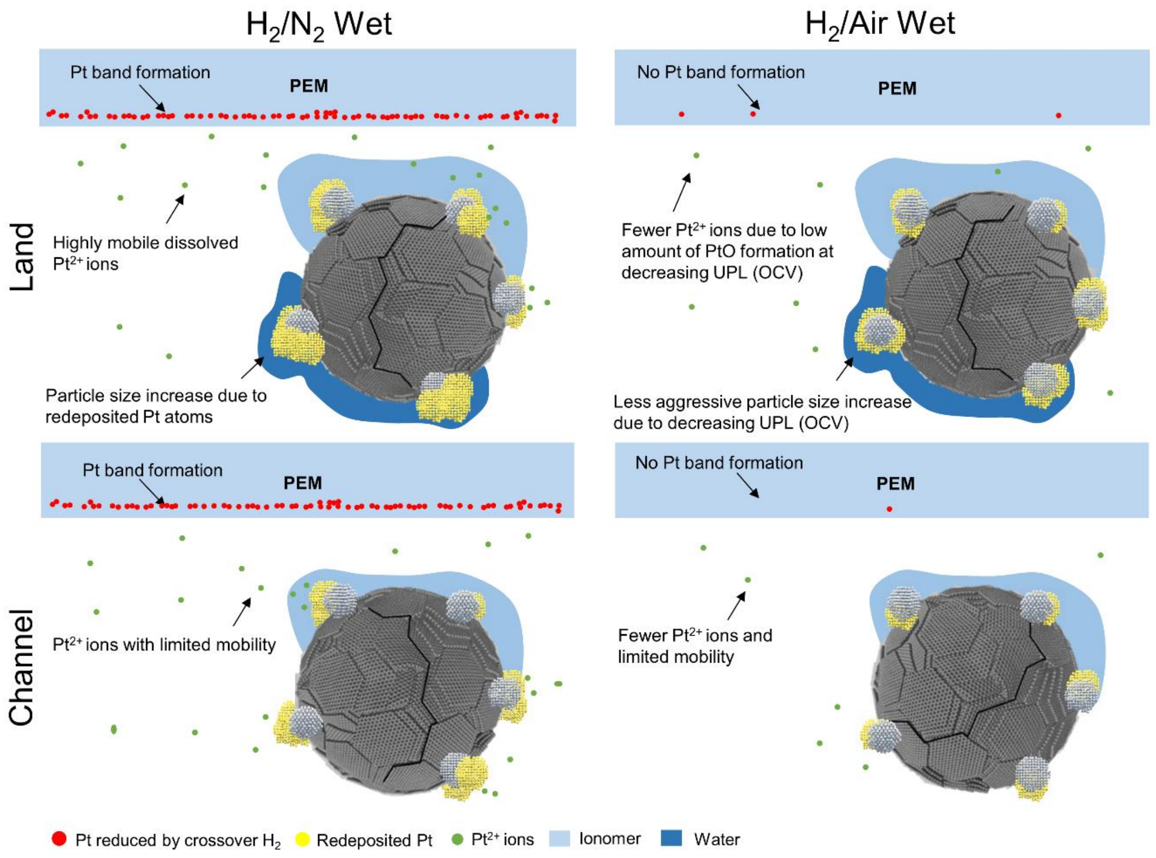

Figure 4.16 *A mechanistic summary of observed Pt degradation mechanisms in N_2 and Air Wet AST conditions.*

4.2. *Chapter 2:* Effect of gas diffusion layers on catalyst durability in varied cathode gas environment

In this study three widely used and commercially available GDLs were selected to elucidate their impact on cathode catalyst layer degradation. The selected GDLs were designed for high RH and high current density operating conditions. The MEAs were prepared using Sigracet 22BB (22BB), Freudenberg H23C6 (H23C6) and AvCarb MB30 (MB30) as cathode GDLs. All three MEAs were first tested in the nitrogen environment AST with fixed UPL. Following this, two GDLs were down selected to be tested in air environment AST to simulate actual PEFC operation. Advanced characterization techniques were used to spatially resolve Pt degradation between the three MEAs with different GDLs. In addition, computational fluid dynamic (CFD) simulations using Lattice Boltzmann method (LBM) were utilized to predict water distribution in the MEAs.

4.2.1. Morphology visualization and analysis of gas diffusion layers

X-ray CT was used to characterize morphological differences between the three GDLs studied. The cross-sectional tomograph of 22BB in **Figure 4.17 a** shows a relatively level MPL surface with a significant presence of cracks. The in-plane images show that cracks have approximately 10 - 20 μm width. The cracks penetrate the entire thickness of the MPL and potentially provide a low-resistance pathway for the transport of reactants and products to and from the cathode catalyst layer. It can also be noticed from both the cross sectional and the in-plane grayscale images that 22BB has a MPL which is embedded in the GDS. This embedding most likely happens when the MPL slurry is casted on the GDS, and the slurry flows into the substrate before drying completely. Lastly, the images show that the GDS was made of chopped carbon fibers held together by the carbonaceous binder. **Figure 4.17 d** shows the porosity of 22BB GDL, as a function of its thickness, which is about 209 μm. The MPL meso-porosities in this study were neglected and the only porosity measured was for the macroscale cracks. The cracks within MPL occupied about 20 % of the surface area, furthermore 22B showed the MPL to be embedded into 50 % of the GDS. As the embedded MPL disappeared, the porosity plateaued giving an average porosity value of 78 %. A broad and bimodal distribution of pore diameter in the GDS was observed, resulting in an average pore radius of 14.7 μm for 22BB. The bimodal distribution was fit with the probability density function (PDF) of log-normal bi-modal distribution, where the fitting parameters show two radii of distribution, 2.2 μm and 13.6 μm, as shown by **Table 4.5 a**.

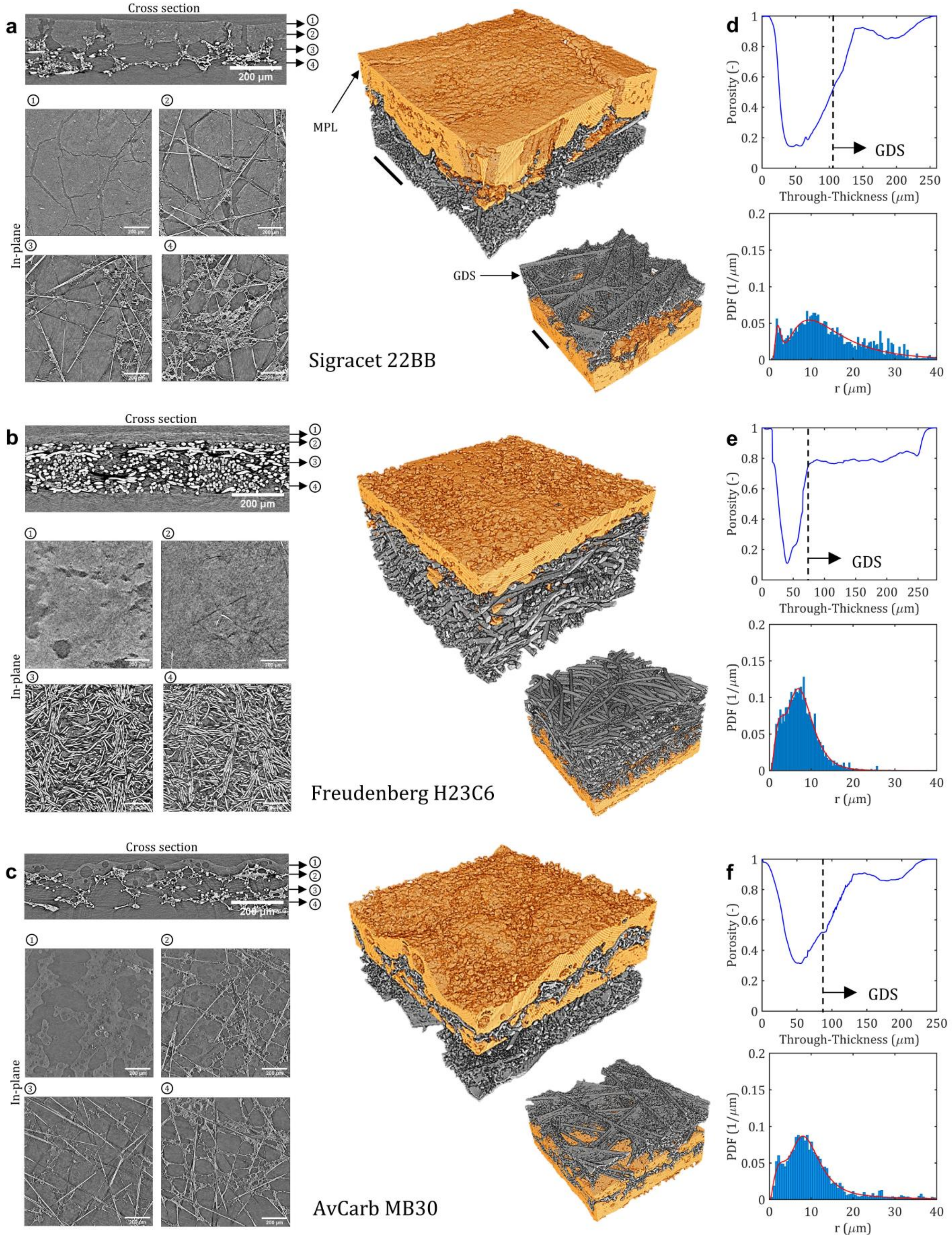

Figure 4.17 (Left) 2D grayscale cross-section tomographs (above) and in-plane tomographs (below). The GDLs studied are: a, 22BB b, H23C6 and c, MB30. (Center) 3D reconstructions with MPL and GDS view. (Right) d,e, and f, porosity

as a function of GDS thickness (above) and pore size distribution (below) for 22BB, H23C6 and MB30 respectively. Scale bars,100 μm.

Table 4.5 *Probability density function fitting parameters for a, Sigracet 22BB b, Freudenberg H23C6 and c, AvCarb MB30.*

a

Parameters	Radius (μm)
Mean	14.72
Mode	9.02
StdDev	8.86
R^2	0. 89
$f_{r,1}$	0.07
σ_1	0.33
σ_2	0.59
$r_{0,1}$	2.24
$r_{0,2}$	13.57

b

Parameters	Radius (μm)
Mean	7.65
Mode	8.23
StdDev	4.16
R^2	0. 98
$f_{r,1}$	0.43
σ_1	0.67
σ_2	0.34
$r_{0,1}$	4.41
$r_{0,2}$	8.39

c

Parameters	Radius (μm)
Mean	10.95
Mode	9.03
StdDev	8.18
R^2	0. 98
$f_{r,1}$	0.57
σ_1	0.91
σ_2	0.33
$r_{0,1}$	3.37
$r_{0,2}$	9.56

Tomographic images of H23C6 in **Figure 4.17 b** show a smooth and thin MPL that is not embedded over a GDS and is almost free-standing. The GDS is made of curled carbon fibers that are mechanically bound. This GDS does not have a carbonaceous binder. A sharp increase in the porosity followed by a plateau was observed for H23C6 in **Figure 4.17 e**, which is indicative of the distinct transition between MPL and GDS. The average porosity of H23C6 was found to be 80%. **Figure 4.17 e** also shows a narrow but bimodal pore radius distribution for the GDS of H23C6 highlighting its uniformity with an average pore radius of 7.6 μm. The PDF log-normal distribution fits show the radii of distribution are 4.4 μm and 8.4 μm, as reported by **Table 4.5 b**. **Figure 4.17 c** shows tomographic images of MB30, which reveal a highly uneven and undulating MPL surface with presence of large pores of approximately 5-10 μm. The voids within MPL make it highly porous. Like 22BB, MB30 also has an embedded MPL as seen in the in-plane images and 3D rendering. The GDS has fibers like 22BB but the carbonaceous binder used is highly porous. The pores in both the MPL and the binder suggest use of sacrificial material during the manufacturing to increase porosity. **Figure 4.17 f** shows that MPL is much more porous compared to 22BB and H23C6 with a linear increase in porosity near MPL|GDS transition, when plotted as a function of through thickness. This is indicative that the MPL is embedded in the GDS, which can also be observed visually. The average porosity of MB30 is 83%. **Figure 4.17 f** also reveals the somewhat narrow pore radius distribution of the MB30 GDS with an average pore radius of 10.9 µm. The in-plane tortuosity values were computed to be similar for three GDLs, as shown in **Table 1**. Bi-modal log-normal fits were generated with mean radii of 3.4 µm and 9.6 µm as shown by **Table 4.5 c**. The morphology of 22BB and MB30 are somewhat similar, with similar average radii, embedded MPLs, fibers of GDS being bound by a binder. H23C6 is significantly different with smaller average pores, free-standing MPL, curled carbon fibers and higher thickness. **Table 4.6** summarizes values of all the critical parameters of the three selected GDLs. **Figure 2.3** shows 3D reconstructed images of 1cm by 1 cm area highlighting key features of each GDL over a broader scale.

Table 4.6 *GDL properties for SGL 22BB, H23C6 and AvCarb MB30.*

Parameters	**Sigracet 22BB**	**Freudenberg H23C6**	**AvCarb MB30**	**Unit**
Total thickness	209 ± 9	226 ± 6	182 ± 7	µm
Micro Porous Layer Thickness	74 ± 7	35 ± 3	41 ± 9	µm
Porosity	78%	80 %	83%	-
In-plane tortuosity, $_{\text{in-plane}}$	1.21	1.26	1.31	-

Average pore radius, r_{ave}	14.7	7.6	10.9	µm

4.2.2. Electrochemical characterization data after N_2 AST

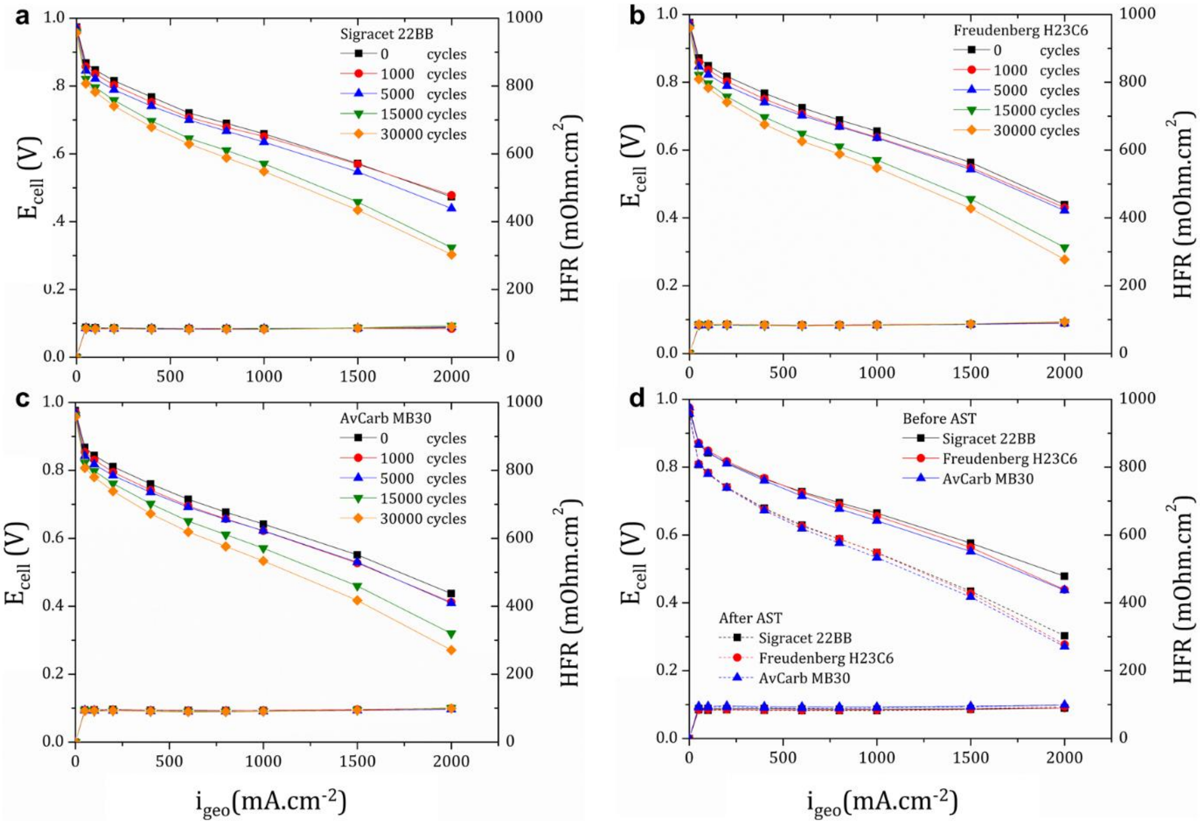

__Figure 4.18__ Polarization curves collected at BOL, 1000, 5000, 15000 and 30000 AST cycles in differential conditions at 80°C in 100% RH under 150 kPa (a) pressure. a, 22BB. b, H23C6. c, MB30 and d, before vs. after AST. The high-frequency resistance (HFR) is plotted on the right-side y-axis.

Polarization curves in differential conditions collected at 0, 1000, 5000, 15000 and 30000 N_2 AST cycles stage for each GDL MEA are shown in **Figure 4.18 a - c**. All the MEAs show significant voltage losses in the kinetic and mass transport regions of the polarization curves over the course of the AST. This loss in voltage for each GDL can be associated with coarsening of Pt nanoparticles resulting in the loss of ECSA. For all the MEAs, voltage loss within the first 5000 AST cycles is mostly kinetic and is dominated by decrease in the ECSA, since the slope of the polarization curve does not change. After 15000 cycles, a change of slope in the polarization curve is evident. No significant change in the high frequency resistance (HFR) suggests that this change in slope could be due to increase in the oxygen mass transport resistance or loss of ionic conductivity in the cathode catalyst layer, both of which will be discussed in the next section. A direct comparison of before and after AST polarization curves from the three MEAs were plotted in **Figure 4.18 d**. For each GDL MEA, identical cell voltages were recorded in the kinetic region at the BOL, which is expected as GDL should not impact kinetic region at low geometric current densities. Different GDLs can result in different HFR due to inadequate and uneven compression leading to differences in ohmic overpotentials. But care was taken in this study to achieve optimum GDL compression with lowest possible HFR value for each GDL. As a result, 22BB, H23C6 and MB30 all showed negligible differences in HFR, with values in the range of 85-95 mOhm.cm^2. This also eliminated any undesired catalyst degradation caused due to suboptimal settings and allowed a fair comparison of polarizations before, during and after AST. The effect of GDL emerges in the mass transport region. At the BOL, 22BB shows the lowest overpotential followed by H23C6 and MB30 at 1 A.cm^{-2}, 1.5 A.cm-^{2} and 2 A.cm-^{2}. This can be credited to the MPL cracks of 22BB, which facilitated better removal of produced water and prevented water accumulation in the cathode catalyst layer at high current densities. After AST, no significant difference was observed in the kinetic and ohmic regions of the polarization curves suggesting catalyst degradation led to identical ECSA loss for all three nitrogen environment ASTs. The improved overpotential in the mass transport region of 22BB carried throughout the N_2 AST, when compared to H23C6 and MB30. This also underlined the potential effectiveness of cracks as a strategy to improve MEA performance in the mass transport region.

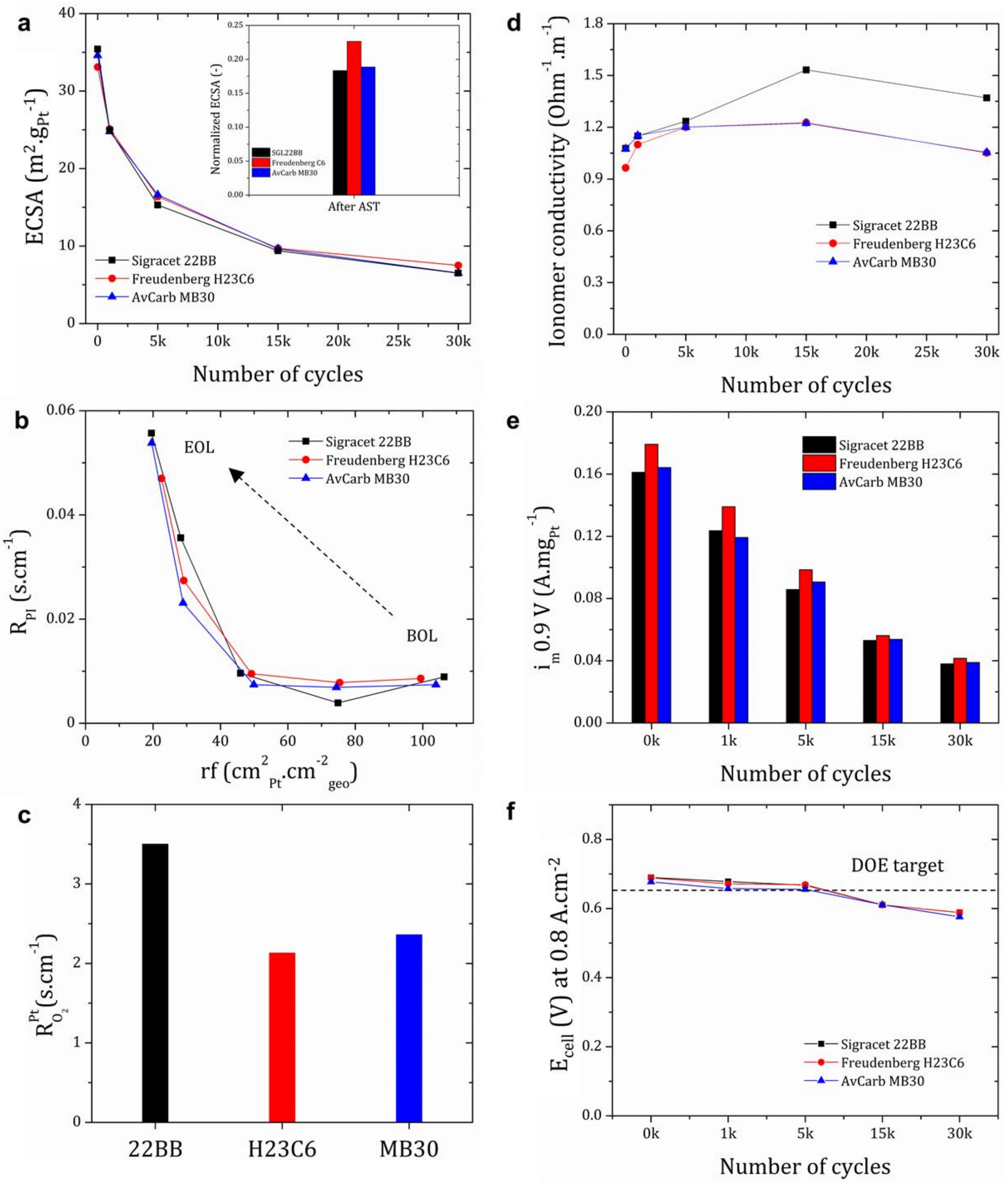

Figure 4.19 *a, ECSA loss as a function of number of AST cycles. b, Pressure independent oxygen mass transport resistance as a function of decreasing rf. c, Average oxygen mass transport resistance at the Pt-ionomer interface during nitrogen AST. d, Ionomer conductivity as a function of number of AST cycles. e, Mass activity calculated at 0.9 V from Tafel plots generated from polarization data collected in oxygen environment plotted as function of number of AST cycles. f, Voltage loss at 0.8 A.cm*$^{-2}$ *as a function of number of AST cycles.*

For MEAs with three different GDLs, the ECSA during nitrogen environment ASTs was plotted as a function of the number of AST cycles in **Figure 4.19 a**. The ECSA was calculated by integrating the hydrogen underpotential deposition region (0.1 V - 0.4 V) from CVs collected in hydrogen/nitrogen (anode/cathode) under atmospheric pressure (**Figure 4.20**). Before the nitrogen environment AST, 22BB, H23C6 and MB30 showed initial ECSA values of 35.42 $m^2.g^{-1}$, 33.1 $m^2.g^{-1}$ and 34.6 $m^2.g^{-1}$ respectively. Minimal differences observed in the initial ECSA values are from sample-to-sample variation. Approximately 50% of the initial ECSA value was lost by all the GDLs within the first 5000 cycles of the nitrogen environment AST (i.e., within 16% of the total AST duration). After AST, ECSA values for 22BB, H23C6 and MB30 were 6.50 $m^2.g^{-1}$, 7.50 $m^2.g^{-1}$ and 6.53 $m^2.g^{-1}$ respectively, resulting in a total loss of approximately 78% of the initial ECSA value for all the GDLs. No differences were observed in the ECSA loss trend between the three MEAs with different GDLs, although a very small difference can be noted in the after AST normalized ECSA plot (inset **Figure 4.19 a**) with 22BB and MB30 showing the lowest values. The ECSA loss corresponds well with the almost identical increase in kinetic overpotentials observed in the air polarization curves. The loss in the ECSA is dominated by increase in the Pt nanoparticle size due to electrochemical Ostwald ripening followed by Pt band formation near the membrane/cathode interface or via effluent water. **Figure 4.19 b** shows pressure independent oxygen mass transport resistance (R_{PI}) as a function of decreasing roughness factor (rf) as the AST progresses. After 5000 cycles apparent increase in the R_{PI} can be noticed as the rf decreases below the threshold of ~ 40. This apparent increase in the R_{PI} can lead to evolution of mass transport overpotentials at current densities as low as 0.5 $A.cm^{-2}$ and cause change in slope of the ohmic region as observed in air polarization curves of the three GDLs. Oxygen mass transport resistance at the Pt-ionomer interface (R^{Pt}_{O2}) after AST, given by the slope of total oxygen mass transport resistance (R_{Total}) vs rf^{-1} at different total pressures [41] (**Figure 4.21**) was averaged and is shown in **Figure 4.19 c** for all three GDLs. At 160 kPa, 22BB shows a value of ~ 3.5 $s.cm^{-1}$ while H23C6 and MB30 show values close to ~ 2.1 $s.cm^{-1}$ and 2.3 $s.cm^{-1}$, respectively. This means that a higher contribution from R^{Pt}_{O2} in R_{PI} is seen for 22BB suggesting either less contact between ionomer and the Pt catalyst due to particle size increase and/or decreased average Pt loading compared to H23C6 and MB30. Ionomer conductivity in the catalyst layer was plotted as a function of the number of AST cycles in **Figure 4.19 d.** The conductivity was calculated by fitting the EIS measured in hydrogen/nitrogen (anode/cathode) at 0.2 V (Nyquist plots in **Figure 4.22**). A small increase in the conductivity is noticed in the first 5000 cycles for all the GDLs. Therefore, ionic conductivity is not responsible for the slope increase in the polarization curves observed in **Figure 4.18**. Mass activity calculated from Tafel plots (**Figure 4.23**) is shown in **Figure 4.19 e**. All the GDLs showed a Tafel slope close to the theoretical value of ~70 $mV.dec^{-1}$. The trend of mass activity loss agrees well with the loss of ECSA. No significant change in the Tafel slope was observed before and after the nitrogen environment AST. An average of ~ 78% of initial mass activity was lost by all the GDLs after AST failing to achieve the DOE target of less than 40% loss of initial mass activity. Lastly, **Figure 4.19 f** shows voltage loss trend at 0.8 $A.cm^{-2}$ for each GDL over the course of the AST. There are identical voltage losses for all the GDLs at each stage of the AST with none of them meeting the DOE voltage loss target of less than 40 mV of the initial value. Approximately 100 mV of voltage loss was observed at 0.8 $A.cm^{-2}$ for each MEA. To summarize, the electrochemical characterization results show no difference in degradation of MEAs having 22BB, H23C6 and MB30 GDLs in nitrogen environment ASTs at 100% RH. This suggests that the Pt oxide coverage, which is the primary degradation stressor, remains unaffected by significant differences in GDL morphology at 100% RH in a non-reactive environment with absence of electrochemically produced water. This can be attributed to Kelvin effect, where the incoming water vapor will condense on the surface of Pt nanoparticles causing insignificant differences of Pt oxide coverage within the cathode catalyst layers having different GDLs.

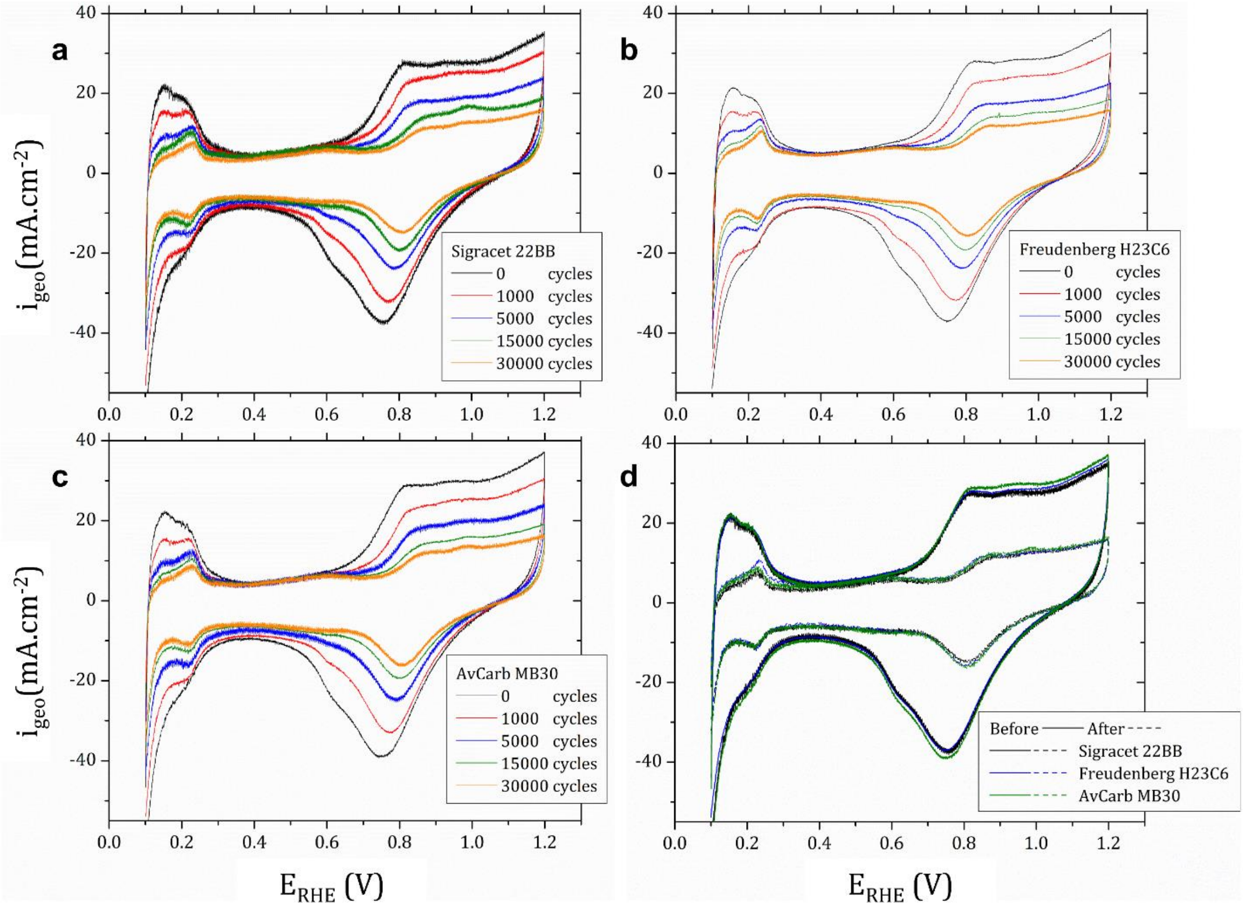

Figure 4.20 *Cyclic voltammograms collected in H_2/N_2 (anode/cathode) at 80°C in 100 % RH under atmospheric pressure at various stages of the AST for each GDL MEA. a, Sigracet 22BB b, Freudenberg H23C6 c, AvCarb MB30 and d, before and after AST.*

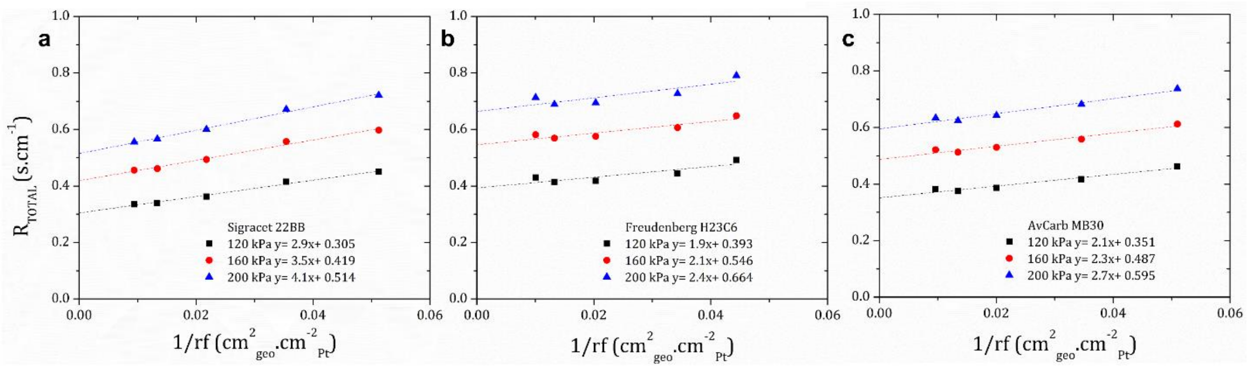

Figure 4.21 *Total oxygen mass transport resistance (calculated from limiting current experiments using 0.5 %, 1% and 1.5 % oxygen concentrations) plotted as a function of decreasing roughness factor over the course of AST for 120 kPa, 160 kPa and 200 kPa of absolute pressure. a, Sigracet 22BB b, Freudenberg H23C6 and c, AvCarb MB30.*

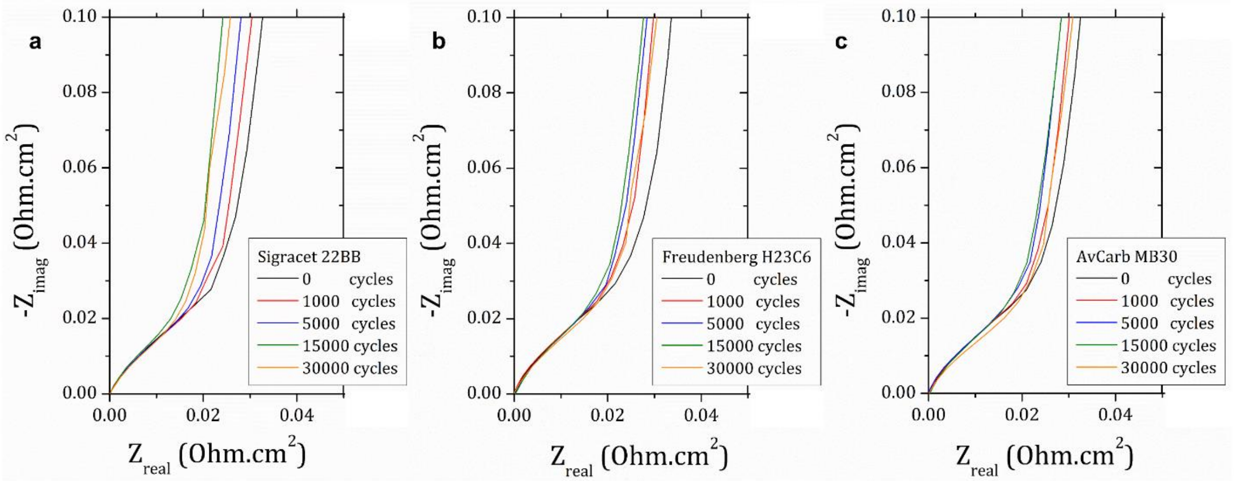

Figure 4.22 *Potentiostatic electrochemical impedance spectroscopies collected in H_2/N_2 (anode/cathode) at 80°C in 100 % RH under atmospheric pressure at various stages of the AST for each GDL MEA. a, Sigracet 22BB b, Freudenberg H23C6 and c, AvCarb MB30.*

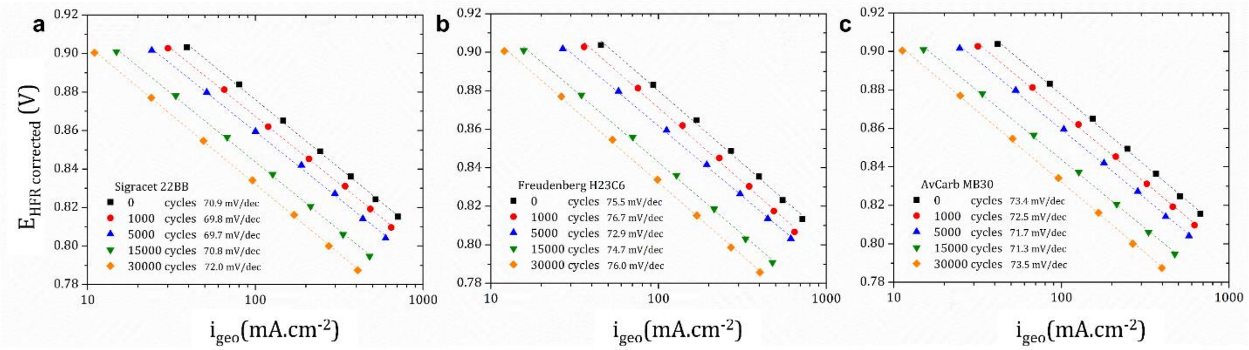

Figure 4.23 *Tafel plots generated from polarization data collected in H_2/O_2 (anode/cathode) at 80°C in 100 % RH under 150 kPa (a) pressure at various stages of the AST for each GDL MEA. a, Sigracet 22BB b, Freudenberg H23C6 and c, AvCarb MB30.*

4.2.3. Analysis of Pt nanoparticle size and Pt loading after N_2 AST

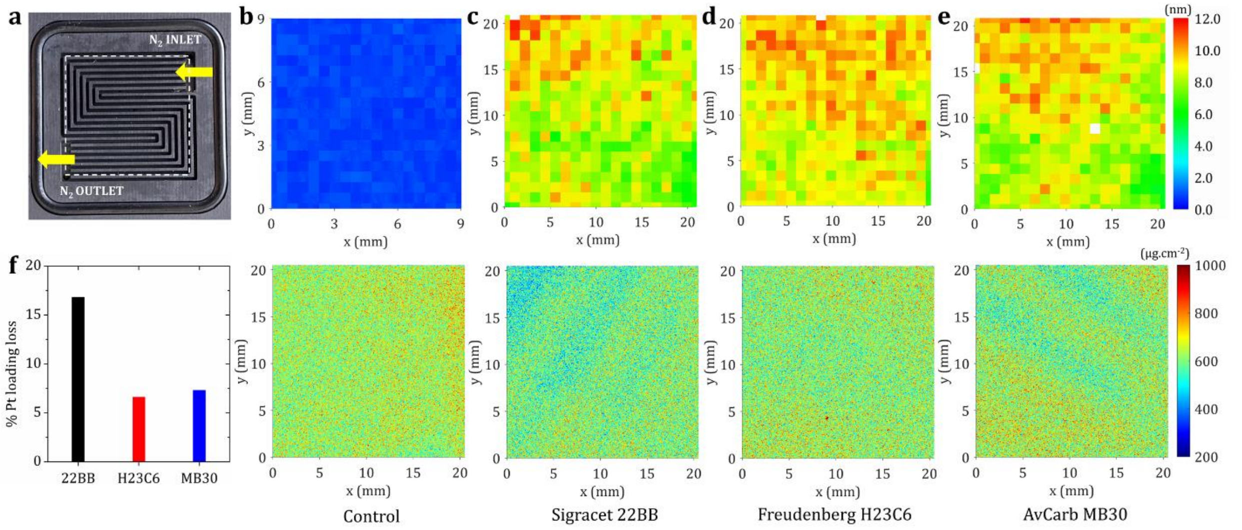

Figure 4.24 *a, Mapped area of the flow field with inlet and outlet marked. b - e, (Above) micro x-ray diffraction maps and (below) micro x-ray fluorescence maps. f, Percentage of average Pt loading loss for each GDL MEA after nitrogen environment AST.*

Active area (4 cm^2) of each GDL was mapped before and after the nitrogen environment AST using μ-XRD and μ-XRF techniques to study the Pt nanoparticle size growth and Pt mass loading changes. **Figure 4.24 a** shows the 2 cm by 2 cm mapped area with respect to the 5 cm^2 flow field used. **Figure 4.24 b- e** show μ-XRD maps (above) and normalized μ-XRF maps (below) for control, 22BB, H23C6 and MB30 respectively. An average Pt nanoparticle size of 2.69 ± 0.10 nm can be observed for the control sample (i.e. before AST). An average Pt nanoparticle size of 9.08 nm ±0.86 nm was observed for 22BB while an average Pt nanoparticle size of 9.11 nm ± 0.82 nm and 9.26 nm ± 1.54 nm was observed for H23C6 and MB30, respectively. All the MEAs showed a significant increase in the Pt nanoparticle size after nitrogen AST, resulting from electrochemical Ostwald ripening mechanism. Somewhat similar distribution of Pt nanoparticle size in the 2D mapping is observed for 22BB, H23C6 and MB30. Generally, larger nanoparticle size area is located at the first 90° turn, near inlet, of the serpentine flow field. In H23C6, the larger nanoparticle size area extends further to the next 90° turn, compared to 22BB and MB30. Even though all the three MEAs show heterogeneity with a greater increase in Pt nanoparticle size closer to the inlet, some degree of heterogeneity can be observed for the MEA having 22BB compared to H23C6 and MB30. To further understand this degradation heterogeneity, micro XRF maps were analyzed and quantified. An average Pt loading of 601 $\mu g.cm^{-2}$ was seen for the control sample, which is a summation of the anode and cathode Pt loadings. All the GDLs showed some amount of Pt loading loss from the cathode catalyst layers loadings evident from the μ-XRF maps normalized using control sample loading (to eliminate sample to sample variation and clearly understand the effect of GDLs). Like the μ-XRD maps, a difference in average Pt loading after AST (**Table 4.7**) was clearly noticed between the three MEAs with 22BB showing the lowest average Pt loading. **Figure 4.24 f** shows MEA with 22BB having ∼ 16 % loss of initial Pt loading, which is more than twice when compared to H23C6 and MB30 that show a Pt loading loss of ~ 6-7%.

Table 4.7 *Average Pt loading before vs after AST for each GDL MEA from x-ray fluorescence with estimated Pt loading loss %.*

Gas Diffusion Layer	**Average Pt loading ($\mu g.cm^{-2}$)**					
	N_2 AST			Air AST		
	Before AST (1.2 mm capillary spots)	After AST (10 µm capillary map)	% Pt loading loss from cathode	Before AST (1.2 mm capillary)	After AST (10 µm capillary)	% Pt loading loss from cathode
Sigracet 22BB	558	511	16.8	562	541	7.5
Freudenberg H23C6	609	589	6.6	545	535	3.7
AvCarb MB30	550	530	7.3	-	-	

Understanding of GDL morphology from the µ-XCT data suggests that this difference in Pt nanoparticle size increase and average Pt loading loss between MEAs having 22BB vs H23C6 and MB30 could be related to the presence of MPL cracks in 22BB. Presence of MPL cracks can result in a higher flux of liquid water from the cathode catalyst layer. Therefore, a much larger fraction of the Pt ions have a high probability of leaving the cathode catalyst layer through effluent water. This explains the lower increase in average Pt nanoparticle size and decrease in average Pt loading (after AST in 22BB) as a lower fraction of Pt ions are available for redeposition on nearby larger nanoparticles. Previously, an operando small angle x-ray scattering study has shown significant loss of Pt loading in flowing conditions when compared to stagnant conditions [30]. In addition to this, multiple studies have reported such heterogeneity in Pt nanoparticle size increase (between inlet-outlet and land-channel) [28,29,52] and loss or change in cathode catalyst layer Pt loading [31], which can be explained through differences in liquid water flux.

4.2.4. Electrochemical characterization data after air AST

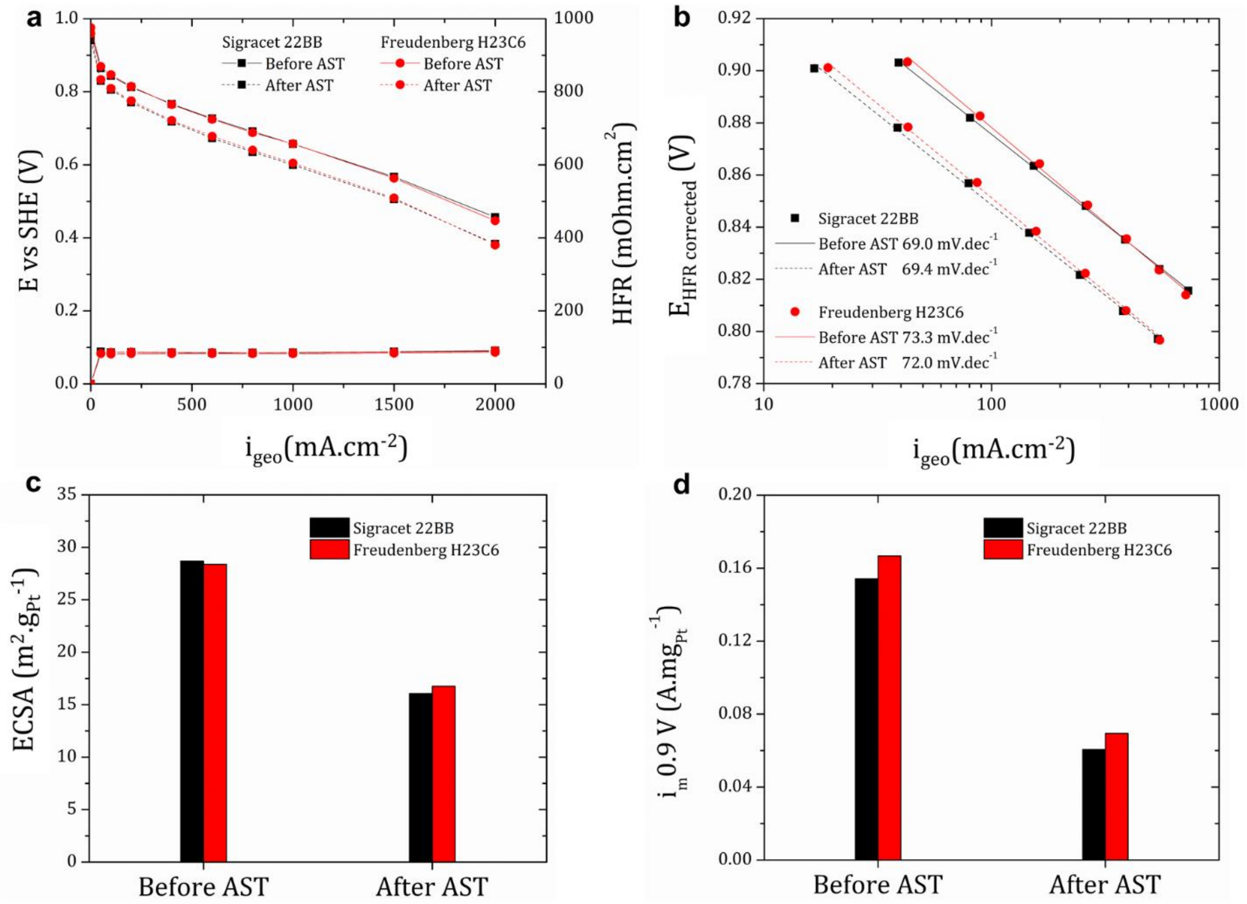

Figure 4.25 *a, Before vs after AST differential polarization curves collected at 80°C in 100% RH under 150 kPa (a) pressure. b, Before vs after AST Tafel plots generated from polarization data collected in oxygen environment. c, Before vs after AST ECSA. d, Before vs after AST mass activity calculated from Tafel plots at 0.9 V.*

To confirm the average Pt loading loss trend and solidify that Pt oxide coverage and hence degradation at 100% RH will not be affected by electrochemically produced water (due to Kelvin effect), MEAs were subjected to AST in air environment on the cathode. GDLs 22BB and H23C6 were selected as they display a significant difference between their morphologies. **Figure 4.25** shows before and after air AST electrochemical characterization. Like nitrogen environment ASTs, no difference is observed in the polarization curves in **Figure 4.25 a** between the two MEAs after degradation. The voltage loss at 0.8 A.cm^{-2} is ~ 50 mV which is half of that seen in the nitrogen environment. The average Pt nanoparticle size after air AST for both the GDLs was ~ 3.90 +0.31 nm which is also significantly lower compared to nitrogen ASTs. This difference between particle size in N_2 AST and air AST is primarily due to the decreasing UPL limit during voltage cycling in case of air ASTs (as UPL is set to be OCV in air AST case) highlighted by **Figure 3.4 a** and **b**. **Figure 3.4 b** also shows that the voltage cycling profile experienced by both the GDLs over the course of AST was similar. **Figure 4.25 b** shows Tafel plots before and after AST with little to no difference between the two MEAs after degradation. The Tafel slope shows minimal change, as well. Therefore, the calculated mass activity at 0.9 V plotted in **Figure 4.25 d** is similar after degradation. A loss of ~ 60% of initial mass activity was observed. **Figure 4.25 c** shows initial ECSA values of 29.8 m^2.g^{-1} and 28.9 m^2.g^{-1} for 22BB and H23C6 respectively. The slightly lower ECSA values for the air AST MEAs are from batch-to-batch variation. Almost 50% of initial ECSA was lost after the air AST. Therefore, it can be confirmed that, like nitrogen ASTs, no difference in electrochemical performance was noted after degradation in air ASTs for 22BB and H23C6. **Figure 4.26** shows additional electrochemical characterization while **Figure 4.27** shows μ-XRF maps of control sample along with 22BB and H23C6 after air AST.

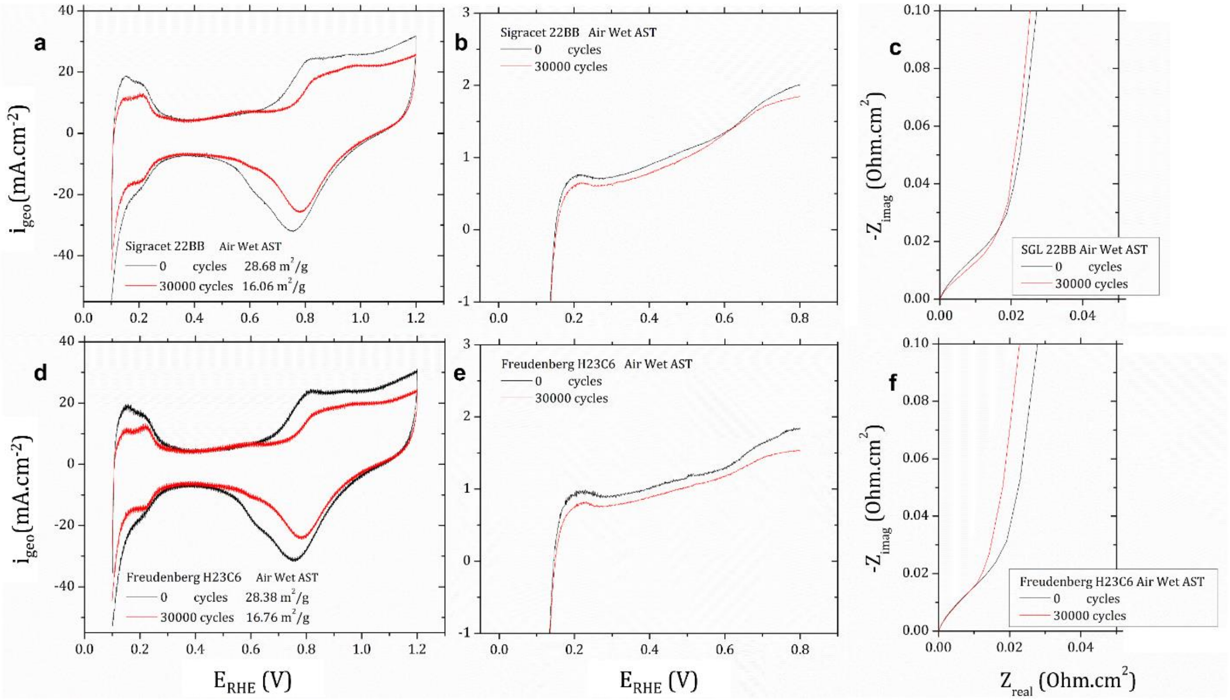

Figure 4.26 *Cyclic voltammograms, linear sweep voltammograms and electrochemical impedance spectroscopies (left to right) before and after air environment AST. a,b and c, Sigracet 22BB. d, e, and f Freudenberg H23C6.*

A similar difference of average Pt loading loss can be seen between MEAs having 22BB (7.5 %) and H23C6 (3.7 %) GDLs after air AST. The overall percentage of loading loss has decreased for both MEAs due to decreasing UPL, but the difference caused due to the GDLs has stayed constant.

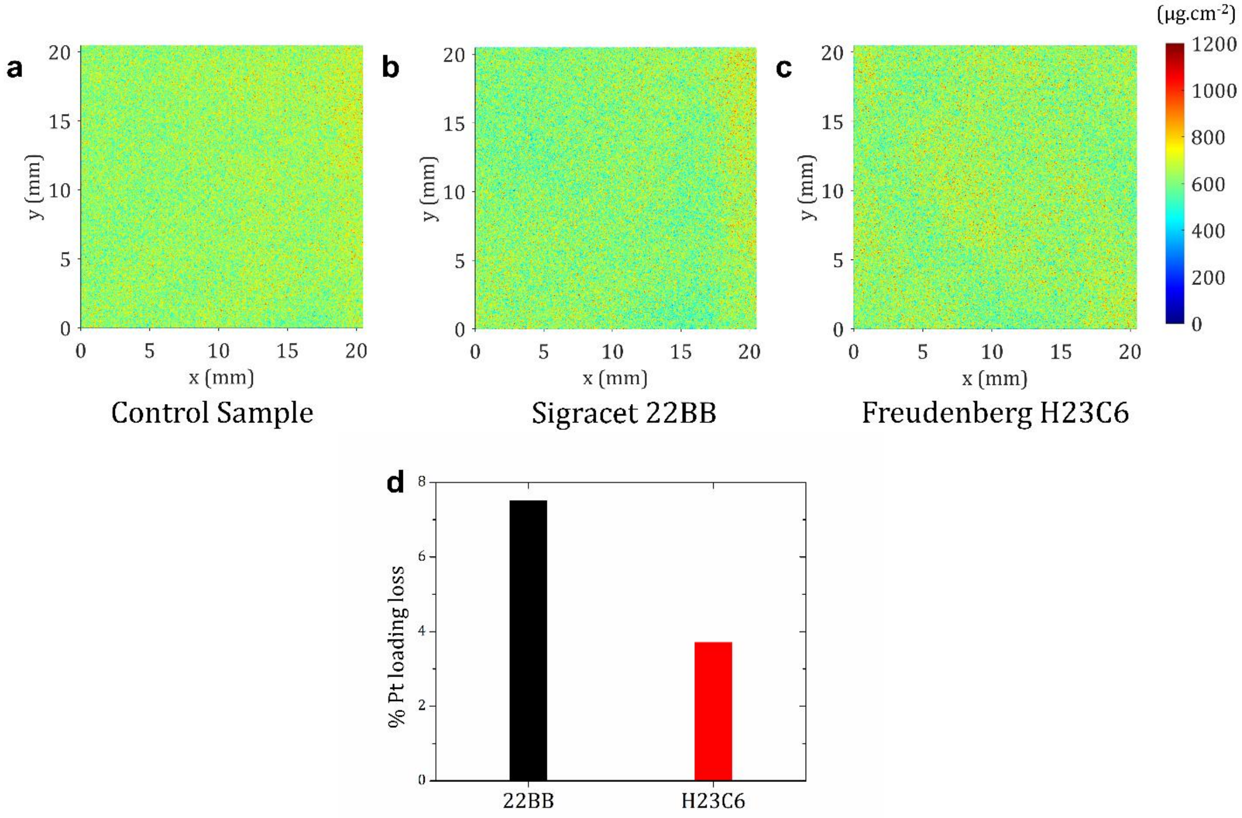

Figure 4.27 *4 cm^2 μ-X-ray fluorescence maps after air environment AST of MEAs with Sigracet 22BB and Freudenberg H23C6 GDLs d, percentage loss in average Pt loading after air AST.*

4.2.5. Lattice Boltzmann simulations of water transport in gas diffusion layers

Lastly, computational fluid dynamic (CFD) simulations using Lattice Boltzmann method (LBM) were performed to simulate water transport through the GDLs. X-ray CT images were used as simulation domains. **Figure 4.28 a, b** and **c** show 3D reconstructions of 22BB, H23C6 and MB30 with simulated flow of liquid water through the GDLs (above) along with 2D colormap cross sections of liquid water saturation (below). Water was injected at the bottom of the MPL, to simulate liquid water formation (electrochemically produced or condensed) in the cathode catalyst layer and transport through the MPL. After injection, liquid water starts building up pressure to escape through the hydrophobic pores of the MPL. In the case of 22BB the breakthrough pressure was found to be at 8.5 kPa. This low value is due to the presence of MPL cracks, as they provide a low-pressure preferential pathway for water to escape. This can be seen from the breakthrough pressure difference between 22BB vs H23C6 and MB30 in **Figure 4.28 d**.

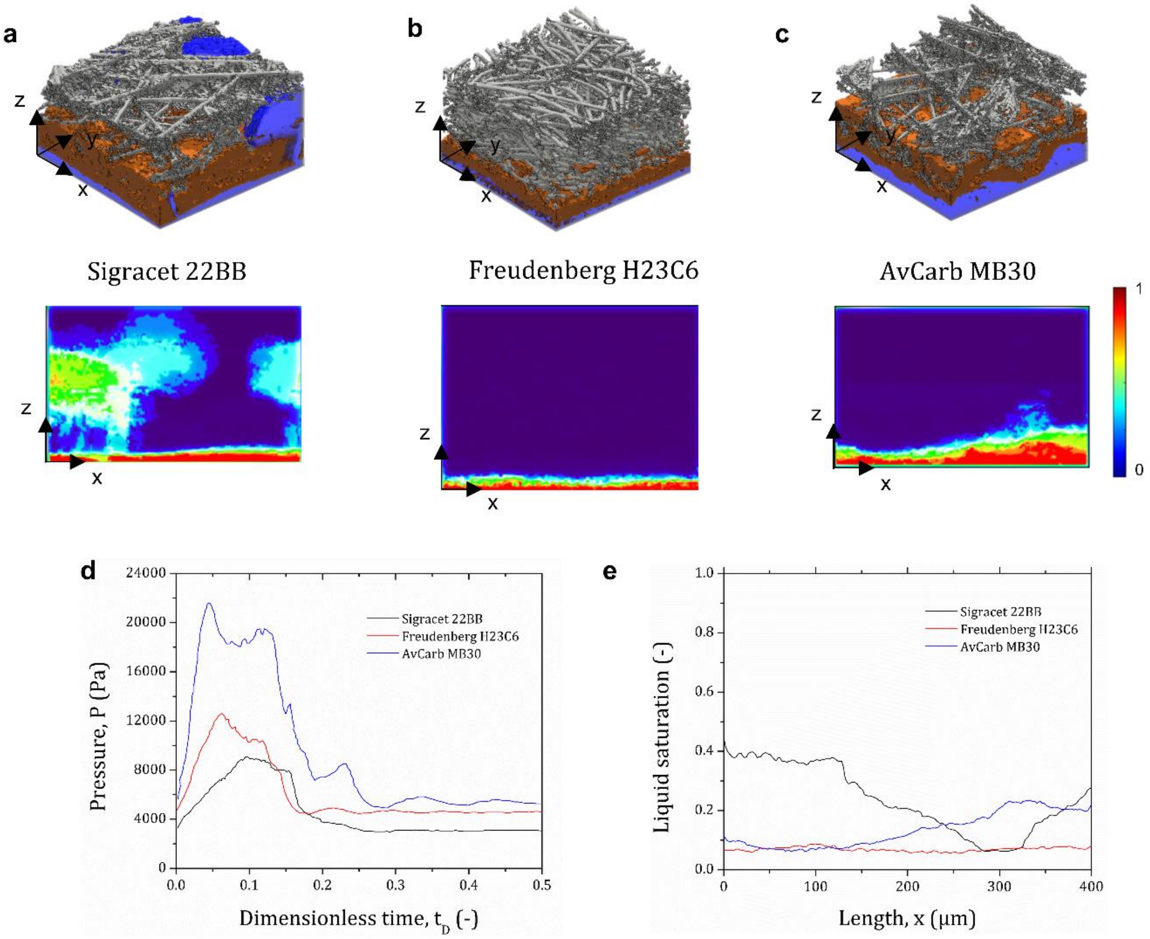

Figure 4.28 *a, b, and c, (Above) 3D reconstructions of liquid water saturation simulation, (below) 2D colormaps of liquid water saturation. d, Breakthrough pressure as function of time. e, Liquid water saturation as a function of length.*

A breakthrough pressure of 8.5 kPa was observed for 22BB while 12.8 kPa and 21.9 kPa pressures were observed for H23C6 and MB30, respectively. **Table 4.8** contains stagnation pressure for each GDL. All the data confirms a higher flux of liquid water in the cathode catalyst layer with 22BB as the GDL compared to H23C6 and MB30. This results in loss of dissolved Pt ions from the cathode catalyst layer via effluent water as confirmed by the micro XRF maps previously. Average liquid water saturation (**Figure 4.28 e**) inside GDS was observed to be highest for 22BB (24%) resulting in better liquid water removal from the cathode catalyst layer due to MPL cracks. H23C6 and MB30 show much lower liquid water saturation of 7% and 13%, respectively resulting in low liquid water flux.

Table 4.8 *Stagnation pressure for 22BB, H23C6 and MB30 calculated from CFD simulations using LBM.*

Samples	Stagnation pressure
H23C6	4,897 [Pa]
22BB	3,765 [Pa]
MB30	6,122 [Pa]

4.3. *Chapter 3:* Correlating the morphological changes to electrochemical performance during carbon corrosion

Despite many studies, it is still unclear what chain of events are triggered by carbon corrosion and how these morphological changes affect electrochemical performance. This study attempts to understand the complex interplay. Commercially available CCMs were subjected to the DOE carbon corrosion AST up to 2000 AST cycles. Standard electrochemical tests were performed to diagnose the electrode health at the BOL after 100, 500, and 2000 AST cycles. Carbon loss was quantified by NDIR spectroscopy. Cathode catalyst layer thickness was measured by SEM. FIB-SEM was used to study the change in the pore structure. XPS was used to measure the concentration of oxides on the carbon surface to qualitatively study the change in hydrophilic behavior. Lastly, μ-XRD and μ-XRF were used to measure catalyst nanoparticle size and catalyst loading respectively.

4.3.1. Electrochemical performance and cathode catalyst layer carbon loss

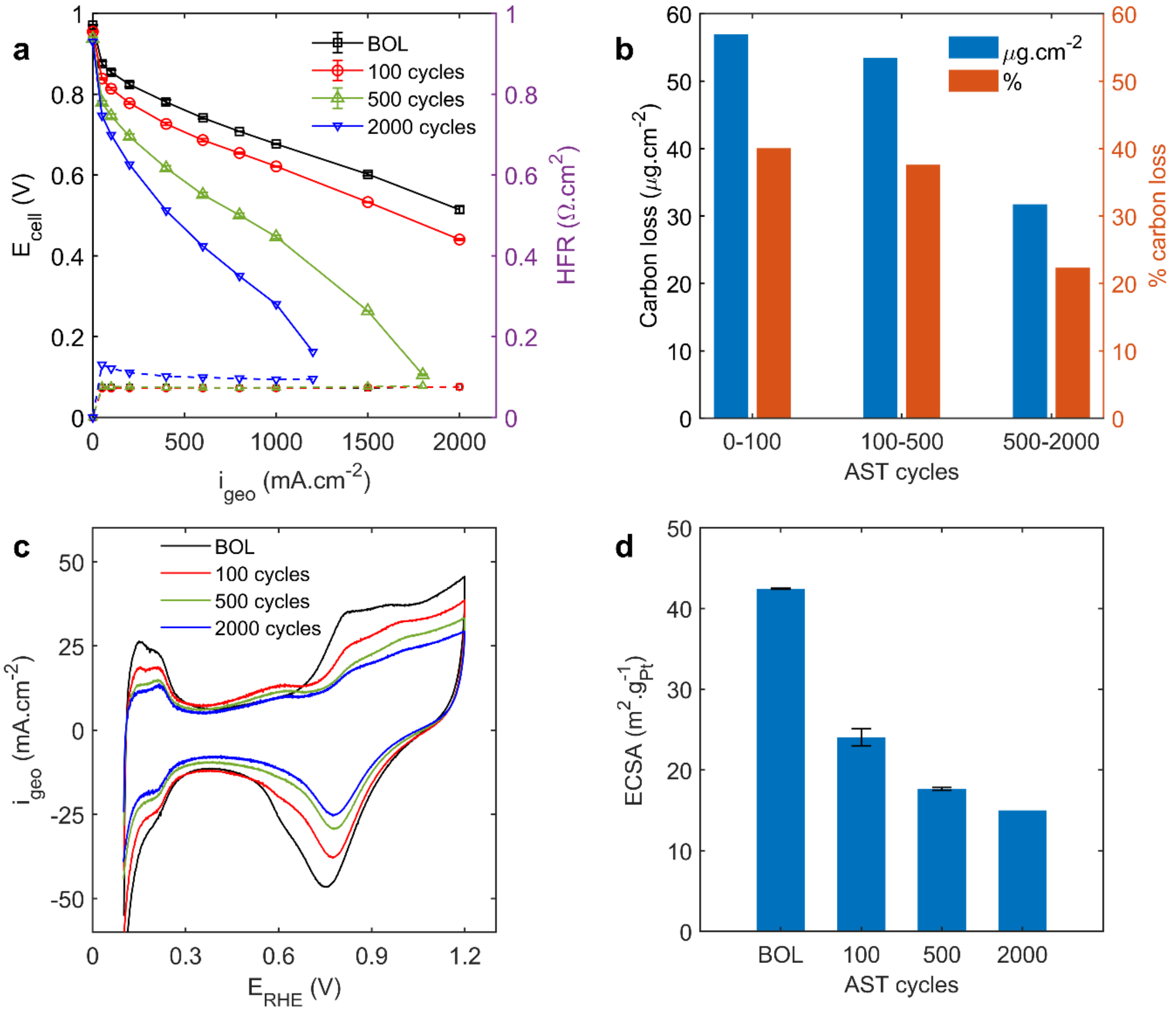

Figure 4.29 *a, Differential polarization curves in air collected at the BOL, after 100, 500, 2000 AST cycles with HFR plotted on the right y-axis. b, Carbon loss estimated from NDIR spectroscopy for 0-100, 100-500 and 500-2000 AST cycles. c, Cyclic voltammograms. d, ECSA at BOL, after 100, 500, and 2000 AST cycles. Carbon loss is plotted in both, absolute amount (μg.cm*$^{-2}$*) and corresponding percentage from the total carbon lost.*

Figure 4.29 provides a discussion on the quantification of carbon loss during AST and its effects on the electrochemical performance of the MEA at various stages of AST. **Figure 4.29 a** shows the polarization curves collected in H_2/air (anode/cathode) environment at 80°C in 100% RH under 150 kPa backpressure in differential conditions. The high frequency resistance (HFR) is also measured and plotted. The cell overpotential increased after carbon corrosion, but two distinct trends were observed. After 100 AST cycles, there was no visible mass transport limitation. The HFR remained almost unchanged (75 $m\Omega.cm^2$). The increase in overpotential is mostly kinetic and can be attributed to the loss of the ECSA (**Figure 4.29 d**). After 500 AST cycles, the slope in the high current density increases which indicates a significant increase in the O_2 mass transport resistance (MTR), which will be shown later in **Figure 4.34 c**. After 2000 AST cycles, the HFR increased to 100 $m\Omega.cm^2$ and the polarization curve showed severe mass transport limitation. This observation suggests a possible collapse of cathode catalyst layer pore structure. **Figure 4.29 b** shows the amount of carbon lost calculated from the NDIR measurements. Carbon loss during different AST cycles was the following- 57 $\mu g.cm^{-2}$ during the first 100 cycles (~ 40% of the total loss), 53.5 $\mu g.cm^{-2}$ during the next 400 cycles (~ 38% of the total loss), and 32 $\mu g.cm^{-2}$ during the last 1500 cycles (~ 22% of the total loss). **Figure 4.29 b** also shows that carbon loss rate decreases with ageing. Amorphous carbon in disordered domains corroded faster than graphitic carbon, whose oxidation rate was much slower [37]. The amount of amorphous carbon reduced with ageing, and the corrosion rate slowed down. **Figure 4.29 c** and **d** show how CV and ECSA changed during the carbon corrosion AST. ECSA was calculated from the CVs by integrating the charge in the hydrogen underpotential deposition (H-UPD) region and dividing it by the monolayer H-UPD charge of 210 $\mu C \cdot cm^{-2}$ (standard value for an electrochemically clean and polished polycrystalline Pt [72]). **Figure 4.29 c** shows that the current in both H-UPD and oxide regions decreased with ageing. However, in the capacitive region (~ 0.3-0.6 V) during the anodic scan, current density was maximum after 100 AST cycles and then decreased afterwards. The increase of current in this potential window, despite decreasing capacitance with ageing (**Figure 4.31 a**), was due to quinone oxidation [73]. This trend is consistent with previous observations [74]. It is likely that quinone oxidation predominantly occurred on the amorphous carbon. With ageing, the amount of amorphous carbon decreased, and quinone oxidation rate decreased subsequently. **Figure 4.29 d** shows that ECSA decreased monotonically with ageing from 42.4 $m^2.g^{-1}{}_{Pt}$ at BOL to 15 $m^2.g^{-1}{}_{Pt}$ after 2000 AST cycles. Hence, nearly 65% of the initially active Pt area was lost after 2000 AST cycles. The loss of ECSA did not exactly correlate with the rate of carbon corrosion. Comparing **Figure 4.29 b** and **d**, although carbon loss in the first 100 AST cycles was similar to that in the next 400 AST cycles, ECSA loss was almost 3 times higher in the first 100 AST cycles. Overall, both ECSA (65% of the total) and carbon (40% of the total) losses were fastest during the first 100 AST cycles.

4.3.2. Analysis of Pt nanoparticle size and loading

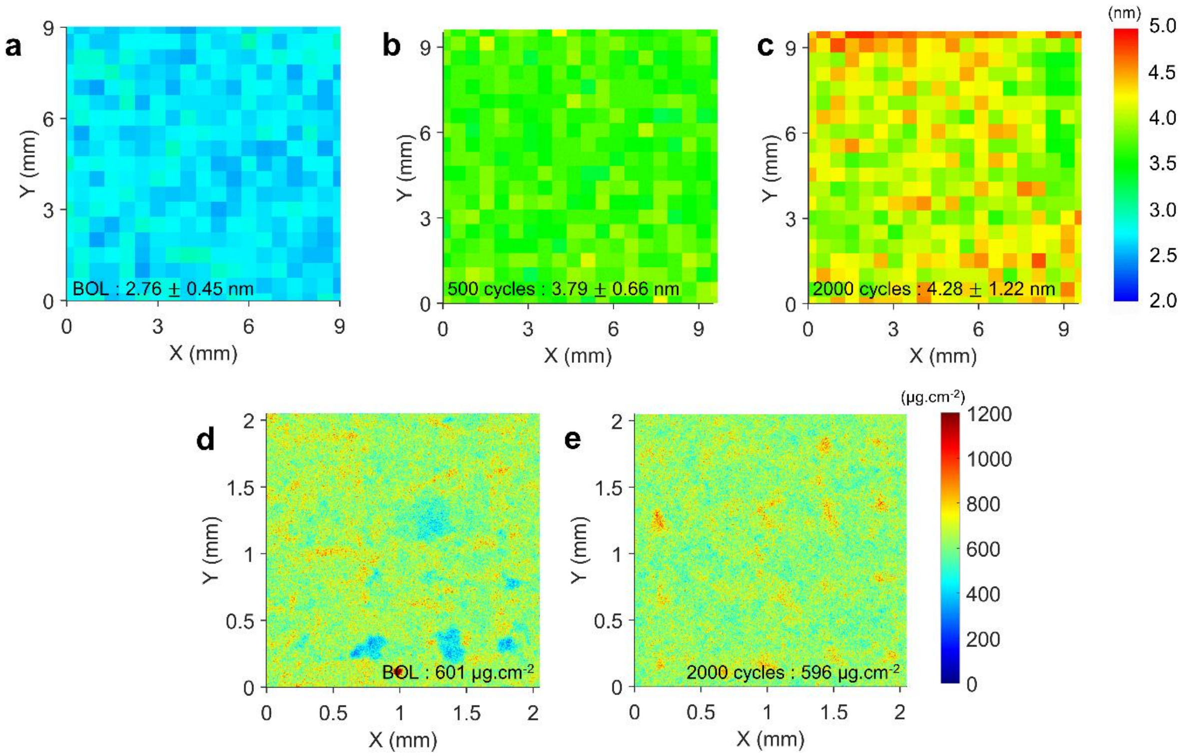

Figure 4.30 *a, b, and c, μ-XRD maps with average Pt nanoparticle size at BOL, after 500 and after 2000 AST cycles. d, and e, μ-XRF maps with average Pt loading at BOL and after 2000 AST cycles.*

Pt loading and nanoparticle size distribution data is required to understand the reason for ECSA loss after carbon corrosion. **Figure 4.30 a, b,** and **c** show the μ-XRD maps of average Pt crystallite sizes over 1 cm^2 area (20% of the entire MEA) at BOL, after 500, and 2000 AST cycles. **Figure 4.30 d** and **e** show the μ-XRF maps of Pt loading at BOL and after 2000 AST cycles. **Figure 4.30 a, b,** and **c** show that the median size of Pt nanoparticles increased from 2.76 nm at the BOL to 3.79 nm after 500 AST cycles, and finally to 4.28 nm after 2000 AST cycles. μ-XRF maps in **Figure 4.30 d** and **e** show that the average Pt loading in the MEA did not change even with 65% loss in the cathode catalyst layer thickness (**Figure 4.32**) after 2000 AST cycles. This rules out any Pt loss from the MEA and any ECSA loss due to it. The combined facts of: i) largest ECSA decrease (65% of total loss) and ii) fastest carbon corrosion rate (40% of total loss) during the first 100 AST cycles, and iii) carbon in the disordered domains that preferentially contain Pt nanoparticles oxidized fast, strongly suggest that Pt detachment was the principal reason for the loss of ECSA. Pt nanoparticles located on amorphous carbon detached rapidly, which contributed to most of the total ECSA loss. Pt agglomeration occurred simultaneously although not as aggressively and continued to occur until the end of AST. Only 10% of the total ECSA loss occurred in the last 1500 AST cycles, indicating that the remaining Pt that did not detach during ageing, was most likely bonded to the graphitic carbon. This might also explain why the increase in Pt nanoparticle size was so small compared to the catalyst corrosion AST (0.6-0.95 V cycling) with similar ECSA loss [29]. Additional evidence is necessary to understand if agglomeration of Pt occurred on the surface of the carbon support [75] or in the ionomer-liquid phase.

4.3.3. Impact of carbon corrosion on cathode catalyst layer conductivity

The effects of carbon corrosion on Ohmic resistance (R_{Ohmic}), proton transport resistance (sheet resistance R_{Sheet}) and double layer capacitance (sheet capacitance C_{Sheet}) of the cathode catalyst layer, studied by EIS, are shown in **Figure 4.31**. The EIS datasets were fitted with a transmission line model as discussed by Eikerling and Kornyshev [42]. In the equivalent transmission line model, it was assumed that the charging is purely capacitive (electronic). Sheet resistance and capacitance are strongly dependent on the structural properties of the cathode catalyst layer, which generally change during carbon corrosion. The sheet capacitance was due to both Pt and carbon. Details of the fitting procedure, with individual plots with standard errors are discussed in section 3.5.3.

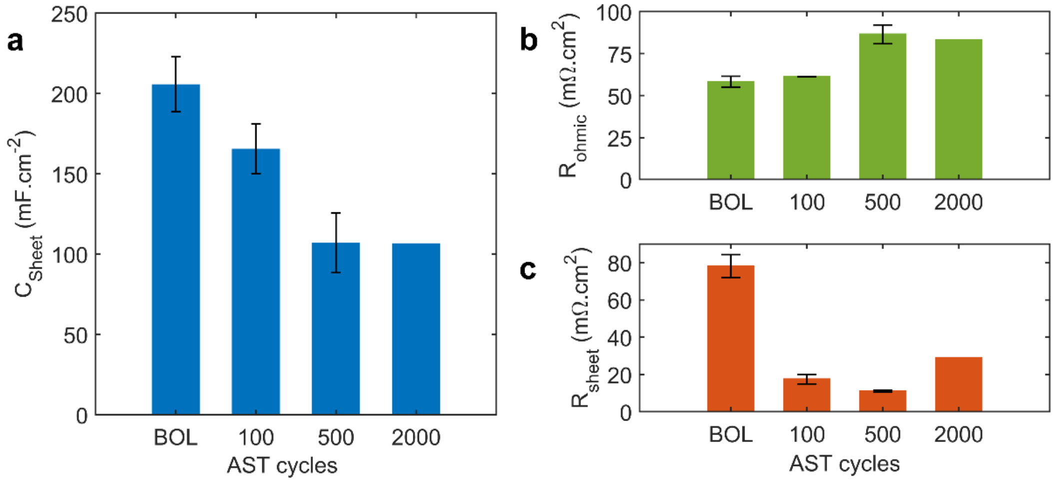

***Figure 4.31** a, Sheet capacitance b, ohmic resistance and c, sheet resistance of the cathode catalyst layer at BOL, 100, 500 and 2000 AST cycles.*

Figure 4.31 a shows that sheet capacitance of the cathode catalyst layer decreased monotonically from an initial BOL value of 206 mF.cm^{-2} to 107 mF.cm^{-2} after 500 AST cycles and remained nearly constant for the last 1500 AST cycles. The measured BOL value of sheet capacitance is in good agreement with value reported by Liu et al. for Pt/Vulcan and I/C ratio ~ 1 [76]. Similar loss in sheet capacitance due to carbon corrosion was observed before [77]. The loss of sheet capacitance with ageing was due to: (i) reduction in the effective carbon surface area due to corrosion, and (ii) loss of Pt ECSA. Overall, carbon and Pt ECSA losses correlate well with the decreasing sheet capacitance. In **Figure 4.31 b**, the ohmic resistance (R_{Ohmic}) remained nearly constant up to the first 100 AST cycles (~ 60 mΩ.cm^2), increased to ~ 86 mΩ.cm^2 after 500 AST cycles and remained nearly unchanged for the rest of the AST. Jung *et al*. reported a similar trend [78]. As carbon provided the electronic conductive pathway, its corrosion most likely increased the contact resistances between the cathode catalyst layer and the diffusion media. R_{Ohmic} most likely increased as a result of that. **Figure 4.31 c** shows that the sheet resistance decreased from 78 mΩ.cm^2 at BOL to 14 mΩ.cm^2 after 500 AST cycles, and then increased to 29 mΩ-cm^2. The BOL value is in good agreement with that reported by Makharia *et al*. [79] for I/C = 0.8 with Pt/Vulcan carbon catalyst. SEM images of cathode catalyst layer (**Figure 4.32**) show that the thickness decreased from 11.9±1.4 μm at BOL to 5.0±1.1 μm after 500 AST cycles, and finally to 4.2±0.8 μm after 2000 AST cycles. As a result of this electrode thinning from carbon loss, H$^+$ transport length was reduced, and its transport resistance decreased. The maximum decrease in sheet resistance was observed between BOL and 100 AST cycles (61 mΩ-cm^2), which correlates with a large carbon loss in the first 100 AST cycles (57 μg.cm^{-2}). This indicates that thinning might have occurred at the highest rate during the first 100 AST cycles. In absence of any pore structural collapse, the sheet resistance should have monotonically decreased. This trend is observed up to 500 cycles. The increase after 2000 AST cycles might be related to a change in ionomer network as a result of a drastic change in the pore structure. It will be shown later in **Figure 4.33** that a structural collapse occurred during the last 1500 AST cycles. Both porosity and pore percolation decreased significantly. This might have resulted in discontinuity in the ionomer network as well as inefficient hydration inside the electrode. Since H$^+$ ion conductivity through ionomer decreases with the decreasing hydration, sheet resistance increased.

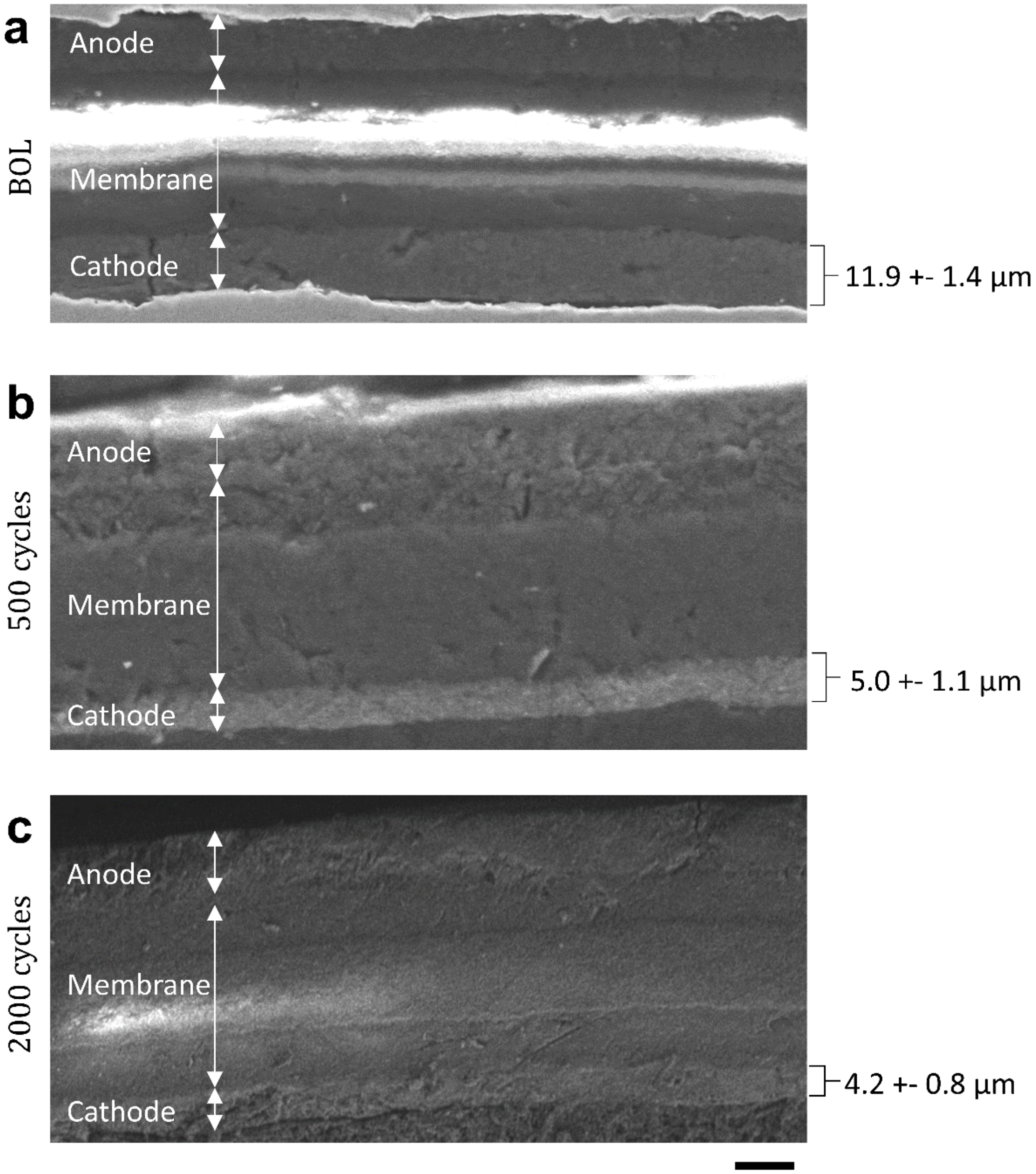

Figure 4.32 *Reduction in thickness of cathode catalyst layer due to carbon corrosion. a, BOL. b, After 500 AST cycles. c, After 2000 AST cycles. The bright spots are due to charge accumulation in the membrane which is electronically non-conductive. Scale bar is 10 µm.*

4.3.4. Cathode catalyst layer pore structure analysis

Pore structure evolution during carbon corrosion AST was analyzed using FIB-SEM and is shown in **Figure 4.33**. **Figure 4.33 a** shows the 3D reconstruction of the solid and void phases inside the catalyst layer, **Figure 4.33 b** shows representative 2D slices, **Figure 4.33 c** shows the pore size (diameter) distribution, **Figure 4.33 d** shows the pore-space tortuosity, and **Figure 4.33 e** shows the variation of porosity as a function of through plane distance inside the cathode catalyst layer. The solid phase comprises of Pt, carbon, and the ionomer. The discrete pore size data was fit with a log-normal distribution [19]. Details of the FIB-SEM image analyses and the pore size distribution fitting are provided in section 3.6.2.

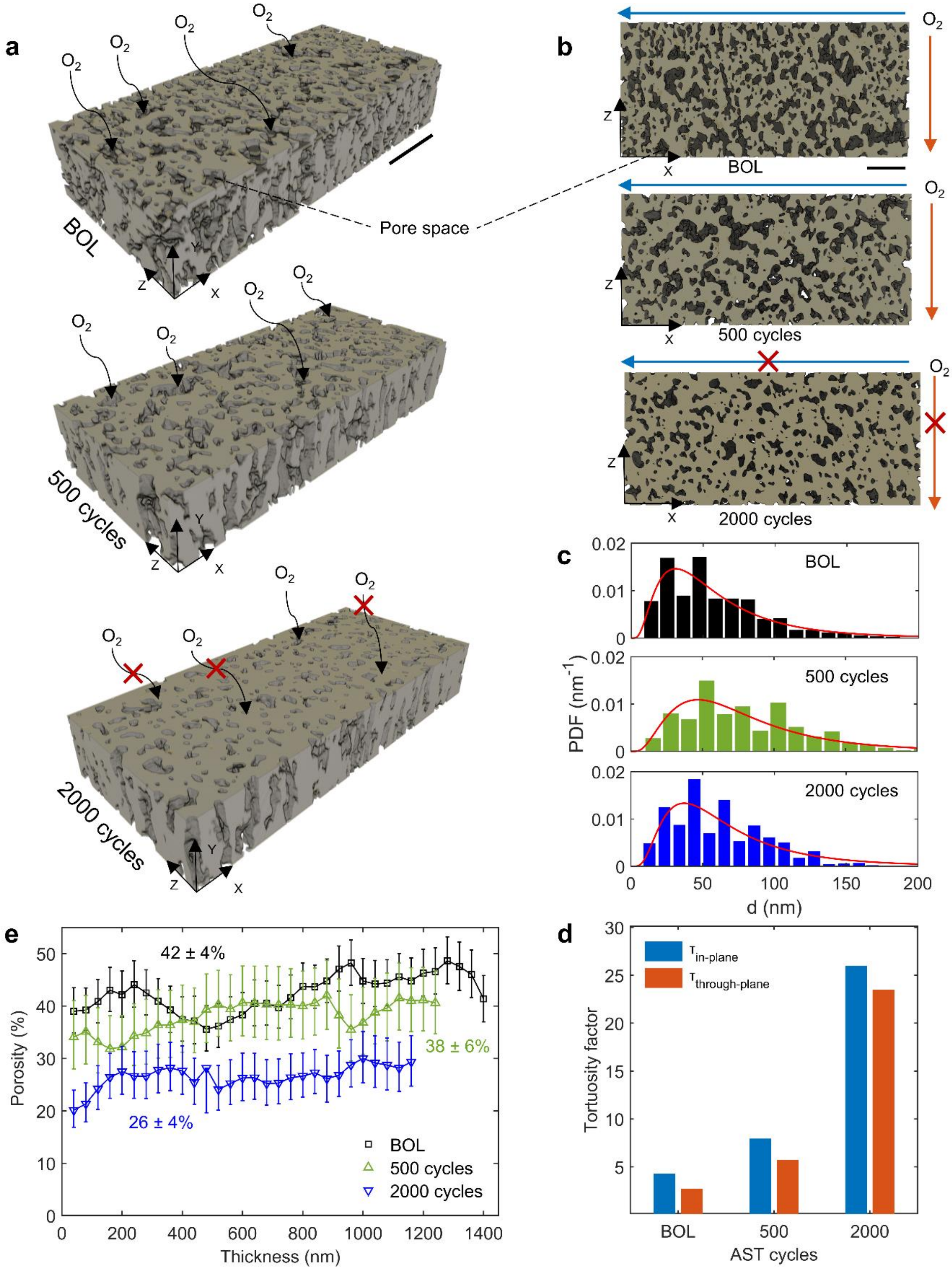

Figure 4.33 *a, 3D reconstruction of the solid phase and the pores with b, corresponding 2D view highlighting pore connectivity and oxygen diffusivity. c, Pore diameter distributions with log-normal fits. d, In-plane and through-plane pore space tortuosity factors. e, Porosity of the cathode catalyst layer as a function of its thickness, where 0 corresponds to the location of the first slice. Scale bars, 1 μm.*

The decrease in porosity with ageing is clear from the 3D reconstructions in **Figure 4.33 a,** and also from the corresponding in-plane 2D view in **Figure 4.33 b**. **Figure 4.33 a** also shows that pore connectivity decreased with ageing. The mean porosity of the cathode catalyst layer at BOL was 42 ± 4%. The observed porosity is consistent with that measured by others using FIB-SEM and porosimetry [80–82]. After 500 AST cycles, the porosity decreased slightly to 38 ± 6%. This decrease is low compared to the significant reduction in cathode catalyst layer thickness observed after 500 AST cycles from SEM (~5.9 μm). After 2000 AST cycles, the porosity decreased to 26 ± 4% with only slight change in the cathode catalyst layer thickness (~0.8 μm). Porosity decreased by 12% during the last 1500 AST cycles. **Figure 4.33 c** shows that the mean pore diameter at BOL was 50.6 nm, increased to 72.1 nm after 500 AST cycles, and then decreased to 55.7 nm after 2000 AST cycles. The mean values were calculated from the raw data instead of the fitting function. **Figure 4.33 c** also shows that the pores less than 50 nm in diameter decreased in number after 500 AST cycles. This observation indicates that carbon from the smaller pores oxidized faster than carbon from the larger pores, probably because smaller pores were in the disordered domains that oxidized faster. As a result, the smaller pores became larger, and the mean diameter increased. An opposite trend was observed during the last 1500 AST cycles. Pores smaller than 50 nm increased in number while those larger than 50 nm decreased in number. This is most likely due to the pore structure collapse that occurred in this period. Larger pores collapsed and the mean pore diameter decreased as a consequence. **Figure 4.33 d** shows that both the in-plane and through-plane pore-space tortuosity factors increased with ageing. The in-plane tortuosity was 4.28 at BOL. After 500 AST cycles, it increased to 7.95. After 2000 AST cycles, it increased to 26 which is nearly 6 times the BOL value. Similarly, the through plane pore space tortuosity was 2.7 at the BOL. After 500 AST cycles, it increased to 5.73, and after 2000 AST cycles, it increased to 23.5. So, during the last 1500 AST cycles, the in-plane and through-plane tortuosity factors increased by 83% and 85.6% respectively. The overall data in **Figure 4.33** indicates that a significant pore structure collapse occurred during the last 1500 AST cycles.

FIB-SEM and NDIR spectroscopy data shows that changes in the pore structure were initiated as soon as carbon corrosion started. But porosity and pore connectivity did not change significantly during the first 500 AST cycles, even though almost 78% of the total carbon loss occurred. A major change in the pore structure was observed during the last 1500 cycles, when only 22% of the total carbon corrosion occurred. This implies that until sufficient carbon had corroded, the pore structure held the pressure of the cell hardware and did not collapse. This observation is significant as it explains the apparent lag between carbon loss and the pore structure collapse.

4.3.5. Impact of carbon corrosion on mass transport of the cathode catalyst layer

Figure 4.34 provides electrochemical evidence of pore structure collapse in the cathode catalyst layer. Differential polarization curves in H_2/O_2 environment were collected at 80°C in 100 % RH under 150 kPa of backpressure. The data was used to generate Tafel plots in the kinetic region shown in **Figure 4.34 a**. Kinetic parameters like Tafel slope and exchange current density were analyzed and used to calculate concentration overpotential in oxygen environment plotted in **Figure 4.34 b**. The detailed calculation of concentration overpotential is reported in section 3.5.4.

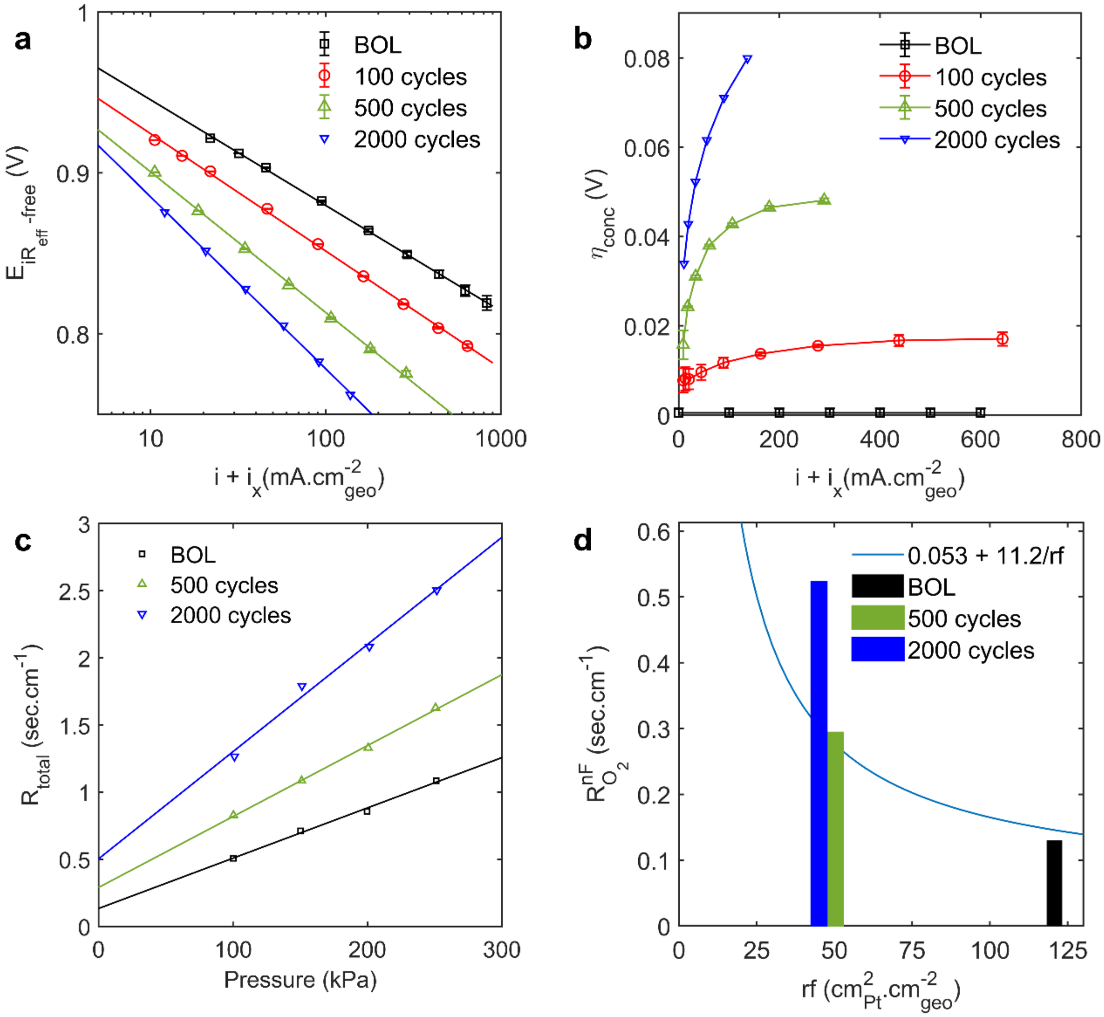

***Figure 4.34** a, Tafel plots with apparent increase in Tafel slope over the course of AST. b, Concentration overpotentials at low current densities in differential oxygen conditions. c, total O_2 MTR as a function of pressure and d, non-Fickian O_2 MTR as a function of decreasing roughness factor. The deviation of the MTR values from the 0.053 + 11.2/RF sec.cm^{-1} line after 2000 AST cycles indicates a severe pore structure collapse that occurred in the last 1500 AST cycles.*

Figure 4.34 a shows that Tafel slope increased with ageing in the following order: 71 mV.dec^{-1} at BOL, 76.8 mvV.dec^{-1} after 100 AST cycles, 87.4 mV.dec^{-1} after 500 AST cycles, and finally reached 106.8 mV.dec^{-1} after 2000 AST cycles. The slope was calculated after iR correction (with $R_{eff} = R_{Ohmic} + R_{Sheet}/3$) and H_2 crossover current correction [47]. The H_2 crossover current was estimated from LSVs (**Figure 3.7**). The Tafel slope is an intrinsic characteristic of the ORR on Pt and does not depend on electrode morphological parameters like ECSA, porosity etc. Thus, it is not supposed to be affected due to carbon corrosion. This observed increase in the Tafel slope with ageing was, therefore, an apparent effect. The iR correction included the R_{Sheet} contribution, so the change in H^+ conduction was already considered. **Figure 4.34 c** and **d** show that O_2 MTR increased significantly with ageing. Higher values of Tafel slope were, thus, an effect of mass transport limitation. Harzer *et al.* [23] and Arisetty *et al*. [83] observed similar increase in Tafel slope after catalyst corrosion AST (~ 0.6 – 0.95 V cycling). Assuming the Tafel slope to be equal to the BOL value of 71 $mV.dec^{-1}$ throughout ageing, η_{conc} was calculated for both H_2/O_2 and H_2/air environments. The detailed calculations are provided in section 3.5.4. (H_2/O_2 case) and 3.5.5. (H_2/air case). From the H_2/O_2 polarization curve at BOL, Tafel slope and the Pt area specific exchange current density were calculated. These two parameters were assumed to be constant throughout ageing. This data, along with the assumption that $\eta_{conc} \approx 0$ at BOL, were used to calculate η_{conc} at different ageing states. In the H_2/O_2 case, **Figure 4.34 b** shows that η_{conc} was less than 20 mV after 100 AST cycles, which is consistent with the slight apparent increase (~5.8 $mV.dec^{-1}$) in the Tafel slope from **Figure 4.34 a.** After 500 AST cycles, η_{conc} reached a maximum value of 48 mV at 289 $mA.cm^{-2}$. After 2000 cycles, η_{conc} sharply increased with the current density due to pore structure collapse and reached a maximum value of 80 mV at 136.6 $mA.cm^{-2}$. **Figure 4.35** shows that η_{conc} in the H_2/air environment increased with ageing, albeit with much higher values. This trend of increasing η_{conc} is due to the increasing O_2 MTR with ageing.

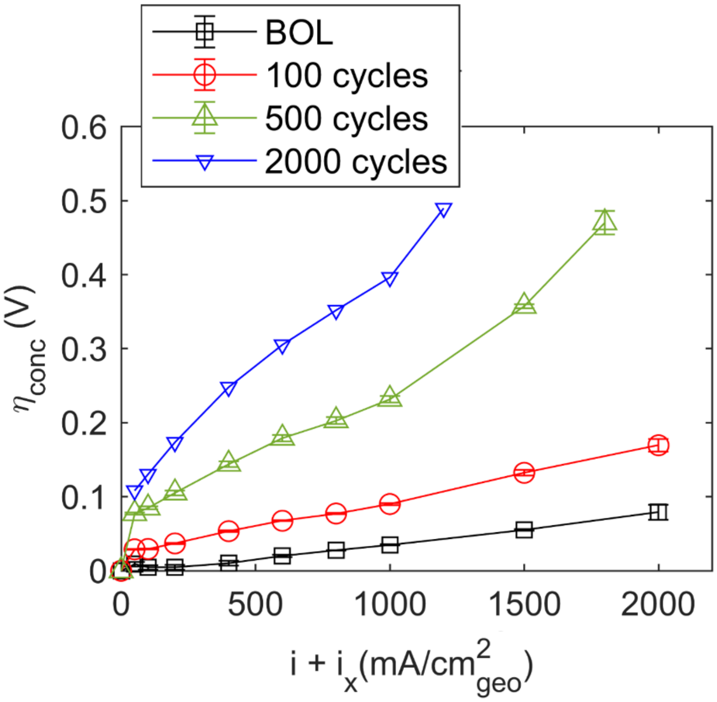

Figure 4.35 Concentration overpotential (in air) as a function of current density at different stages of carbon corrosion. I_x is the correction due to hydrogen crossover current density.

.

The O_2 mass transport resistance (MTR) was calculated at different AST stages using O_2 limiting current experiments and the results are shown in **Figure 4.34**. **Figure 4.34 c** shows the total O_2 MTR (R_{total}) as a function of backpressure, and **Figure 4.34 d** shows the non-Fickian or pressure independent O_2 MTR ($R_{O_2}^{nF}$) as a function of decreasing roughness factor (rf). Electrode roughness factor is the ratio of Pt active area to electrode geometric area. **Figure 4.34 d** also shows the empirical relationship between $R_{O_2}^{nF}$ and rf that is known to be valid for the cathode catalyst layers [84].

$$R_{O_2}^{nF} = R_{O_2,MPL}^{nF} + R_{O_2,CCL}^{nF} + \frac{R_{O_2}^{local}}{rf} = 0.053 + \frac{11.2}{rf} \quad \frac{sec}{cm} \qquad 4.2$$

In equation (4.2), $R_{O_2,MPL}^{nF}$ and $R_{O_2,CCL}^{nF}$ stand for non-Fickian MTR arising from the pores smaller than the mean free path of O_2 in the MPL and the cathode catalyst layer respectively. $R_{O_2}^{local}$ is the MTR at the local Pt-ionomer interface. Pant *et al.*[43] and Nonoyama *et al.*[44] experimentally measured $R_{O_2,MPL}^{nF}$ and $R_{O_2,CCL}^{nF}$ respectively, which add up to the roughness-independent 0.053 sec.cm^{-1} term in equation (4.2). For electrodes with lower roughness (ECSA), $R_{O_2}^{nF}$ increases according to equation (4.2).

From **Figure 4.34 c**, R_{total} at 150 kPa increased in the following order: 0.71 sec.cm^{-1} at BOL, 1.08 sec.cm^{-1} after 500 AST cycles, and 1.8 sec.cm^{-1} after 2000 AST cycles. A change in slope of the linear fit of R_{total} can be observed from BOL to 500 AST cycles and more significantly after 2000 AST cycles. Since carbon in the diffusion media did not corrode significantly, the change in the slope was due to the increase in overall MTR in the cathode catalyst layer. Collapse of the pore structure during the last 1500 AST cycles qualitatively explains this observation. **Figure 4.34 d** shows $R_{O_2}^{nF}$ for decreasing roughness of the cathode catalyst layer. **Figure 4.29 d** showed that ECSA, or equivalently, roughness decreased with ageing. **Figure 4.34 d** shows that up to 500 AST cycles, $R_{O_2}^{nF}$ varied according to equation (4.2). This implies that the change in $R_{O_2}^{nF}$, up to 500 AST cycles, can be approximately explained by decrease in the ECSA, without any significant pore structure collapse. However, after 2000 AST cycles, measured $R_{O_2}^{nF}$ (0.53 sec.cm^{-1}) was significantly higher than that predicted by equation (4.2) (0.3 sec.cm^{-1}). This result implies that the increase in $R_{O_2}^{nF}$ in the last 1500 AST cycles cannot be explained by the decrease in ECSA alone. Following the argument of previous modeling works [85,86], this originated from an increased $R_{O_2,CCL}^{nF}$ caused by severe collapse in the pore structure, which is also supported by the FIB-SEM data in **Figure 4.33**. This is perhaps the most direct electrochemical evidence of the pore structure collapse.

4.3.6. Impact of carbon corrosion on wettability of the cathode catalyst layer

Finally, to understand the impact of carbon corrosion on wettability of the cathode catalyst layer, surface chemistry and oxygen surface groups were studied by XPS Survey and high-resolution XPS spectra have been acquired from exposed catalyst layer locations at BOL, after 500, and 2000 AST cycles. The background corrected deconvoluted fine spectra for C1s region showing the relative abundance of different surface carbonaceous moieties are shown in **Figure 4.36** and the quantitative results are summarized in **Table 4.9**. The total concentration of carbonaceous surface oxides was 22.2% at BOL, 24.9% after 500 AST cycles, and 23.6% after 2000 AST cycles. The increase of relative concentration of COOH group, in particular, between 0 and 500 AST cycles was clearly observed. **Table 4.9**. also shows that percentage of individual C-F bonds decreased from 28.9% to 14.5% after 500 AST cycles and stayed constant around 17% after 2000 AST cycles. This could be explained as ionomer degradation in the cathode catalyst layer. From the C-C bond statistics, the relative abundance of graphitic carbon (signified by the relative content of the sp^2 hybridized moieties) increased after 500 AST cycles which can be interpreted as an effect of further oxidation, and hence a loss of amorphous carbon (usually derived from the relative content of the sp^3 hybridized moieties).

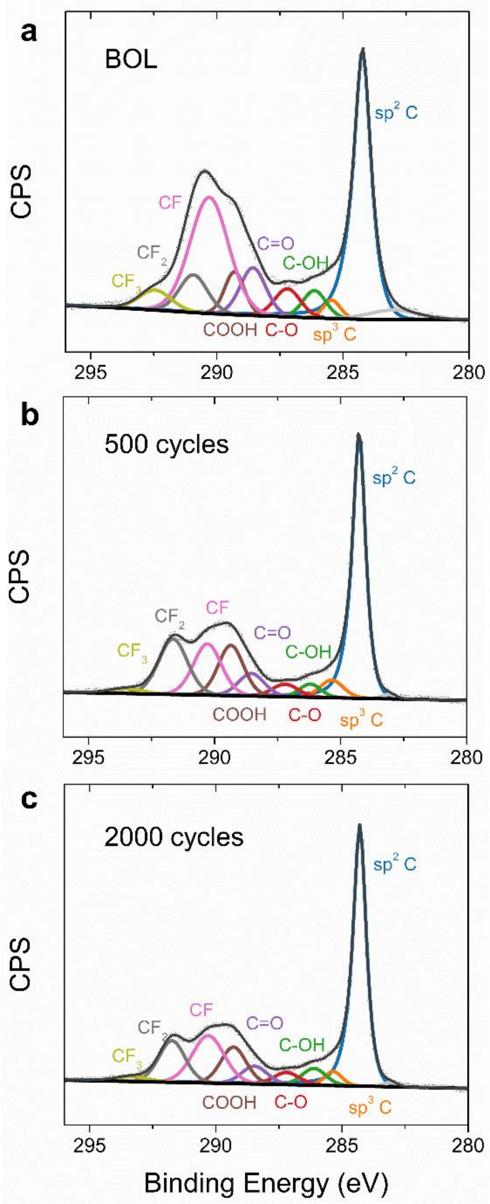

Figure 4.36 *a, At BOL b, after 500 AST cycles and c, after 2000 AST cycles.*

The total growth of surface carbonaceous oxides due to the AST was rendered statistically insignificant. This is consistent with the quantitative results by Macauley *et al*., where carbonaceous surface has been found to be effectively passivated by oxides around 0.8 V vs RHE [74]. Hence, application of AST (1-1.5 V) did not result in the any additional increase is surface oxides coverage, but rather advanced the terminal oxidation of predominantly amorphous carbonaceous domains to CO_2. Thus, even though the surface oxides did not increase significantly, the decreased overall porosity and the collapse of pore connectivity, have had a pronounced negative effect on water management in the cathode catalyst layer.

Table 4.9 *Relative concentrations for surface species at BOL, after 500 and 2000 AST cycles for carbon.*

Chemical species	Oxide groups on C					Fluorine signal (from ionomer binder)				C-C bonds		
AST stages	C-OH	C-O	C=O	COOH	total	C-F	C-F2	C-F3	Total	sp2	sp3	Total
BOL	4.1	4.7	7.9	5.5	22.2	28.9	6.9	4.2	40	32.9	2	34.9
500 AST cycles	2.8	3.3	5.9	12.9	24.9	14.5	16.1	1.7	32.3	38.1	4.2	42.3
2000 AST cycles	4.5	3.5	5.2	10.4	23.6	17	12.3	1.8	31.1	41.8	2.8	44.6

4.4. *Chapter 4:* Revealing in-plane movement of Platinum after heavy-duty lifetime

Recently, *in situ* identical location transmission electron microscopy (IL-TEM) and *ex situ* identical location scanning transmission electron microscopy (IL-STEM) techniques using aqueous electrolyte rotating disk electrode (RDE) setup have been utilized to elucidate electrocatalyst degradation mechanisms [75,87]. The more common IL-STEM uses a gold coated TEM grid which allows atomic level imaging, energy dispersive X-ray spectroscopy (EDS) and electron energy-loss spectroscopy (EELS) analysis of electrocatalyst in the same region at different lifetime stages. Combined results from both techniques have identified Pt dissolution as the primary and dominant ECSA loss mechanism followed by Pt nanoparticle size increase through migration-coalescence and Pt nanoparticle detachment from carbon support. Contrarily, MEA tests have shown that nanoparticle size increase by electrochemical Ostwald ripening is the dominant ECSA loss mechanism [8]. Such disparity is caused by the complicated cathode catalyst layer operation environment within MEA, where multiple transport processes at the electrocatalyst-support-ionomer interface play a crucial role [88]. In addition to electrocatalyst and ionomer properties, the transport processes are also affected by the operating conditions, PEFC components and cathode catalyst layer morphology [29]. This is also the reason for poor translation of electrocatalyst ORR activity from RDE to MEA-scale [88]. Furthermore, electrocatalyst degradation is strongly influenced by loading, and RDE working electrodes employ ultra-low electrocatalyst loading (ng.cm^{-2}) deposited on either carbon or gold surface compared to MEA-scale where a much higher loading is deposited on membrane. This can lead to degradation rates that deviate substantially from realistic conditions. Various studies have attempted to eliminate this disparity by using different electrolyte flowrates, operating temperatures and electrode configurations in the RDE setup [30,87]. However, concerns regarding the relevance of identified RDE-scale degradation mechanisms to MEA-scale remain. To date, MEA-scale AST studies commonly rely on *ex situ* TEM of scraped electrocatalyst from the cathode catalyst layer and SEM/EDS analysis of MEA cross-sections [31]. Although, this reveals nanoparticle size increase and through-plane changes like Pt band formation, the techniques fail to capture in-plane degradation phenomenon. Recently synchrotron µ-XRD studies revealed important in-plane heterogeneity in Pt nanoparticle size increase due to influence of operating conditions and PEFC components [28,29,52]. Thus, to mitigate the risk of misidentifying degradation mechanisms and misdirecting the electrocatalyst material development it is very important to validate the results with thorough MEA-scale analysis which captures realistic aspects of electrocatalyst degradation.

Thus, in this chapter commercially available CCMs from Gore® designed for HDV application were subjected to accelerated stress tests (ASTs) simulating HDV lifetime. A simple method was utilized to achieve for the first time MEA-scale identical location μ-XRF (IL-μ-XRF) spectroscopy maps before and after the AST. The IL-μ-XRF mapping of the MEA was performed in-plane near the inlet and outlet regions of the cathode gas flow field. Analysis of identical locations revealed distinct changes in Pt loading strongly influenced by its initial distribution and by cathode catalyst layer morphology. A modified cathode GDL MEA was used to highlight the effect of PEFC components on electrocatalyst degradation. The resulting heterogeneous Pt degradation was successfully quantified using the developed method. Finally, synchrotron μ-XRD and μ-XRF experiments were performed successively on identical locations to establish a currently unknown correlation between nanoparticle size increase and changes in loading after the AST. Electrochemical characterization was performed at various stages of the AST to support the spectroscopic analysis.

4.4.1. Electrochemical characterization data

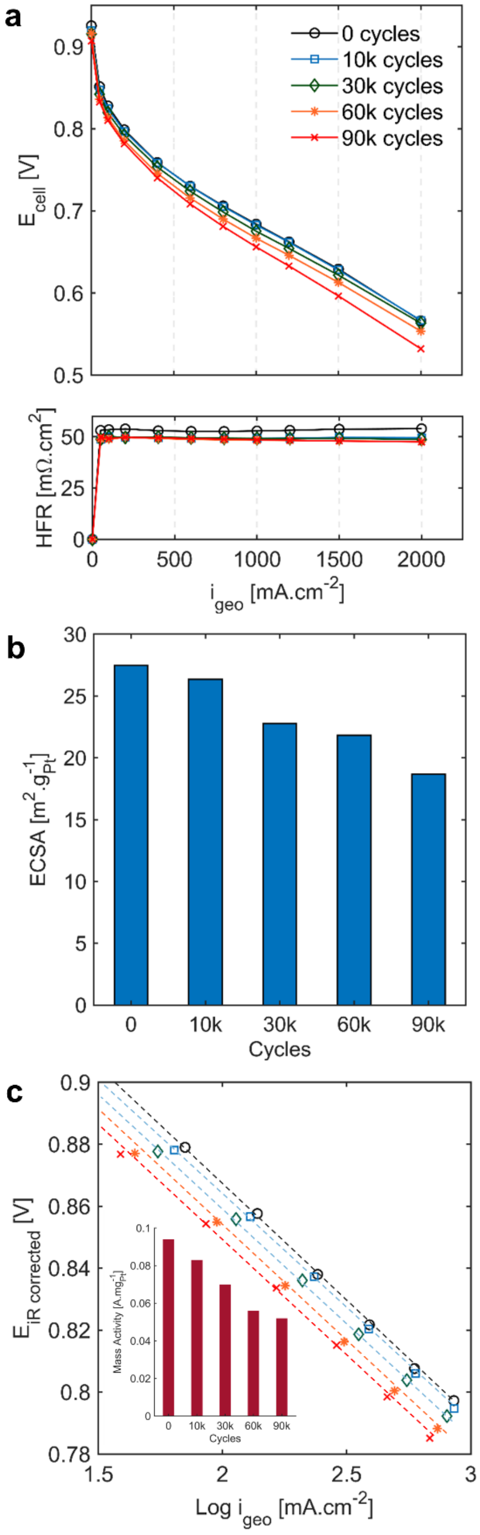

Figure 4.37 *a, Polarization curves with HFR collected at 80°C in 100% RH under 150 kPa of absolute backpressure in H_2-air differential environment. b, ECSA calculated from CVs collected at 80°C in 100% RH under 100 kPa of absolute*

backpressure in H_2-N_2 environment. c, Tafel plots generated from H_2-O_2 differential environment data collected at 80°C in 100% RH under 150 kPa of absolute backpressure. (Inset) Mass activity at 0.9 V calculated from the corresponding Tafel plots.

Polarization curves with high frequency resistance (HFR) collected at 80°C in 100% RH under 150 kPa of absolute backpressure in H_2-air (anode-cathode) differential conditions during various stages of the AST are plotted in **Figure 4.37 a**. Except a very small drop within first 10,000 AST cycles, the cell HFR remains unchanged throughout the AST. Such slight initial decrease in HFR has been previously reported [60] and is usually attributed to additional cell conditioning. As the AST progresses and the electrocatalyst undergoes degradation, a monotonic increase in kinetic and mass transport cell overpotentials can be observed. An overpotential increase of ~ 25 mV and ~ 33 mV is seen at geometric current densities of 0.8 $A.cm^{-2}$ and 1.5 $A.cm^{-2}$ respectively. Thus, the MEA achieved set DOE target of ≤ 30 mV of increase in overpotential at 0.8 $A.cm^{-2}$. A small change in the slope of polarization curves can be noticed between 60,000 and 90,000 AST cycles. As the HFR is constant, this change in slope could be due to increase in oxygen mass transport resistance usually caused by the decrease of Pt roughness factor (rf) below a threshold value [84]. **Figure 4.37 b** shows ECSA (calculated by integrating the hydrogen underpotential deposition region from cyclic voltammograms in **Figure 4.38** plotted at different stages of the AST. The ECSA decreased by ~ 32% after 90,000 AST cycles. The loss in ECSA agrees well with the observed increase in cell overpotentials. Tafel plots generated from data collected in operating conditions same as the polarization curves but in O_2 cathode environment are plotted in **Figure 4.37 c.** The Tafel slope is close to the theoretical ORR value[45] of 70 $mV.dec^{-1}$ and does not change through the AST. Plot inset **Figure 4.37 c** shows the mass activity at 0.9 V calculated from the Tafel plots. A ~ 45% decrease is observed in mass activity which follows a loss trend similar to the ECSA.

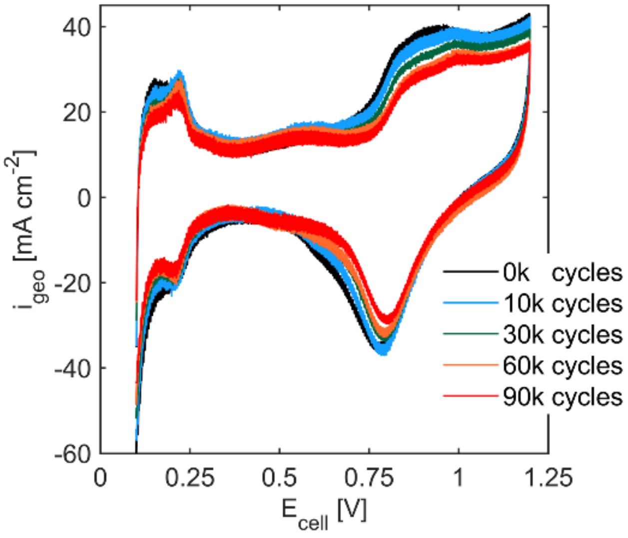

Figure 4.38 *Cyclic voltammograms collected at 80°C in 100% RH under 100 kPa of absolute backpressure in* H_2-N_2 *environment at different stages of the HDV AST.*

4.4.2. Identical location μ-X-ray fluorescence revealing in-plane Pt movement

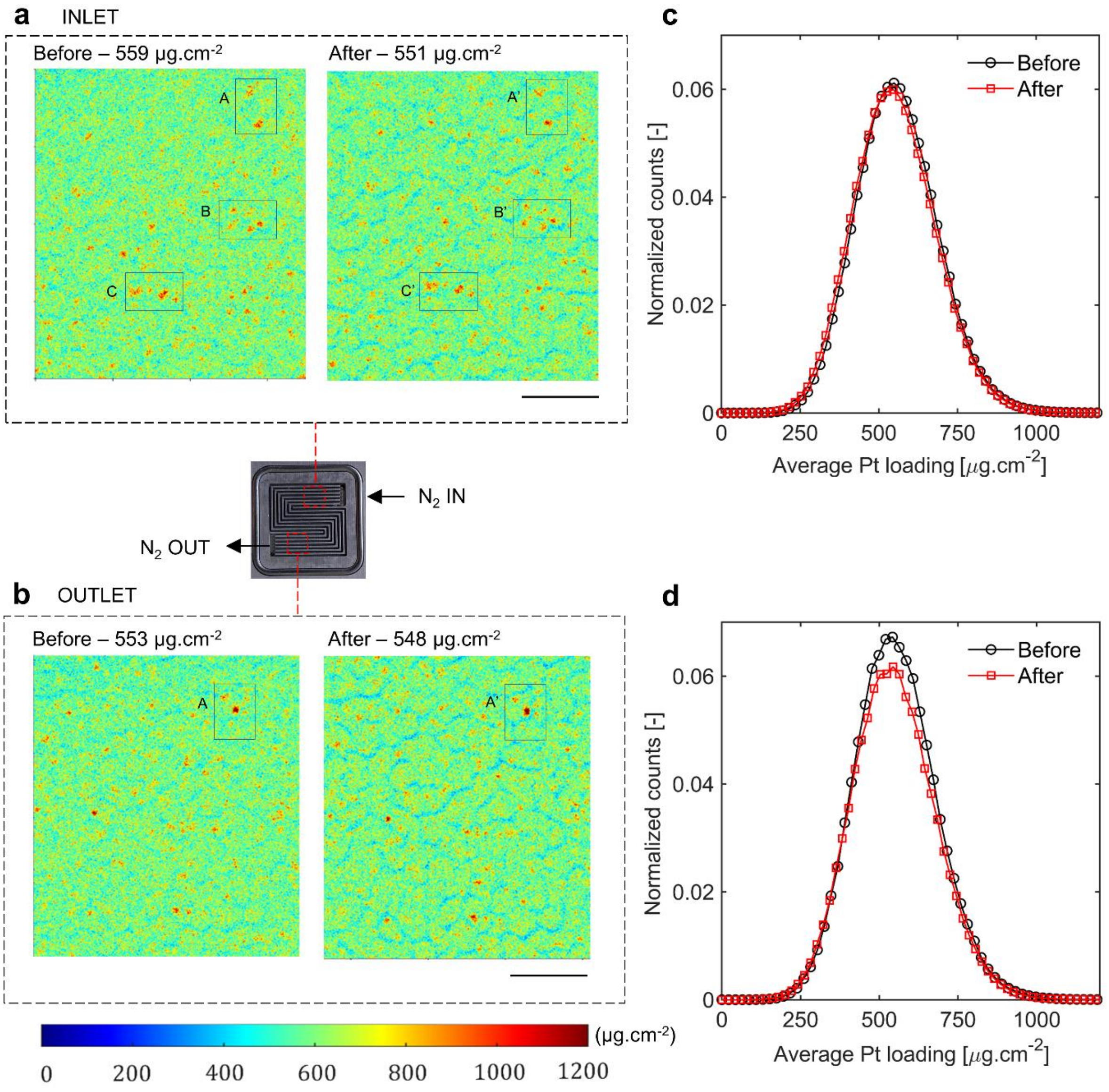

Figure 4.39 a, b In-plane Pt loading maps of inlet (a) and outlet (b) with regions marked to establish identical location before and after the HDV AST. c, d Corresponding histograms of the inlet and outlet respectively showing the unchanged unimodal Pt loading distribution before and after the HDV AST. Scale bars, 500 μm.

Using a thin PTFE template with alignment markers (section 3.6.5.), IL-μ-XRF spectroscopy was performed on MEA before and after HDV lifetime. The spectroscopy was performed in-plane on an area of 2048 μm by 2048 μm with a resolution of 2 μm by

2 µm near inlet and outlet of the serpentine cathode flow field. **Figure 4.39 a** and **b** show the 2D IL-µ-XRF maps near inlet and outlet respectively. Corresponding loading histograms are shown in **Figure 4.39 c** and **d**. Marked locations A,B,C in the inlet map before AST and A',B',C' after AST establish successful mapping of identical locations. Only one location is marked hereafter to signify identical location. A total average Pt loading of 559 µg.cm^{-2} was quantified in the before AST inlet map with presence of several local hotspots within initial distribution of Pt loading. The size of such local loading hotspots may differ, but it is a recurring feature found in various commercially available and in-house made CCMs fabricated using completely different techniques. One reason for development of such local loading hotspots is attributed to agglomeration of the carbon support influenced by solvent ratios, ionomer, drying conditions and dispersion methodology [89]. The before AST outlet map also shows features similar to the before AST inlet map with a total average Pt loading of 553 µg.cm^{-2} which falls within the observed spatial variation of ± 2% (section 3.6.5.). The after AST inlet and outlet maps show a total average Pt loading of 551 µg.cm^{-2} and 548 µg.cm^{-2} respectively. A clear increase in the intensity of local loading hotspots and development of cracks can be noticed in both the inlet and outlet after AST maps. However, a higher degree of cracking can be observed in the outlet map suggesting some heterogeneous degradation between inlet and outlet. The loading histograms of inlet and outlet before AST show a unimodal initial distribution of Pt loading. The distribution stays unimodal after the AST with a negligible change in the total average Pt loading as it falls within the observed spatial variation. A larger representative area of ~ 4 cm^2 out of the 5 cm^2 active area was also mapped with a resolution of 20 µm by 20 µm (**Figure 4.45** a). A total average Pt loading

of 559 μg.cm^{-2} and 550 μg.cm^{-2} was quantified for the 4 cm^{2} before and after AST maps respectively.

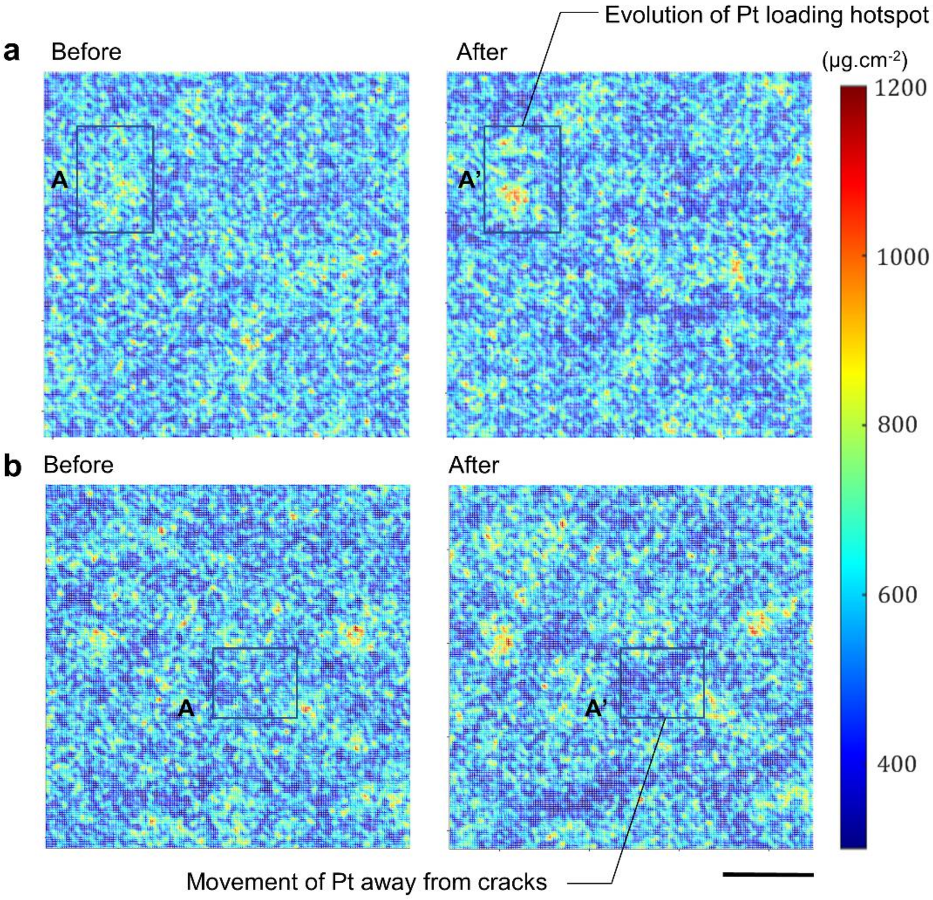

***Figure 4.40** a, b Local ~ 400 μm × 400 μm areas before and after the HDV AST from inlet (a) and outlet (b) IL-μ-XRF maps of the standard MEA. The marked regions highlight evolution of local loading hotspots and preferential movement of Pt loading away from cracks. Scale bar, 100 μm.*

To study the increase in intensity of local loading hotspots, IL-μ-XRF maps were closely examined before and after the AST. **Figure 4.40 a** shows one of the many (**Figure 4.41**) local 400 μm by 400 μm areas from inlet which delineates development of such local hotspots after AST. Marked locations A and A' in **Figure 4.40 a** clearly indicate in-plane movement of Pt which led to evolution of a hotspot where the average total Pt loading increased from ~ 750 μg.cm^{-2} to ~ 1100 μg.cm^{-2}. An average increase of ~ 32 % can be seen for formation of hotspots specifically observed in **Figure 4.40 a.** Such hotspots evolved selectively in locations with local loading already ≥ 750 μg.cm^{-2} confirming that initial Pt loading distribution plays a crucial role in how the Pt distribution will evolve during AST.

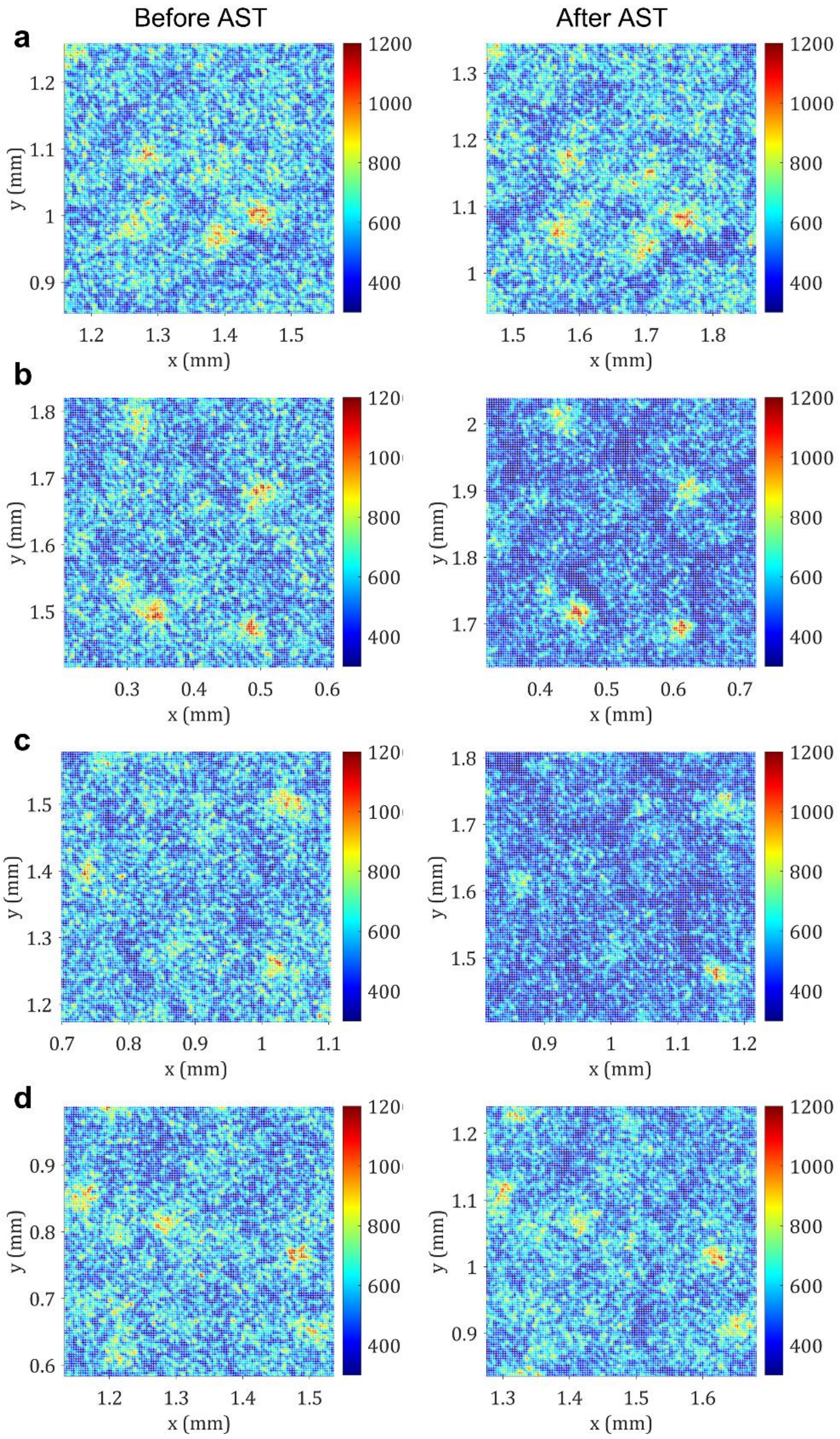

__Figure 4.41__ Various local ~ 400 µm × 400 µm areas from IL-µ-XRF maps of a, standard MEA outlet b,c modified MEA inlet and d, modified MEA outlet highlighting evolution of local loading hotspots and movement of Pt loading away from cracks after HDV AST.

Thus, formation of such hotspots could be driven by relatively low inter-nanoparticle distance in the initial stages followed by decrease in the local surface energy of the region later. The striking in-plane movement of Pt on the scale of tens of μm after AST may signify that electrochemical Ostwald ripening in the cathode catalyst layer is not a local effect as currently believed. **Figure 4.40 b** shows another local 400 μm by 400 μm area before and after AST from the outlet. Such maps also revealed a preferential movement of Pt away from the cracks making them more prominent after AST. The preferential movement of Pt could be thermodynamically driven due to difference between local surface energies of the regions. The transmission images (**Figure 4.42**) showed that cracks are present before AST and become more prominent after AST. Most likely, the cracks formed during the drying step of CCM fabrication and caused sparse distribution of Pt loading within. Different studies have reported that cracks result in low breakthrough pressure for removal of liquid water [90]. This can cause high liquid water flux in the cathode catalyst layer cracks consequently decreasing the local concentration of Pt ions. The sparse loading distribution within cracks (high surface energy) coupled with low local Pt ion concentration can intensify Pt degradation in and around cracks. The heavy in-plane movement of Pt along with the presence of loading hotspots within ~ 0 to 5 μm of a crack certainly substantiates the role of cathode catalyst layer morphology on Pt degradation. Cracks can also aid the through-plane movement of Pt ions either towards the membrane (via ionomer phase) or out of the cathode catalyst layer (via effluent water).

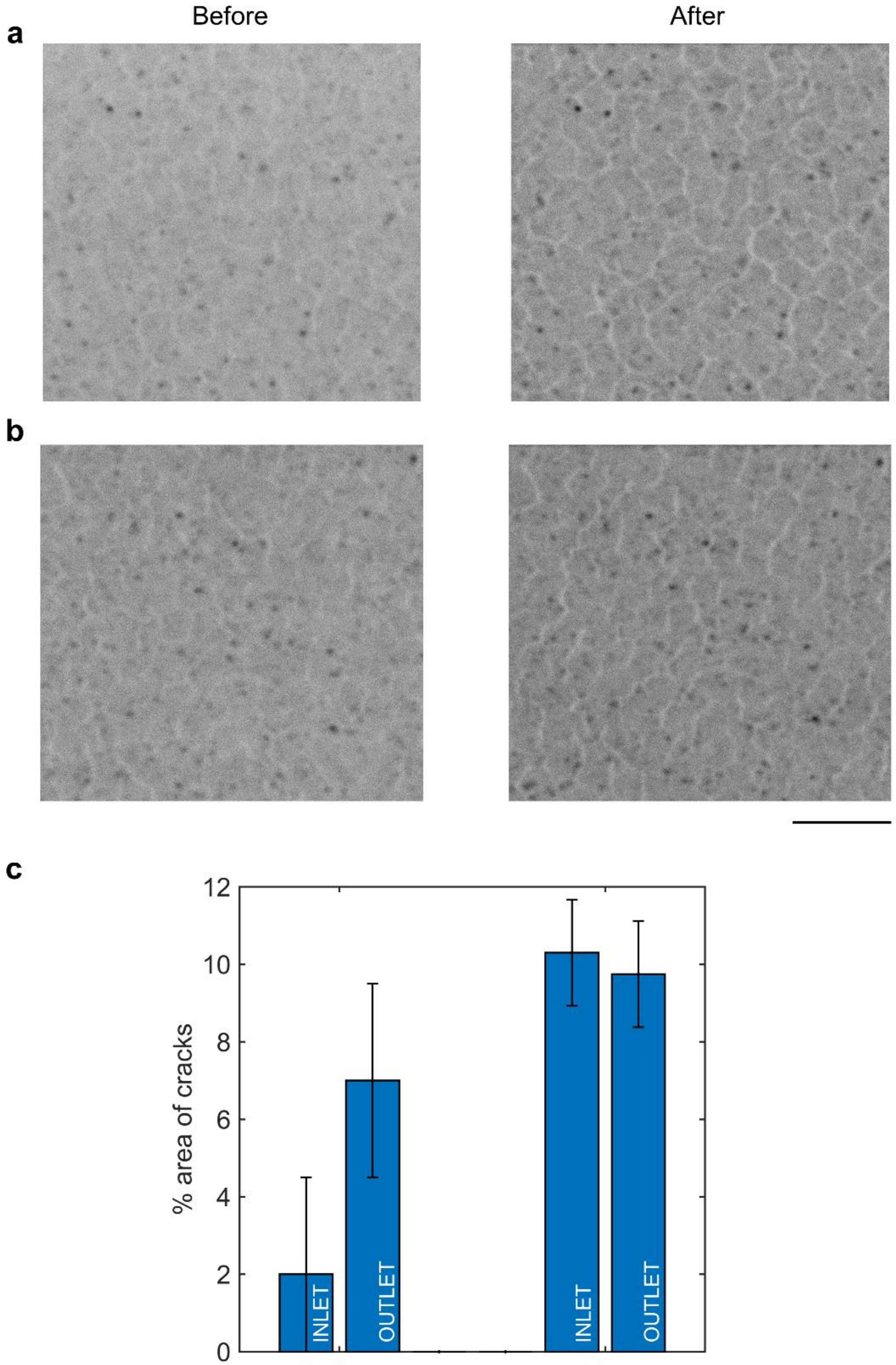

Figure 4.42 *Identical location transmission images of a, modified MEA inlet and b, modified MEA outlet before and after the HDV AST. c, Corresponding percentage area of cracks before and after AST. Scale bar, 500 µm.*

4.4.3. Effect of MPL cracks on Pt degradation

To understand if Pt degradation can be impacted by MEA components and to confirm if the developed identical location method could quantify such effects, a GDL with modified MPL was used on the cathode of MEA subjected to HDV lifetime. Cracks of width ~ 30-50 μm were milled in the MPL (section 3.1.) with a pitch of 1 mm in a direction perpendicular to the land/channels of the flow field and were confirmed by μ-XCT (**Figure 4.43**).

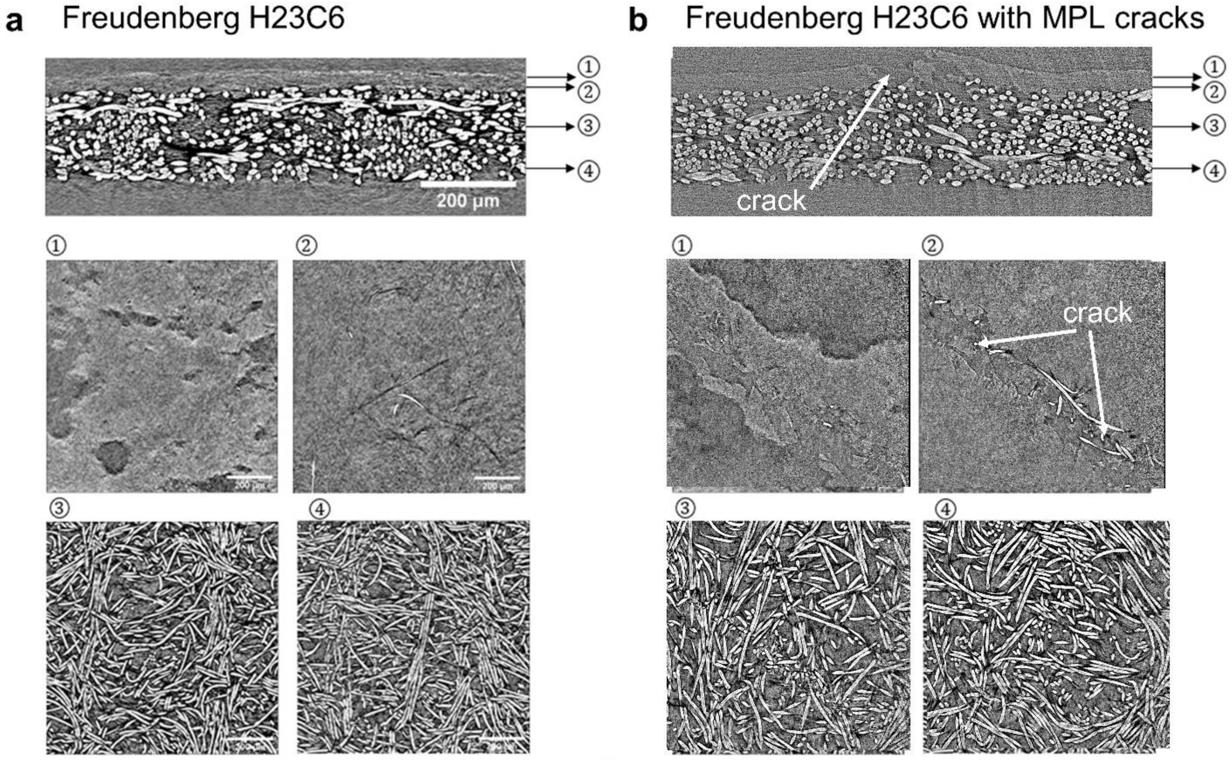

__Figure 4.43__ Through-plane (top) and in-plane (bottom) grayscale images from μ-XCT of a, Freudenberg H23C6 GDL and b, Freudenberg H23C6 GDL with ~ 20 μm wide cracks fabricated in the MPL.

Figure 4.44 a and **b** show IL-μ-XRF maps of modified MEA inlet and outlet (before and after AST) respectively. Like the standard MEA, significant in-plane movement of Pt loading with increase in the number of local loading hotspots can be observed between maps before and after AST of both inlet and outlet regions of the modified MEA. However, in contrast to the standard MEA a substantial heterogeneous degradation after AST was noted between the inlet and outlet. A loss in the total average Pt loading of inlet from 545 μg.cm^{-2} to 477 μg.cm^{-2} was effectively quantified before and after AST. This ~ 13% loss in the total average Pt loading is significantly higher than the observed ± 2 % spatial variation and ± 2% variation due to attenuation (section 3.6.5.). Thus, it may be assigned to the loss of Pt ions out of the mapped area. To understand if this loss from the mapped area was not due to Pt redistribution to the other parts of the active area caused by an in-plane movement of Pt, 4 cm^2 out of the 5 cm^2 active area was also mapped (**Figure 4.45 b**). A similar trend of decrease in average total Pt loading from 558 μg.cm^{-2} to 498 μg.cm^{-2} was quantified equating to ~ 10 %. Thus, the heterogeneous degradation resolves the small ~ 3% drop observed in the loss of total average Pt loading between the large 4 cm^2 and local inlet area. On the other hand, the total average Pt loading of the outlet was 547 μg.cm^{-2} and 535 μg.cm^{-2} before and after AST, respectively. The decrease was negligible compared to the inlet and fell quite close to the observed spatial variation confirming heterogeneous degradation between the inlet and outlet was caused by the modified GDL. A remarkably high crack development can be observed for inlet after AST with modified GDL explaining the ~ 13% loss in total average Pt loading. The crack formation for the outlet is close to that observed within standard MEA after AST, all of which show minimal change in the total average Pt loading. This further elucidates the role of cracks in through-plane and in-plane transport of Pt ions **Figure 4.44 c** and **d** show inlet and outlet loading histograms for the modified MEA respectively. The initial unimodal distribution stays same after the AST for both however, histogram for inlet after the AST shifts left owing to the observed loss in total average Pt loading. The identical location approach allowed successful quantification of evolution of cracks, inlet-outlet degradation heterogeneity and the effect of MEA components on electrocatalyst degradation. Although out of scope for this study, it must be noted that observed loss of Pt loading can be corroborated by ICP-MS of effluent water.

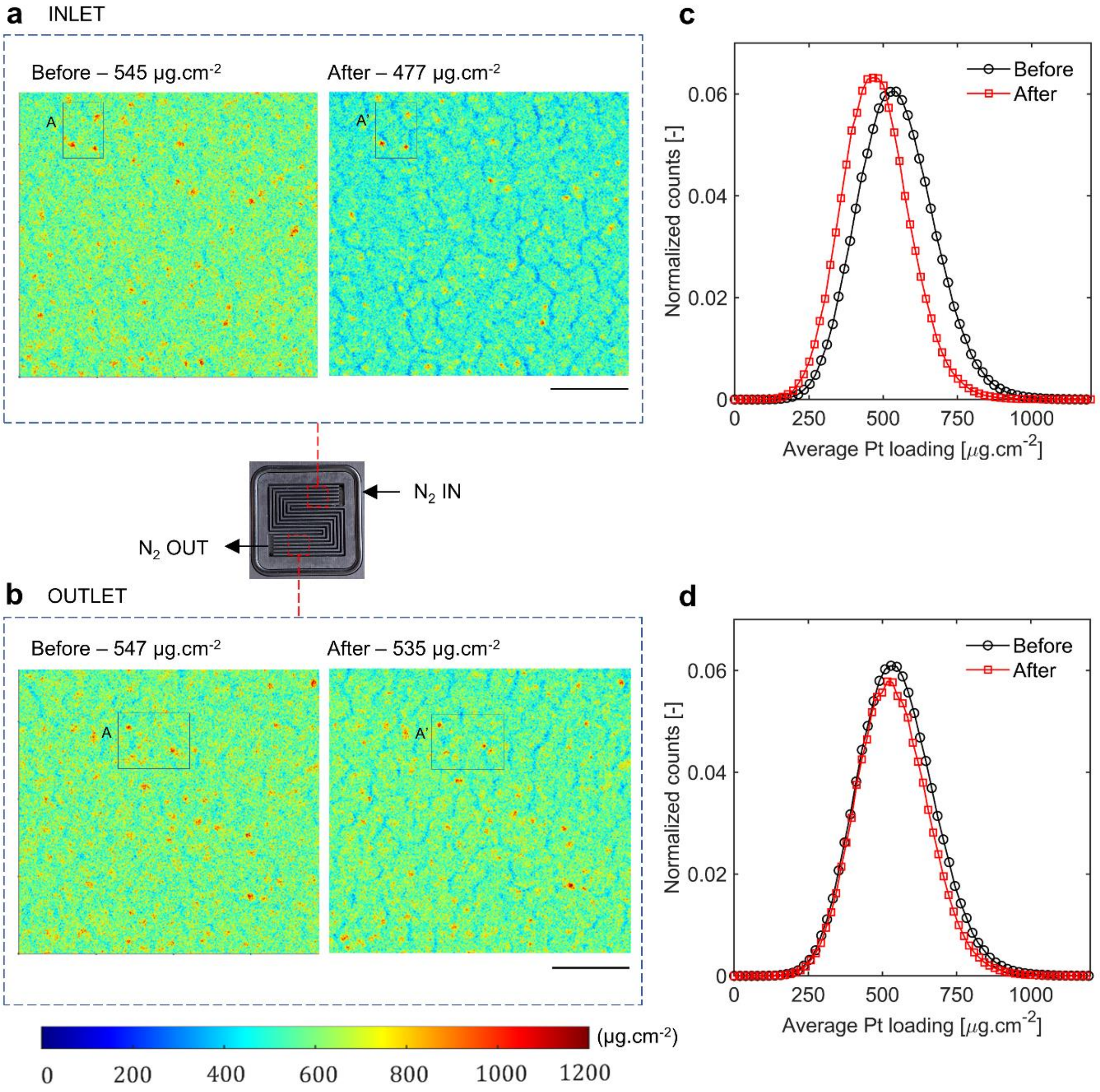

Figure 4.44 *a, b In-plane Pt loading maps of inlet (a) and outlet (b) before and after the HDV AST. c, d Corresponding Pt loading distribution histograms of the inlet and outlet respectively. The unimodal distribution was unchanged before and after the HDV AST however a loss in inlet average total Pt loading was observed. Scale bars, 500 µm.*

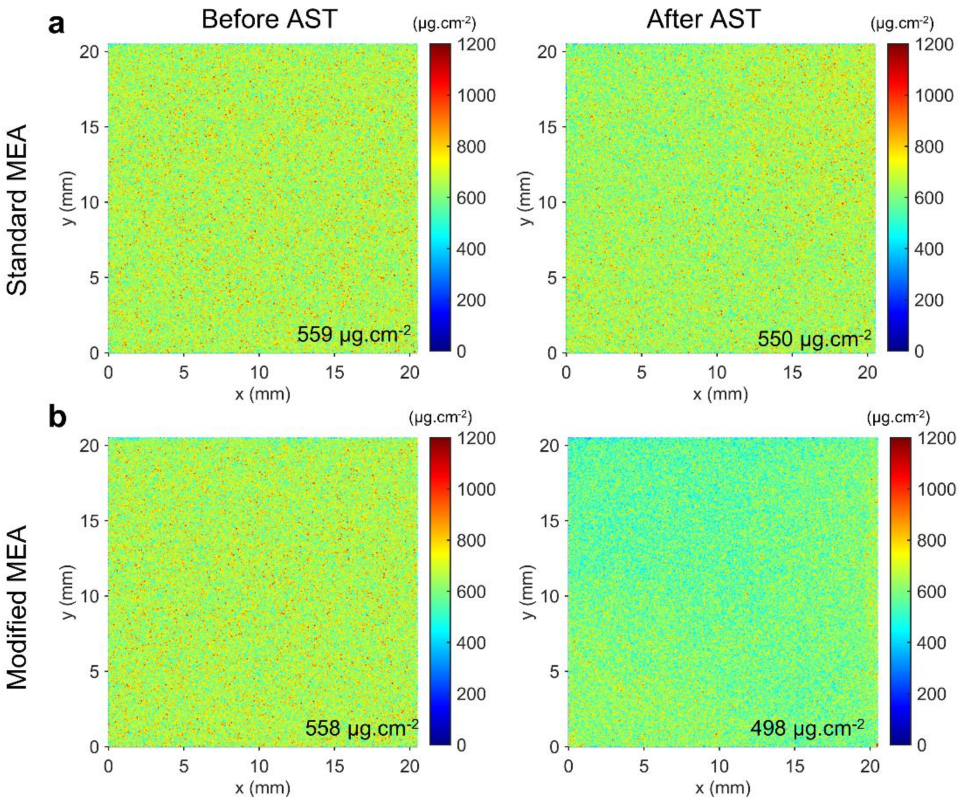

Figure 4.45 *Representative 20.48 mm × 20.48 mm μ-XRF mapped area (~ 4 cm^2 out of the 5 cm^2 active area) for the a, standard MEA and b, modified MEA before and after the HDV AST. Corresponding quantified average total Pt loading reported in the bottom right of each map.*

Compared to the standard MEA, modified MEA (**Figure 4.46**) before AST showed identical overpotentials in the kinetic and ohmic regions. Higher cell overpotentials observed in the mass transport region were most likely due to the MPL modification. After AST, cell overpotentials increased more for the modified MEA in all regions driven by relatively high Pt degradation. Cell overpotential increase of 33 mV at 0.8 A.cm^{-2}, 54 % loss in mass activity at 0.9 V and 41 % loss in ECSA was observed after AST for the modified MEA. Interestingly, after AST the H_2 crossover saw an increase of 16% for the modified MEA indicating increased membrane degradation by combination of cathode catalyst layer and MPL cracks.

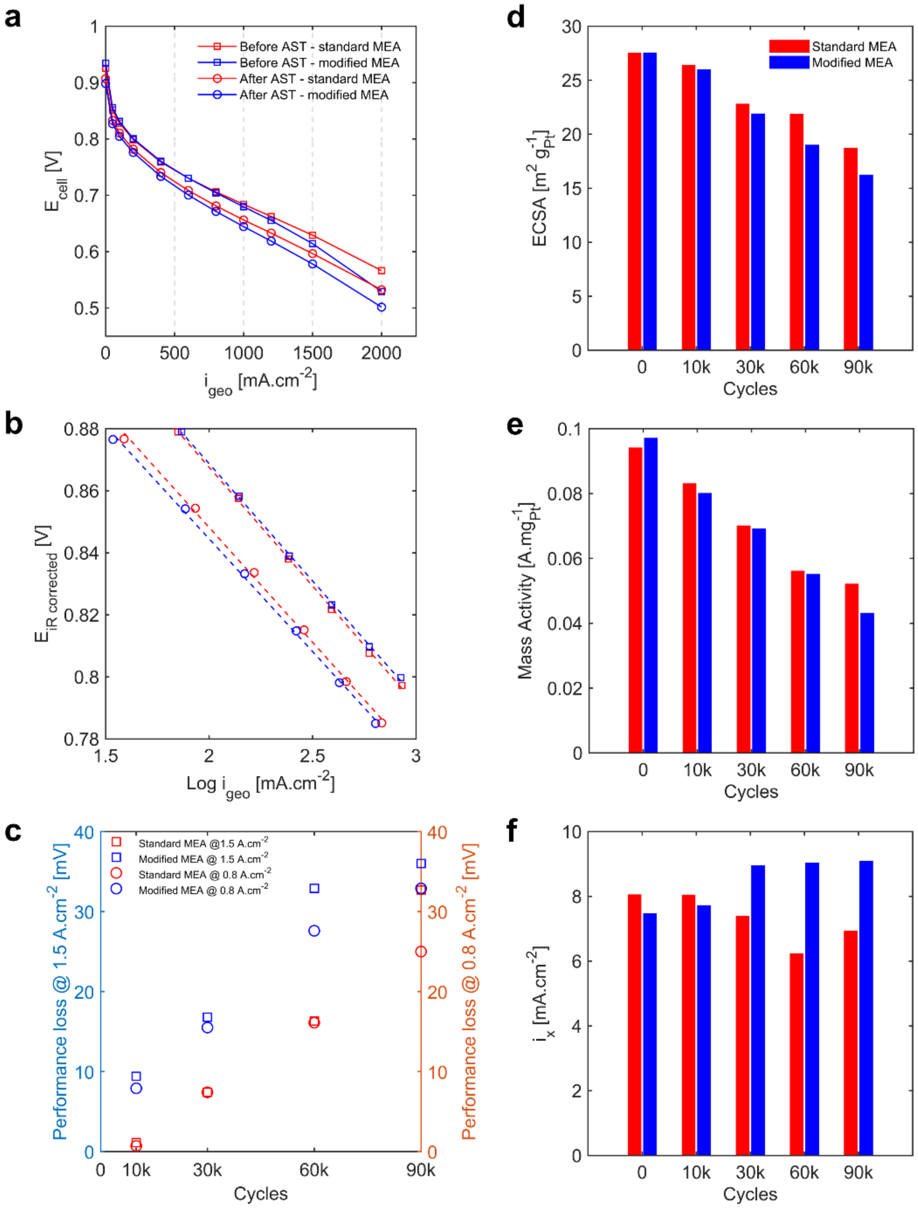

Figure 4.46 *a, Polarization curves and b, Tafel plots of standard and modified MEAs before and after the HDV AST. c, Comparison of cell overpotential increase at 0.8 A.cm^{-2} and 1.5 A.cm^{-2} d, ECSA e, mass activity at 0.9 V and f, crossover current density between standard and modified MEA at various stages of the HDV AST.*

4.4.4. Correlation between Pt nanoparticle size and loading

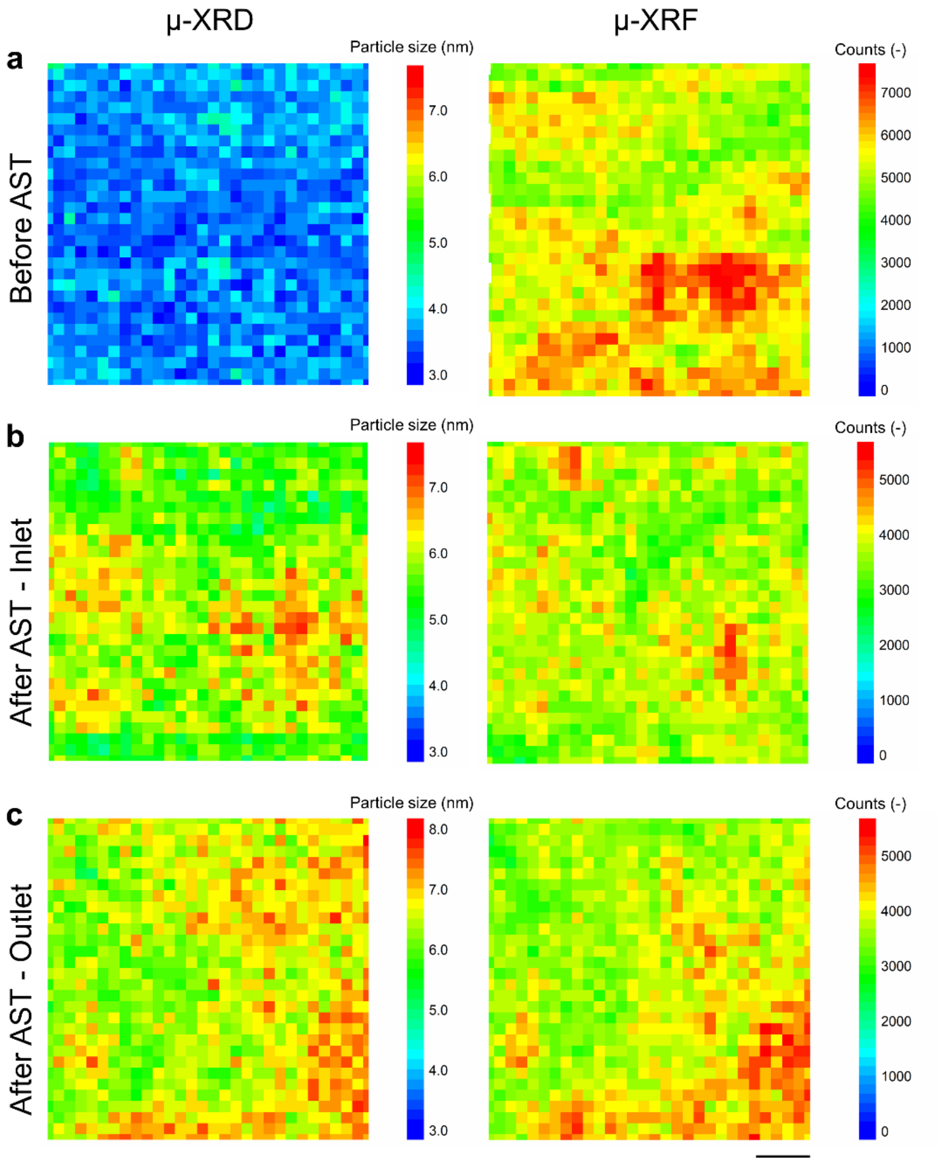

***Figure 4.47** a, Before HDV AST 300 µm × 300 µm maps showing no correlation between Pt nanoparticle size and loading distribution. b, c Inlet and outlet of the standard MEA respectively showing a strong linear correlation between Pt nanoparticle size and loading distribution after AST. Scale bar 50 µm.*

Figure 4.47 a, **b** and **c** show 300 µm by 300 µm synchrotron µ-XRD maps of CCM before AST, inlet-after AST and outlet-after AST respectively along with µ-XRF maps of the same location (section 3.6.5.). No correlation can be observed between Pt nanoparticle size and loading distribution for the CCM before AST. The average Pt nanoparticle size before AST is 3.63 nm with a Pearson's correlation of – 0.07 between the 2D maps of nanoparticle size and loading (**Table 4.10**). A Pearson's correlation of 0 means no linear relationship while a correlation of -1 or +1 indicates complete linear relationship between two maps. The inlet and outlet after AST show a direct linear correlation (positive correlation) between the Pt nanoparticle size and loading with a Pearson's correlation of +0.37 and +0.33, respectively. This means that increase in Pt nanoparticle size is driven by the local increase in Pt loading. The average inlet and outlet Pt nanoparticle size increased to 5.80 nm and 6.84 nm, respectively. Some local hotspots in the μ-XRD maps show a nanoparticle size increase of almost 8 nm after AST. The synchrotron μ-XRD and μ-XRF maps of the modified MEA (**Figure 4.48**) also show direct linear correlation with a Pearson's correlation of +0.42 for inlet. More interestingly, the average inlet Pt nanoparticle size increased to 6.76 nm even after ~ 13% loss in the total average Pt loading was quantified from the IL-μ-XRF after AST. Thus, coupled with the established correlation above, for a μm scale region in the cathode catalyst layer undergoing degradation, Pt nanoparticle size increase and loss in loading are mutually inclusive. This finding is extremely important as it provides blueprint to prevent the depletion of Pt near the membrane-cathode interface in the through-plane direction by developing a hybrid cathode catalyst layer structure with targeted low surface energy regions.

***Table 4.10** Pearson's correlation between the Pt nanoparticle size (μ-XRD) and Pt loading (μ-XRF) for various locations of standard and modified MEA before and after the HDV AST.*

	Pearson's correlation
Pristine - before AST	-0.07
Standard MEA inlet - after AST	+0.37
Standard MEA outlet - after AST	+0.33
Modified MEA inlet – after AST	+0.42

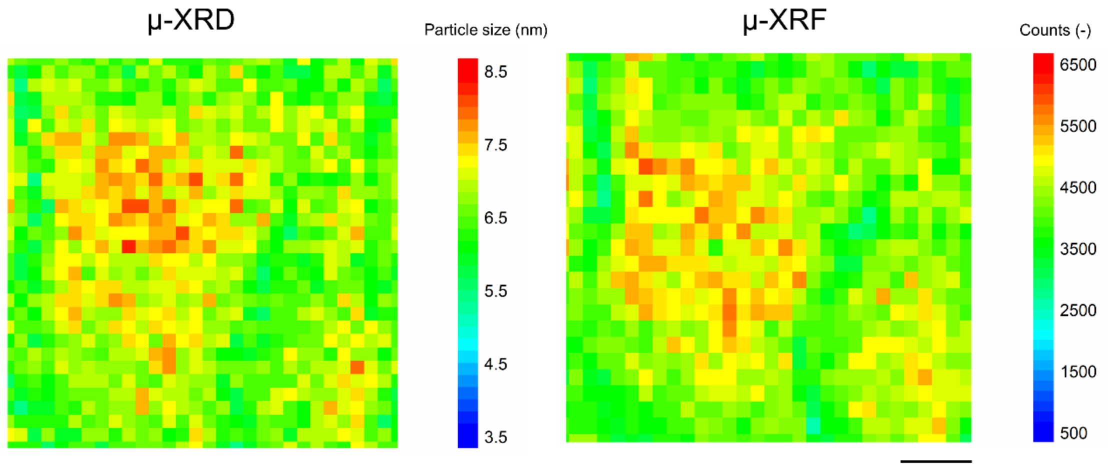

Figure 4.48 *Synchrotron μ-XRD and μ-XRF maps of modified MEA inlet after HDV AST. Scale bar, 50 μm.*

5. Conclusions

5.1. Effect of operating conditions and flow field geometry on catalyst degradation

Four MEAs were tested under different RH and gas environments using standard DOE AST protocols (voltage cycling from 0.6 V to 0.95 V/OCP for 30,000 cycles) and investigated for heterogeneous catalyst degradation. The ASTs conducted were under 40 % or 100 % RH and in H_2/Air or H_2/N_2 environment, termed here as Air Dry, Air Wet or N_2 Dry and N_2 Wet. For H_2/Air experiments the UPL during AST was limited by the cell OCP. The effect of flow field land and channel was further investigated using the US DRIVE FCTT adopted AST protocols. A combination of electrochemical characterization and post-mortem characterization techniques (SEM/EDS, μ-XRD, μ-XCT, μ-XRF and XPS) is used to unravel the heterogeneity of Pt degradation at inlet/outlet and land/channel locations.

Polarization curves showed potential loss in all the regions: activation, ohmic and mass-transport from 1,000 cycles to 30,000 cycles. Cyclic voltammetry plots showed that different Pt facets disappear at different rates (Pt (110) had highest dissolution rate) in the H_{UPD} region during cycling. Largest ECSA loss was observed for N_2 Wet, then Air Wet, N_2 Dry and Air Dry operating conditions (wet - 100% RH dry- 40% RH). Tafel slopes were calculated from potential loss at BOL and during ageing vs. log ($ECSA_{ratio}$) at 100 $mAcm^{-2}$ indicating that the loss in polarization for MEAs in wet conditions is mainly due to ECSA loss (~70mV dec^{-1} Tafel slope), whereas for dry conditions there are additional losses in polarization that cannot be explained by the ECSA loss alone.

Cross-sectional SEM, X-ray CT and EDS showed that the catalyst layer thickness remained approximately unchanged during ageing. Optical imaging and μ-XCT showed that catalyst layers have woven structure. Micro XRD corroborated the ECSA loss, showing largest Pt particle size (~14 nm) for N_2 Wet AST, second largest for Air Wet AST (~7 nm) and smaller for N_2 and Air Dry AST (~4-5 nm). The difference in absolute mean Pt particle size at the EOL between N_2 and air environment is due to the difference in the UPL during voltage cycling. UPL for air environment AST is OCP, which decreases during cycling, reducing PtO coverage and decreasing Pt dissolution rate during cathodic voltage sweep. Heterogeneity of catalyst degradation under land and channel is prominent in Air Wet AST due to produced water mostly at the LPL (~0.6 V), which exacerbates the difference in thermal management of land and channel. Higher water content in catalyst layer under land increases PtO coverage and subsequently promotes Pt ion formation and mobility. Co-flow configuration of humidified gases cause water accumulation in the outlet region, which leads to heterogeneous particle size growth between inlet and outlet.

The XPS study showed that relative Pt^0 atomic concentration increased in a sequence N_2 Wet, Air Wet, Dry ASTs and Control. Higher metallic Pt content is due to larger nanoparticle size, as Pt^0 is located inside the nanoparticle. The μ-XRF analysis confirmed that Pt nanoparticle size growth is a local phenomenon, as Pt loading does not follow a land-channel pattern. The analysis also confirms loss of Pt from the cathode catalyst layer.

For durable operation of PEFC under dynamic load and homogeneous catalyst degradation it is desirable to minimize the land area to reduce relatively cold locations (under land) in the catalyst layer. Flow-field with 0.5 mm width lands showed homogeneous catalyst degradation with no Pt nanoparticle size differences due to land-channel geometry. Furthermore, operating in a counter-flow or using alternative gas flow-field configuration can help reduce inlet-outlet degradation heterogeneity. Lastly, designing a dynamic load cycle with lower UPL by using system level control can reduce Pt nanoparticle size growth due to Ostwald ripening. Overall, for improved catalyst layer durability it is desirable to operate at sub humidified conditions due to reduced Pt ion migration in ionomer, which is a function of water content. Thus, higher temperature operation can help keep lower relative humidity in the stack but at the same time may contribute to other component (non-catalyst) degradation, therefore, careful optimization is needed.

5.2. Effect of gas diffusion layer water management on catalyst degradation

Catalyst ASTs were performed on MEAs using commercially available GDLs Sigracet 22BB, Freudenberg H23C6 and AvCarb MB30 in both nitrogen and air environments.

Micro X-ray computed tomography was performed on each GDL to analyze differences in morphological properties such as thickness, porosity, pore size distribution and to also identify critical features. Thorough in-situ electrochemical characterization was performed at various stages of the ASTs to better understand the degradation phenomena. µ-XRD mapping was used to analyze increase in average Pt nanoparticle size while µ-XRF mapping was used to quantify average Pt loading after ASTs. Computational fluid dynamic simulations using Lattice Boltzmann method were performed on water injection µ-XCT data collected for each GDL to understand liquid water saturation/flux and breakthrough pressure.

From µ-XCT, the embedded nature of MPLs in 22BB and MB30 was detected while H23C6 showed a free standing MPL. MPL thicknesses of 74 ± 7 µm, 35 ± 3 µm and 41 ± 9 µm were observed for 22BB, H23C6 and MB30, respectively. MPL of 22BB showed cracks, which resulted in better water management confirmed by slightly better electrochemical performance in the mass transport region. The cracks provided a direct pathway for removal of liquid water from the cathode catalyst layer. An ECSA loss of 78% and 60% was observed after nitrogen and air ASTs respectively for each MEA. A voltage loss of 100 mV (DOE target 40 mV) was observed in the air polarization curves after the nitrogen ASTs of each GDL. Close to 50% of initial ECSA and 47% of initial mass activity was lost within the first 5000 AST cycles by all the MEAs. Although some differences were observed in the mass transport region before and after AST (due to significantly different GDL morphologies), no difference was observed in electrocatalyst degradation (arising due to differences in GDLs) from electrochemical performance. µ-XRD maps showed an increase in the average Pt nanoparticle size for all GDL MEAs, which correlate with the

ECSA loss data. The MEA with 22BB as cathode GDL showed a much higher degree of heterogeneous Pt nanoparticle size growth with a lower average Pt nanoparticle size after nitrogen AST. µ-XRF maps also showed almost 16% of average Pt loading loss for 22BB compared to 6-7% average Pt loading loss for H23C6 and MB30.

CFD simulations using LBM showed that 22BB had the lowest breakthrough (8.5 kPa) and stagnation pressure (3.7 kPa) coupled with the highest (24%) liquid water saturation compared to H23C6 and MB30. A combined analysis of micro XCT, micro XRD, micro XRF and CFD simulation suggests that higher liquid water flux due to presence of MPL cracks in 22BB results in more direct loss of dissolved Pt ions from the cathode catalyst layer. This also suggests that different pathways were taken by the three GDL MEAs to reach similar ECSA loss.

Although the electrochemical difference cannot be observed for 30,000 AST cycles (LDV lifetime) it may show up after 90,000 AST cycles (to simulate HDV lifetime) and in dry operating conditions. The direct loss of dissolved Pt from the system is also critical in terms of Pt recycling. The study highlights the importance of designing GDLs with end-of-life performance target.

5.3. Chronology of catalyst layer pore structure collapse due to carbon corrosion

Commercially available PEFC MEAs were subjected to the DOE adopted carbon corrosion AST. The morphological changes that occurred after carbon corrosion were studied using spectroscopic and electron microscopy techniques and the results were correlated with the electrochemical performance. The corrosion showed two phases: in the initial phase (~ 500 cycles), carbon corroded rapidly (about 78% of the total loss) and the cathode catalyst layer lost thickness fast (~ 78% of the total reduction). Pt detached from the support as the latter corroded, and ECSA dropped sharply (~ 90% of the total loss). The sheet capacitance (~ 95% of the total reduction) and resistance of the cathode catalyst layer decreased significantly too. Due to the loss of electrical contact, Ohmic resistance increased slightly. However, no significant change in the pore structure was observed. The increase in O_2 mass transport resistance was primarily due to the loss of ECSA. In the later phase (~ 1500 cycles), carbon corrosion, ECSA loss, cathode catalyst layer thinning, and sheet capacitance reduction slowed down significantly. However, a drastic collapse occurred in the cathode catalyst layer pore structure. Porosity (~ 75% of the total reduction) and pore connectivity ($>$ 80% of the total) decreased considerably. This resulted in a significant increase of O_2 mass transport resistance (65% of the total increase). Tafel slope was found to increase from 71 $mV.dec^{-1}$ to 106.8 $mV.dec^{-1}$ with ageing. It was an apparent effect due to increasing mass transport resistance. The AST did not result in any significant growth of oxides, but the overall water management of the cathode catalyst layer might have deteriorated due to the loss of porosity and pore connectivity.

5.4. Identical location µ-X-ray fluorescence mapping after heavy-duty vehicle lifetime

Commercial CCMs designed for HDV applications were subjected to AST simulating HDV lifetime. A simple approach was used to facilitate IL-µ-XRF spectroscopy of MEAs before and after the AST. The novel results revealed striking in-plane movement of Pt loading strongly influenced by the initial loading distribution. Increase in the intensity and evolution of local loading hotspots with preferential movement of Pt loading away from the cathode catalyst layer cracks was observed and successfully quantified. A GDL with cracked MPL was used on the cathode to understand the effect of PEFC components on Pt degradation. The identical location approach exposed heterogeneous degradation between inlet-outlet and allowed quantification of ~ 13% loss in total average Pt loading for the inlet after AST. Synchrotron μ-XRD and μ-XRF experiments showed a direct linear correlation between Pt nanoparticle size and loading, which developed only after AST. The increase in average Pt nanoparticle size to 6.76 nm for modified MEA inlet even after ~ 13% loss in total average Pt loading suggested that nanoparticle size increase and loading loss are mutually inclusive for a cathode catalyst layer area undergoing degradation.

6. Future work

6.1. Materials development to enhance durability of PEFCs

6.1.1. Modification of catalyst interface

Dissolution of Pt ions during reduction of oxide is the primary catalyst degradation mechanism. Thus, delaying the onset of oxide formation to potentials greater than 0.9 V could be a viable strategy to improve long term ORR catalyst material durability. Based on initial reports at RDE scale, this may be done by addition of small molecule additives (to modify the catalyst-ionomer interface) such as poly-melamine formaldehyde (PMF) and ionic liquids (ILs.) Such small molecule additives can also boost the catalyst specific activity. Pt nanoparticles doped with transition metals such as Cobalt and Nickel are highly active ORR catalysts and promising candidates for commercial use. However, they suffer significant degradation due to transition metal leaching affecting the activity followed by ionomer conductivity and permeability. Small molecule additives also have the potential to prevent such leaching of transition metals. Efforts will be required to optimize the catalyst-ionomer-additive interface in the catalyst layer at MEA scale through use of different solvents and solvent ratios.

6.1.2. Use of carbon support morphology

A strong interaction of catalyst nanoparticles with the carbon support in addition with narrow distribution of nanoparticle size can help alleviate degradation caused due to agglomeration and coalescence. This can be achieved by utilizing carbon support morphology to create physical barriers for pathways of agglomeration and coalescence. For instance, a highly microporous (2 nm) metal-organic framework-based carbon support can be used to limit Pt nanoparticle size growth. This can be done by deposition of nanoparticles inside micro and relevant mesopores (3 to 4 nm) which can also create a significant physical separation and prevent degradation through migration and coalescence.

6.2. Engineered catalyst layers to reduce PEFC degradation

6.2.1. Hybrid loading catalyst layers

An approach of targeted low surface energy regions with hybrid loading of catalyst in both in-plane and through plane directions of the catalyst layer where exacerbated degradation is observed can be used to increase the durability. For instance, a layer of just carbon and ionomer in between the PEM and catalyst layer may prevent Pt band formation and catalyst depletion. Similarly, higher loading in degradation prone regions (such as inlet) can be used to eliminate heterogenous degradation.

6.2.2. Carbon-free catalyst layers

A way to improve carbon corrosion durability would be to completely eliminate carbon from the catalyst layer. Use of catalyst thin films to do this is promising however quite challenging. Such catalyst layers can also be used as corrosion tolerant anodes to prevent degradation from fuel starvation.

6.3. System-level mitigation strategies to increase PEFC lifetime

Limiting upper potential limit, operation under low relative humidity conditions and optimized flow field geometry are critical system-level mitigation strategies to significantly reduce degradation. Innovative ways to limit UPL will be necessary without causing thermal management issues until material durability improves. Also, it will be important to consider its effects on other PEFC components (such as PEM) and overall system efficiency.

References

[1] World Energy Outlook 2021. Int Energy Agency 2021:15.

[2] Perea A, Smith C, Davis M, Sun X, White B, Cox M, et al. U . S . Solar Market Insight Executive Summary 2020:28.

[3] Saeedmanesh A, Mac Kinnon MA, Brouwer J. Hydrogen is essential for sustainability. Curr Opin Electrochem 2018;12:166–81. https://doi.org/10.1016/j.coelec.2018.11.009.

[4] Mark F. Ruth, Paige Jadun, Nicholas Gilroy, Connelly E, Boardman R, Simon AJ, Zuboy AE and J. The Technical and Economic Potential of the H2@Scale Hydrogen Concept within the United States 2020:196.

[5] Hydrogen Shot: An Introduction 2022:2362.

[6] Table 2-8 Inventory of U.S. Greenhouse Gas Emissions and Sinks, 1990 to 2020 2020.

[7] Anair D. Engines for Change 2015.

[8] Borup R, Meyers J, Pivovar B, Kim YS, Mukundan R, Garland N, et al. Scientific aspects of polymer electrolyte fuel cell durability and degradation. Chem Rev 2007;107:3904–51. https://doi.org/10.1021/cr050182l.

[9] Papageorgopoulos D. Fuel Cell R&D Overview. 2019 Annu Merit Rev Peer Eval Meet 2019:33.

[10] Cullen DA, Neyerlin KC, Ahluwalia RK, Mukundan R, More KL, Borup RL, et al. New roads and challenges for fuel cells in heavy-duty transportation. Nat Energy 2021;6:462–74. https://doi.org/10.1038/s41560-021-00775-z.

[11] Meier JC, Galeano C, Katsounaros I, Witte J, Bongard HJ, Topalov AA, et al. Design criteria for stable Pt/C fuel cell catalysts. Beilstein J Nanotechnol 2014;5:44–67. https://doi.org/10.3762/bjnano.5.5.

[12] Yu H, Zachman MJ, Reeves KS, Park JH, Kariuki NN, Hu L, et al. Tracking Nanoparticle Degradation across 2022. https://doi.org/10.1021/acsnano.2c02307.

[13] Lee C, Wang X, Peng J-K, Katzenberg A, Ahluwalia R, Kusoglu A, et al. Towards a Comprehensive Understanding of Cation Effects in Proton Exchange Membrane Fuel Cells. ACS Appl Mater Interfaces 2022:Accepted. https://doi.org/10.1021/acsami.2c07085.

[14] 2019 AEO. Annual Energy Outlook 2019 with projections to 2050. Annu Energy Outlook 2019 with Proj to 2050 2019;44:1–64.

[15] Harzer GS. Boosting High Current Density Performance of Durable, Low Pt-Loaded PEM Fuel Cells 2018.

[16] Ramaswamy, Nagappan; Gu, Wenbin; Kumaraguru, Swami; Ziegelbauer J. Carbon Support Microstructure Impact on High Current Density Transport Resistances in PEMFC Cathode. J Electrochem Soc 2019.

[17] Forner-Cuenca A. Novel Gas Diffusion Layers with Patterned Wettability for Advanced Water Management Strategies in Polymer Electrolyte Fuel Cells 2017. https://doi.org/10.3929/ETHZ-A-010811344.

[18] Spernjak D, Mukundan R, Borup RL, Connolly LG, Zackin BI, De Andrade V, et al. Enhanced Water Management of Polymer Electrolyte Fuel Cells with Additive-Containing Microporous Layers. ACS Appl Energy Mater 2018;1:6006–17. https://doi.org/10.1021/acsaem.8b01059.

[19] Zenyuk I V., Parkinson DY, Connolly LG, Weber AZ. Gas-diffusion-layer structural properties under compression via X-ray tomography. J Power Sources 2016;328:364–76. https://doi.org/10.1016/j.jpowsour.2016.08.020.

[20] Schweiss R, Meiser C, Damjanovic T, Galbiati I, Haak N. SIGRACET ® Gas Diffusion Layers for PEM Fuel Cells , Electrolyzers and Batteries. SGL Gr 2016:1–10.

[21] Marcinkoski J, Spendelow J, Wilson A, Papageorgopoulos D. DOE Hydrogen and Fuel Cells Program Record - Fuel Cell System Cost - 2017. J Mech Robot 2017;9:1–9. https://doi.org/10.1115/1.4036738.

[22] The US Department of Energy (DOE) Energy Efficiency and Renewable Energy. Fuel Cell Multi-Year Research, Development and Demonstration Plan. Fuel Cell Technol Off 2017;2015:3.4.1-3.4.58. https://doi.org/Department of Energy.

[23] Harzer GS, Schwämmlein JN, Damjanović AM, Ghosh S, Gasteiger HA. Cathode Loading Impact on Voltage Cycling Induced PEMFC Degradation: A Voltage Loss Analysis. J Electrochem Soc 2018;165:F3118–31. https://doi.org/10.1149/2.0161806jes.

[24] Stariha S, Macauley N, Sneed BT, Langlois D, More KL, Mukundan R, et al. Recent Advances in Catalyst Accelerated Stress Tests for Polymer Electrolyte Membrane Fuel Cells. J Electrochem Soc 2018;165:F492–501. https://doi.org/10.1149/2.0881807jes.

[25] Perry RL. Analysis of Durability of MEAs in Automotive PEMFC Applications 2011:794–6.

[26] Geyer HK, Ahluwalia RK. GCtool for Fuel Cell Systems Design and Analysis: User Documentation 1998.

[27] Cherevko S, Kulyk N, Mayrhofer KJJ. Durability of platinum-based fuel cell electrocatalysts: Dissolution of bulk and nanoscale platinum. Nano Energy 2016;29:275–98. https://doi.org/10.1016/j.nanoen.2016.03.005.

[28] Khedekar K, Cheng L, Kuppan S, Perego A, Stewart S, Atanassov P, et al. Effect of Commercial Gas Diffusion Layers on Catalyst Durability of Polymer Electrolyte Fuel Cells in Varied Cathode Gas Environment. Small 2021;MA2021-02:1193–

1193. https://doi.org/10.1149/ma2021-02391193mtgabs.

[29] Khedekar K, Rezaei Talarposhti M, Besli MM, Kuppan S, Perego A, Chen Y, et al. Probing Heterogeneous Degradation of Catalyst in PEM Fuel Cells under Realistic Automotive Conditions with Multi-Modal Techniques. Adv Energy Mater 2021;11. https://doi.org/10.1002/aenm.202101794.

[30] Gilbert JA, Kariuki NN, Wang X, Kropf AJ, Yu K, Groom DJ, et al. Pt catalyst degradation in aqueous and fuel cell environments studied via in-operando anomalous small-angle X-ray acattering. Electrochim Acta 2015;173:223–34. https://doi.org/10.1016/j.electacta.2015.05.032.

[31] Kneer A, Jankovic J, Susac D, Putz A, Wagner N, Sabharwal M, et al. Correlation of Changes in Electrochemical and Structural Parameters due to Voltage Cycling Induced Degradation in PEM Fuel Cells. J Electrochem Soc 2018;165:F3241–50. https://doi.org/10.1149/2.0271806jes.

[32] Zhang J, Litteer BA, Gu W, Liu H, Gasteiger HA. Effect of Hydrogen and Oxygen Partial Pressure on Pt Precipitation within the Membrane of PEMFCs. J Electrochem Soc 2007;154:B1006. https://doi.org/10.1149/1.2764240.

[33] Myers DJ, Wang X, Smith MC, More KL. Potentiostatic and Potential Cycling Dissolution of Polycrystalline Platinum and Platinum Nano-Particle Fuel Cell Catalysts. J Electrochem Soc 2018;165:F3178–90. https://doi.org/10.1149/2.0211806jes.

[34] Kneer A, Wagner N, Sadeler C, Scherzer A-C, Gerteisen D. Effect of Dwell Time and Scan Rate during Voltage Cycling on Catalyst Degradation in PEM Fuel Cells. J Electrochem Soc 2018;165:F805–12. https://doi.org/10.1149/2.0651810jes.

[35] Kneer A, Wagner N. A Semi-Empirical Catalyst Degradation Model Based on Voltage Cycling under Automotive Operating Conditions in PEM Fuel Cells. J Electrochem Soc 2019;166:F120–7. https://doi.org/10.1149/2.0641902jes.

[36] Zhang H, Haas H, Hu J, Kundu S, Davis M, Chuy C. The Impact of Potential Cycling on PEMFC Durability. J Electrochem Soc 2013;160:F840–7. https://doi.org/10.1149/2.083308jes.

[37] Reiser CA, Bregoli L, Patterson TW, Yi JS, Yang JD, Perry ML, et al. A reverse-current decay mechanism for fuel cells. Electrochem Solid-State Lett 2005;8. https://doi.org/10.1149/1.1896466.

[38] Brightman E, Hinds G. In situ mapping of potential transients during start-up and shut-down of a polymer electrolyte membrane fuel cell. J Power Sources 2014;267:160–70. https://doi.org/10.1016/j.jpowsour.2014.05.040.

[39] Simon C, Hasché F, Gasteiger HA. Influence of the Gas Diffusion Layer Compression on the Oxygen Transport in PEM Fuel Cells at High Water Saturation Levels. J Electrochem Soc 2017;164:F591–9. https://doi.org/10.1149/2.0691706jes.

[40] Baker DR, Wieser C, Neyerlin KC, Murphy MW. The Use of Limiting Current to Determine Transport Resistance in PEM Fuel Cells 2006;3:989–99. https://doi.org/10.1149/1.2356218.

[41] Greszler TA, Caulk D, Sinha P. The Impact of Platinum Loading on Oxygen Transport Resistance. J Electrochem Soc 2012;159:F831–40. https://doi.org/10.1149/2.061212jes.

[42] M. Eikerling AAK. Electrochemical impedance of the cathode catalyst layer in polymer electrolyte fuel cells. J Electroanal Chem 1999;475:107–23. https://doi.org/10.1038/hdy.1988.111.

[43] Setzler BP, Fuller TF. A Physics-Based Impedance Model of Proton Exchange Membrane Fuel Cells Exhibiting Low-Frequency Inductive Loops. J Electrochem Soc 2015;162:F519–30. https://doi.org/10.1149/2.0361506jes.

[44] J. Pfeilsticker. Open Source Impedance Fitter, Github. n.d.

[45] Gasteiger HA, Panels JE, Yan SG. Dependence of PEM fuel cell performance on catalyst loading. J Power Sources 2004;127:162–71. https://doi.org/10.1016/j.jpowsour.2003.09.013.

[46] Wang M, Medina S, Pfeilsticker JR, Pylypenko S, Ulsh M, Mauger SA. Impact of Microporous Layer Roughness on Gas-Diffusion-Electrode-Based Polymer Electrolyte Membrane Fuel Cell Performance. ACS Appl Energy Mater 2019;2:7757–61. https://doi.org/10.1021/acsaem.9b01871.

[47] Neyerlin KC, Gu W, Jorne J, Gasteiger HA. Determination of Catalyst Unique Parameters for the Oxygen Reduction Reaction in a PEMFC. J Electrochem Soc 2006;153:A1955. https://doi.org/10.1149/1.2266294.

[48] J. Schindelin, I. Arganda-Carreras, E. Frise, V. Kaynig, M. Longair, T. Pietzsch, S. Preibisch, C. Rueden, S. Saalfeld, B. Schmid, J.-Y. Tinevez, D. J. White, V. Hartenstein, K. Eliceiri PT and AC. Fiji: an open-source platform for biological-image analysis 2012:676–82.

[49] Cooper SJ, Bertei A, Shearing PR, Kilner JA, Brandon NP. TauFactor: An open-source application for calculating tortuosity factors from tomographic data. SoftwareX 2016;5:203–10. https://doi.org/10.1016/j.softx.2016.09.002.

[50] Gostick J, Aghighi M, Hinebaugh J, Tranter T, Hoeh MA, Day H, et al. OpenPNM: A Pore Network Modeling Package. Comput Sci Eng 2016;18:60–74. https://doi.org/10.1109/MCSE.2016.49.

[51] Uchida M, Aoyama Y, Eda N, Ohta A. New Preparation Method for Polymer-Electrolyte Fuel Cells. J Electrochem Soc 1995;142:463–8. https://doi.org/10.1149/1.2044068.

[52] Cheng L, Khedekar K, Rezaei Talarposhti M, Perego A, Metzger M, Kuppan S, et al. Mapping of Heterogeneous Catalyst Degradation in Polymer Electrolyte Fuel Cells. Adv Energy Mater 2020;10. https://doi.org/10.1002/aenm.202000623.

[53] Barabash GIR. Strain and Dislocation Gradients From Diffraction: Spatially-Resolved Local Structures and Defects 2014.

[54] Gürsoy D, De Carlo F, Xiao X, Jacobsen C. TomoPy: A framework for the analysis of synchrotron tomographic data. J Synchrotron Radiat 2014;21:1188–93. https://doi.org/10.1107/S1600577514013939.

[55] Serov A, Shum AD, Xiao X, De Andrade V, Artyushkova K, Zenyuk I V., et al. Nano-structured platinum group metal-free catalysts and their integration in fuel cell electrode architectures. Appl Catal B Environ 2018;237:1139–47. https://doi.org/10.1016/j.apcatb.2017.08.067.

[56] Shum AD, Parkinson DY, Xiao X, Weber AZ, Burheim OS, Zenyuk I V. Investigating Phase-Change-Induced Flow in Gas Diffusion Layers in Fuel Cells with X-ray Computed Tomography. Electrochim Acta 2017;256:279–90. https://doi.org/10.1016/j.electacta.2017.10.012.

[57] Xie J, Wood DL, Wayne DM, Zawodzinski TA, Atanassov P, Borup RL. Durability of PEFCs at High Humidity Conditions. J Electrochem Soc 2005;152:A104. https://doi.org/10.1149/1.1830355.

[58] Jahnke T, Futter GA, Baricci A, Rabissi C, Casalegno A. Physical Modeling of Catalyst Degradation in Low Temperature Fuel Cells: Platinum Oxidation, Dissolution, Particle Growth and Platinum Band Formation. J Electrochem Soc 2020;167:013523. https://doi.org/10.1149/2.0232001jes.

[59] Darling RM, Meyers JP. Kinetic Model of Platinum Dissolution in PEMFCs. J Electrochem Soc 2003;150:A1523. https://doi.org/10.1149/1.1613669.

[60] Kabir S, Myers DJ, Kariuki N, Park J, Wang G, Baker A, et al. Elucidating the Dynamic Nature of Fuel Cell Electrodes as a Function of Conditioning: An ex Situ Material Characterization and in Situ Electrochemical Diagnostic Study. ACS Appl Mater Interfaces 2019;11:45016–30. https://doi.org/10.1021/acsami.9b11365.

[61] Wang X, Kumar R, Myers DJ. Effect of voltage on platinum dissolution relevance to polymer electrolyte fuel cells. Electrochem Solid-State Lett 2006;9:225–7. https://doi.org/10.1149/1.2180536.

[62] Lopes PP, Strmcnik D, Tripkovic D, Connell JG, Stamenkovic V, Markovic NM. Relationships between Atomic Level Surface Structure and Stability/Activity of Platinum Surface Atoms in Aqueous Environments. ACS Catal 2016;6:2536–44. https://doi.org/10.1021/acscatal.5b02920.

[63] Neyerlin KC, Srivastava R, Yu C, Strasser P. Electrochemical activity and stability of dealloyed Pt-Cu and Pt-Cu-Co electrocatalysts for the oxygen reduction reaction (ORR). J Power Sources 2009;186:261–7. https://doi.org/10.1016/j.jpowsour.2008.10.062.

[64] Pizzutilo E, Geiger S, Grote J-P, Mingers A, Mayrhofer KJJ, Arenz M, et al. On the Need of Improved Accelerated Degradation Protocols (ADPs): Examination of Platinum Dissolution and Carbon Corrosion in Half-Cell Tests. J Electrochem Soc

2016;163:F1510–4. https://doi.org/10.1149/2.0731614jes.

[65] Curnick OJ, Pollet BG, Mendes PM. Nafion®-stabilised Pt/C electrocatalysts with efficient catalyst layer ionomer distribution for proton exchange membrane fuel cells. RSC Adv 2012;2:8368–74. https://doi.org/10.1039/c2ra21071a.

[66] Sethuraman VA, Weidner JW, Haug AT, Pemberton M, Protsailo L V. Importance of catalyst stability vis-à-vis hydrogen peroxide formation rates in PEM fuel cell electrodes. Electrochim Acta 2009;54:5571–82. https://doi.org/10.1016/j.electacta.2009.04.062.

[67] Schneider IA, von Dahlen S, Wokaun A, Scherer GG. A Segmented Microstructured Flow Field Approach for Submillimeter Resolved Local Current Measurement in Channel and Land Areas of a PEFC. J Electrochem Soc 2010;157:B338. https://doi.org/10.1149/1.3274228.

[68] Satjaritanun P, Cetinbas FC, Hirano S, Zenyuk I V., Ahluwalia RK, Shimpalee S. Hybrid Lattice Boltzmann Agglomeration Method for Modeling Transport Phenomena in Polymer Electrolyte Membrane Fuel Cells. J Electrochem Soc 2021;168:044508. https://doi.org/10.1149/1945-7111/abf217.

[69] Turhan A, Heller K, Brenizer JS, Mench MM. Quantification of liquid water accumulation and distribution in a polymer electrolyte fuel cell using neutron imaging. J Power Sources 2006;160:1195–203. https://doi.org/10.1016/j.jpowsour.2006.03.027.

[70] Trabold TA, Owejan JP, Jacobson DL, Arif M, Huffman PR. In situ investigation of water transport in an operating PEM fuel cell using neutron radiography: Part 1 - Experimental method and serpentine flow field results. Int J Heat Mass Transf 2006;49:4712–20. https://doi.org/10.1016/j.ijheatmasstransfer.2006.07.003.

[71] Chandesris M, Guetaz L, Schott P, Scohy M, Escribano S. Investigation of Degradation Heterogeneities in PEMFC Stack Aged under Reformate Coupling In Situ Diagnosis, Post-Mortem Ex Situ Analyses and Multi-Physic Simulations. J Electrochem Soc 2018;165:F3290–306. https://doi.org/10.1149/2.0321806jes.

[72] Trasatti S, Petrii OA. International Union of Pure and Applied Chemistry Physical Chemistry Division Commission on Electrochemistry: Real Surface Area Measurements in Electrochemistry. Pure Appl Chem 1991;63:711–34. https://doi.org/10.1351/pac199163050711.

[73] Quan M, Sanchez D, Wasylkiw MF, Smith DK. Voltammetry of quinones in unbuffered aqueous solution: Reassessing the roles of proton transfer and hydrogen bonding in the aqueous electrochemistry of quinones. J Am Chem Soc 2007;129:12847–56. https://doi.org/10.1021/ja0743083.

[74] Macauley N, Papadias DD, Fairweather J, Spernjak D, Langlois D, Ahluwalia R, et al. Carbon Corrosion in PEM Fuel Cells and the Development of Accelerated Stress Tests. J Electrochem Soc 2018;165:F3148–60. https://doi.org/10.1149/2.0061806jes.

[75] Schlögl K, Mayrhofer KJJ, Hanzlik M, Arenz M. Identical-location TEM investigations of Pt/C electrocatalyst degradation at elevated temperatures. J Electroanal Chem 2011;662:355–60. https://doi.org/10.1016/j.jelechem.2011.09.003.

[76] Liu Y, Murphy M, Baker D, Gu W, Ji C, Jorne J, et al. Determination of Electrode Sheet Resistance in Cathode Catalyst Layer by AC Impedance. ECS Meet Abstr 2007;MA2007-02:425–425. https://doi.org/10.1149/ma2007-02/9/425.

[77] Saleh FS, Easton EB. Diagnosing Degradation within PEM Fuel Cell Catalyst Layers Using Electrochemical Impedance Spectroscopy. J Electrochem Soc 2012;159:B546–53. https://doi.org/10.1149/2.098205jes.

[78] Jung J, Chung YH, Park HY, Han J, Kim HJ, Henkensmeier D, et al. Electrochemical impedance analysis with transmission line model for accelerated carbon corrosion in polymer electrolyte membrane fuel cells. Int J Hydrogen Energy 2018;43:15457–65. https://doi.org/10.1016/j.ijhydene.2018.06.093.

[79] Makharia R, Mathias MF, Baker DR. Measurement of Catalyst Layer Electrolyte Resistance in PEFCs Using Electrochemical Impedance Spectroscopy. J Electrochem Soc 2005;152:A970. https://doi.org/10.1149/1.1888367.

[80] Thiele S, Zengerle R, Ziegler C. Nano-morphology of a polymer electrolyte fuel cell catalyst layer-imaging, reconstruction and analysis. Nano Res 2011;4:849–60. https://doi.org/10.1007/s12274-011-0141-x.

[81] Sabharwal M, Pant LM, Putz A, Susac D, Jankovic J, Secanell M. Analysis of Catalyst Layer Microstructures: From Imaging to Performance. Fuel Cells 2016;16:734–53. https://doi.org/10.1002/fuce.201600008.

[82] Yu Z, Carter RN, Zhang J. Measurements of pore size distribution, porosity, effective oxygen diffusivity, and tortuosity of PEM fuel cell electrodes. Fuel Cells 2012;12:557–65. https://doi.org/10.1002/fuce.201200017.

[83] Arisetty S, Wang X, Ahluwalia RK, Mukundan R, Borup R, Davey J, et al. Catalyst Durability in PEM Fuel Cells with Low Platinum Loading. J Electrochem Soc 2012;159:B455–62. https://doi.org/10.1149/2.jes113064.

[84] Kongkanand A, Mathias MF. The Priority and Challenge of High-Power Performance of Low-Platinum Proton-Exchange Membrane Fuel Cells. J Phys Chem Lett 2016;7:1127–37. https://doi.org/10.1021/acs.jpclett.6b00216.

[85] Komini Babu S, Mukundan R, Wang C, Langlois D, Cullen DA, Papadias D, et al. Effect of Catalyst and Catalyst Layer Composition on Catalyst Support Durability. J Electrochem Soc 2021;168:044502. https://doi.org/10.1149/1945-7111/abf21f.

[86] Hegge F, Sharman J, Moroni R, Thiele S, Zengerle R, Breitwieser M, et al. Impact of Carbon Support Corrosion on Performance Losses in Polymer Electrolyte Membrane Fuel Cells. J Electrochem Soc 2019;166:F956–62. https://doi.org/10.1149/2.0611913jes.

[87] Yu H, Zachman MJ, Li C, Hu L, Kariuki NN, Mukundan R, et al. Recreating Fuel

Cell Catalyst Degradation in Aqueous Environments for Identical-Location Scanning Transmission Electron Microscopy Studies. ACS Appl Mater Interfaces 2021. https://doi.org/10.1021/acsami.1c23281.

[88] Lazaridis T, Stühmeier BM, Gasteiger HA, El-Sayed HA. Capabilities and limitations of rotating disk electrodes versus membrane electrode assemblies in the investigation of electrocatalysts. Nat Catal 2022;5:363–73. https://doi.org/10.1038/s41929-022-00776-5.

[89] Wang M, Park JH, Kabir S, Neyerlin KC, Kariuki NN, Lv H, et al. Impact of Catalyst Ink Dispersing Methodology on Fuel Cell Performance Using in-Situ X-ray Scattering 2019. https://doi.org/10.1021/acsaem.9b01037.

[90] Cetinbas FC, Ahluwalia RK, Shum AD, Zenyuk I V. Direct Simulations of Pore-Scale Water Transport through Diffusion Media. J Electrochem Soc 2019;166:F3001–8. https://doi.org/10.1149/2.0011907jes.